MECHANICS OF CHIRAL, ANTI-CHIRAL, AND HIERARCHICAL HONEYCOMBS

A Dissertation Presented

By

DAVOOD MOUSANEZHAD VIYAND

to

The Department of Mechanical and Industrial Engineering

in partial fulfillment of the requirements

for the degree of

Doctor of Philosophy

in the field of

Mechanical Engineering

Northeastern University

Boston, Massachusetts

May 2016

Abstract

The effects of two geometric refinement strategies widespread in natural structures, chirality and self-similar hierarchy, on mechanical response of two-dimensional honeycombs were studied systematically.

First, by employing the concepts of mechanics of materials, simple closed-form expressions were derived for the elastic moduli of several chiral, anti-chiral, and hierarchical honeycombs with hexagon and square based networks. The analytical results were validated using finite element analysis and experimental data available in the literature.

Next, a new class of hierarchical fractal-like honeycombs inspired by the topology of the "spiderweb" was introduced and investigated for its small and large deformation response through analytical modeling, detailed numerical simulations, and mechanical testing. For small deformations, the elastic moduli can be controlled by geometrical ratios in the hierarchical pattern, and the response can vary from bending to stretching dominated. These structures exhibit auxetic behavior at large deformations.

Next, we exploit mechanical instabilities and structural hierarchy to induce negative Poisson's ratio over a wide range of applied compressive strains in hierarchical structures which otherwise exhibit positive Poisson's ratio at small deformations. This unusual behavior is demonstrated experimentally and analyzed computationally.

Finally, we highlighted the effects of structural hierarchy and deformation on band structure and wave-propagation behavior of two-dimensional phononic crystals. We employed finite element analysis along with Bloch theorem to show that the topological hierarchical architecture and instability-induced pattern transformations of the structure under compression can be effectively used to tune the band gaps and directionality of phononic crystals.

Acknowledgements

I wish to express my deep gratitude to Professor Ashkan Vaziri, my academic advisor, for his guidance, constant encouragement, and his valuable advice in the last four and a half years. But more than that, it is his personal warmth that has made working with him such a valuable experience for me.

I would also like to express my sincere appreciation to Professor Hamid Nayeb-Hashemi for his support both technically as well as emotionally, and for the valuable suggestions and stimulating discussions we have had. I would not have been able to complete this work without his help.

This acknowledgement would be incomplete, if I miss to mention the support I received from my research group, especially Dr. Jim Papadopoulos, Dr. Ranajay Ghosh, Dr. Amin Ajdari, Dr. Babak Haghpanah, Dr. Hamid Ebrahimi, Dr. Sahab Babaee, and Dr. Ramin Oftadeh for their fruitful discussions. I would also like to thank my family for their everlasting love and unconditional encouragement throughout my whole life. Without their help and support, I wouldn't be able to make this happen.

Table of Contents

List of Figures

List of Tables

Chapter 1

Elastic Properties of Chiral, Anti-Chiral, and Hierarchical Honeycombs: A Simple Energy-Based Approach

1.1 Abstract

The effects of two geometric refinement strategies widespread in natural structures, chirality and self-similar hierarchy, on the in-plane elastic response of two-dimensional honeycombs were studied systematically. Simple closed-form expressions were derived for the elastic moduli of several chiral, anti-chiral, and hierarchical honeycombs with hexagon and square based networks. Finite element analysis was employed to validate the analytical estimates of the elastic moduli. The results were also compared with the numerical and experimental data available in the literature. We found that introducing a hierarchical refinement increases the Young's modulus of hexagon based honeycombs while decreases their shear modulus. For square based honeycombs, hierarchy increases the shear modulus while decreasing their Young's modulus. Introducing chirality was shown to always decrease the Young's modulus and Poisson's ratio of the structure. However, chirality remains the only route to auxeticity. In particular, we found that anti-tetra-chiral structures were capable of simultaneously exhibiting anisotropy, auxeticity, and remarkably low shear modulus as the magnitude of the chirality of the unit cell increases.

1.2 Introduction

Among the most readily observed topological features in natural structures are chirality [1-5], hierarchy [6-13], and hierarchy of chirality [14, 15]. Their abundance in nature can be contrasted with traditional man-made constructions, which often rely on multiple materials selection but relatively simpler micro-geometrical constitution. In recent years, following these topological cues, synthetic metamaterials with non-traditional properties such as negative stiffness [16-18], auxeticity [19-22], and negative thermal expansion [23-25] have been proposed. These characteristics make mechanical metamaterials suitable for applications such as novel prostheses [26], fasteners [27], piezo-composites with optimal performance [28], dome-shaped panels [29, 30], and high structural integrity foams [31].

Among this general class of metamaterials, periodic chiral lattices such as the ones shown in **Figure 1.1** have been shown to possess relatively compliant behavior because of their bending dominated response, while exhibiting considerable multi-axial expansion/contraction under uniaxial loads due to auxeticity [32, 33]. These features make them optimal candidates for flexible design applications such as micro-electro-mechanical-systems (MEMS) [19, 34, 35], aircraft morphing structures [36-43], and as analogues of spokes in non-pneumatic tires [44, 45]. In addition, chiral honeycombs have been experimentally and numerically shown to possess Poisson's ratios in the range of $-1 < \nu < 0$. For instance, Alderson et al. [46] studied the in-plane elastic constants of chiral and anti-chiral honeycombs using finite element (FE) analysis and experiments. Continuing further, Alderson et al. [47] investigated the in-plane linear elastic response and out-of-plane bending of tri- and anti-tri-chiral honeycombs and their re-entrant counterparts using FE analysis and experiments. Nonetheless, closed-form expressions of elastic moduli for most of these structures are still unavailable. Among several two-dimensional (2D) chiral lattices proposed in the literature, only the elastic properties of hexa- and tetra-chiral lattices have been investigated analytically, using micro-polar and second-gradient continuum theories [32, 48-51]. These approaches are far more complex than the simple yet robust method used here for analytical study of chiral unit cells, which often require special boundary conditions at the unit cell level due to underlying rotational symmetry of the structure.

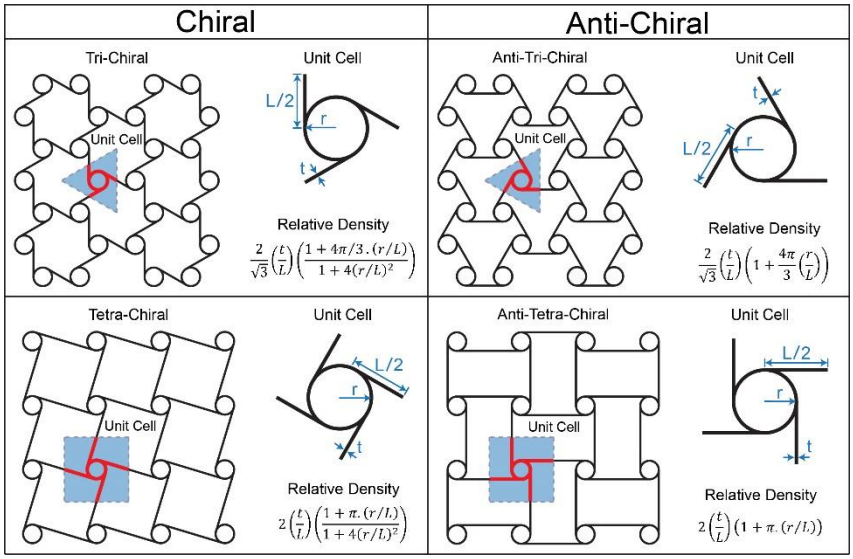

Figure 1.1 Schematic of the structure and the unit cell, and the expression of relative density for the chiral and anti-chiral honeycombs studied.

Another class of bio-inspired materials used increasingly to broaden the achievable range of mechanical response is the hierarchically structured material systems. Extreme values of material properties such as specific stiffness [11, 52-54], toughness [55-58], strength [11, 53, 59, 60], buckling strength [61], negative or complex Poisson's ratio [62-65], and phononic band gaps [66] have been reported in hierarchical architectures across multiple length scales. Through a series of studies on the strength of different fractal-like structures under various loads, Farr and co-workers [59, 67-70] suggested that the volume of the material used for a stable structure can be reduced by an order of 3 to 4 under mild loads using hierarchical designs of third and fourth generation. However, the advantage of hierarchical design in these structures diminishes as the magnitude of applied loading increases. Ajdari et al. [52] showed that a type of self-similar hierarchical honeycomb is capable of attaining specific Young's modulus as much as 2 and 3.5 times that of a regular hexagonal lattice through first and second orders of hierarchy, respectively. In a more inclusive study that considered enhancements in multiple parameters, Haghpanah et al. [71] showed that a wide range of specific stiffness and strength can be tailored by introducing higher orders of hierarchy in a hexagonal lattice. However, none of these earlier studies specifically focused on investigating the geometry of hierarchy as a

controlling variable of mechanical properties of honeycombs. Moreover, there is no systematic comparison between hierarchy and chirality in the literature, which can be useful in design and selection of structures for different loading conditions.

In light of this discussion, it becomes clear that further investigations on the behavior of these classes of metamaterials are well justified. Particularly, obtaining closed-form analytical expressions for the elastic constants in terms of geometric and material parameters would constitute an important step towards evaluating and designing these materials. Furthermore, it would also foster a better understanding of the role of chirality and hierarchy in influencing the mechanical response of these materials. To this end, as a part of this dissertation, we carry out a systematic theoretical and computational study of the effects of these two natural geometrical organizations - chirality and hierarchy - on the in-plane elastic response of 2D honeycombs. In order to directly compare the effects of chirality versus hierarchy, we limit the results to first order of hierarchy for the hierarchical structures presented here. An energy-based method is used to obtain the unit cell deformation by satisfying both the periodic boundary conditions and symmetry requirements for the unit cell. Two specific types of regular tessellation with square and hexagonal cells are altered to endow them with chirality and hierarchy. For achieving chirality, the square based unit cell is altered to yield two different types of chiral architectures - tetra-chiral and anti-tetra-chiral - whereas the hexagonal unit cell alteration results in tri-chiral and anti-tri-chiral structures (illustrated in **Figure 1.1**). In contrast to chiral microstructures, hierarchy is achieved by both conserving the rotational and reflective symmetries of the lattice. This is done by replacing the nodes in a periodic network of cells with the original cells albeit of smaller size as shown in **Figure 1.2**. Thus, the introduction of hierarchy into the square unit cell results in hierarchical square and hierarchical diamond honeycombs (illustrated in **Figure 1.2**). In order to proceed with our calculations, the Representative Volume Element (RVE) is used as the fundamental unit of analysis. In a periodic lattice material, the RVE (i.e., unit cell) is identified as the smallest volume which with associated tractions and displacements, tessellates the space to represent the whole lattice structure under loading [60]. We choose the shaded triangular and square areas bounded by dashed lines in **Figures 1.1** and **1.2** as the structural unit cells of the structures under study. This implies that under any in-plane loading, we can tile the

2D space, solely by translating, and/or reflecting, and/or rotating (by 180^o) the unit cells and their corresponding tractions and displacements, to represent the infinitely extended 2D structures.

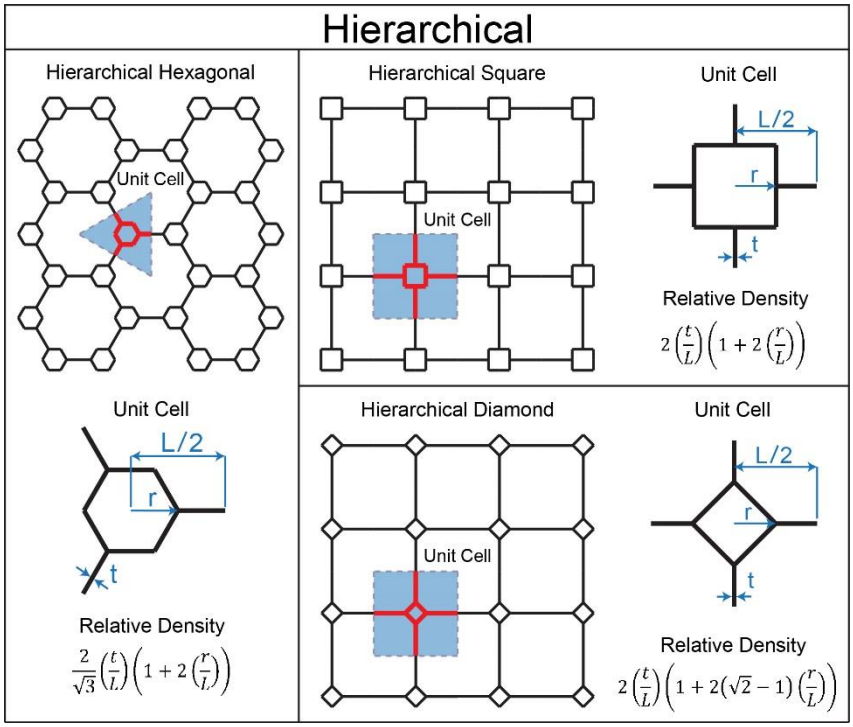

Figure 1.2 Schematic of the structure and the unit cell, and the expression of relative density for the hierarchical honeycombs studied.

We first describe and derive the elastic moduli (i.e., Young's and shear moduli, and Poisson's ratio) of chiral and anti-chiral structures. This is followed by a section devoted to deriving the elastic constants for the hierarchical structures. The results are then compared in a unified template to highlight the effects brought about by these geometrical variants. This chapter ends with conclusions.

1.3 Chiral and anti-chiral structures

Chiral and anti-chiral structures studied in this dissertation have an array of cylinders (nodes) connected by tangential ligaments (ribs) as shown in **Figure 1.1**. Depending on the number of ligaments tangential to each cylinder, two types of chiral lattices are introduced:

tri-, and tetra-chiral structures which are respectively composed of 3, and 4 tangential ligaments for each cylinder. Similarly, anti-chiral lattices are generated if any two adjacent cylinders share the same side of the common tangential ligament. Thus, in addition, two anti-chiral lattices are introduced which are called anti-tri-, and anti-tetra-chiral structures (see **Figure 1.1**).

The structural organization of the chiral and anti-chiral honeycombs can be defined by the ratio, r/L, where r is the radius of the cylinders and L is the length of the ligaments as described in **Figure 1.1**. This figure also represents the dimensionless relative density (i.e., area fraction) of the structures in terms of r/L and t/L, where t is the thickness of the cell walls. For the special case, where $r = 0$, the normalized relative density of the hexagon (tri-chiral and anti-tri-chiral), and square (tetra-chiral and anti-tetra-chiral) based chiral and anti-chiral honeycombs respectively reduce to that of regular hexagonal ($2/\sqrt{3}\ .(t/L)$), and square ($2\,t/L$) honeycombs.

1.3.1 Theoretical formulations

Here, we derive closed-form expressions for elastic properties of chiral and anti-chiral honeycombs made of an isotropic linear elastic material with Young's modulus, E_s. In contrast to the previous studies [32, 33, 48-51], we employ a simple energy-based procedure (Castigliano's second theorem [72]) to obtain analytical estimates for elastic properties of the structures under study. A three-fold symmetry seen within the tri- and anti-tri-chiral lattices (see **Figure 1.1**) assures the macroscopic isotropy of their in-plane elastic properties [73]. Thus, for complete characterization of these structures, they each need only two elastic constants to be determined (i.e., Young's modulus and Poisson's ratio) (shear modulus is obtained as a function of the other two elastic constants, analogous to isotropic materials). In principle, these elastic constants can be determined by any kind of in-plane loading. However, in this study, without loss of generality we chose uniaxial loading to obtain the Young's modulus and Poisson's ratio. In contrast, the four-fold symmetry of tetra- and anti-tetra-chiral honeycombs causes the structures to exhibit macroscopic anisotropy in their in-plane elastic behavior. Therefore, all the components of their stiffness (or compliance) tensor have to be determined in order to fully identify their

elastic behavior. For tetra- and anti-tetra-chiral lattices, we first chose a coordinate system such that the x and y axes were aligned to the lines connecting the center of adjacent cylinders together. This symmetry requires one Young's modulus, one Poisson's ratio, one shear modulus, and possibly two more coefficients called "the coefficients of mutual influence of the first kind" [74] (they characterize the normal strains caused by shear stresses).

To this end, for each of the anisotropic honeycombs (tetra- and anti-tetra-chiral structures), we first impose a uniaxial loading in the x-direction (i.e., horizontal direction in Fig. 1) to obtain the structure's Young's modulus, E_x, and Poisson's ratio, ν_{xy}. Note that the sub-index x, is used to emphasize that the elastic constants are obtained as a result of a loading in the x-direction and they are not valid for any other directions (except for y-direction (i.e., vertical direction in **Figure 1.1**), due to symmetry) of in-plane loading since the structures do not have an isotropic in-plane behavior. Furthermore due to this anisotropy, in order to obtain the shear modulus, G_{xy}, and the coefficients of mutual influence of the first kind, we apply a separate shearing load to these structures. It is noteworthy that since these structures are stretching dominated in both the x- and y-directions, we must include the stretching terms in addition to bending terms in computing the strain energy of the unit cells. In contrast, for bending dominated structures, we only include the bending terms of strain energy. In our theoretical calculations, the central cylinders appearing in the unit cells are regarded as perfectly rigid elements. Also the rotation of ligaments and cylinders is neglected due to small deformation assumption. These assumptions significantly reduce the complexity of the problem yielding closed-form expressions for elastic moduli while staying reasonably accurate for most of the geometries considered in this study.

In the next paragraphs, we will derive closed-form expressions for the elastic moduli of tetra-chiral structures as a demonstration of our proposed method. The detailed derivations for other chiral and anti-chiral structures are presented in **Appendices**.

A schematic of a tetra-chiral structure, which is based on an underlying square network, undergoing a uniaxial far-field stress in the x-direction, σ_x is shown in **Figure 1.3 (A)**. The free body diagram (FBD) of the corresponding unit cell is shown in **Figure**

1.3 (B). The unit cell contains a cylinder (node) which is assumed to be rigid and four half ligaments. Due to the 180° rotational symmetry of the structure and the components of the microscopic stresses, all four external cut points of the unit cell (i.e., points 1 through 4 in **Figure 1.3 (B)**) must be moment-free under an arbitrary macroscopic stress state. Also, since the only far-field stress acting on the structure is along the *x*-direction, all the external cut points must be force-less except points 1 and 2 which carry a pair of forces with opposite directions along the *x*-direction due to σ_x. Therefore, unknown forces and moments acting on the unit cell's external cut points can be summarized as shown in **Figure 1.3 (B)**, where F can be determined as a function of applying stress as, $F = \sigma_x R$, where R is the center to center distance between any two adjacent cylinders. Moreover, to be able to determine the structure's Poisson's ratio, a pair of virtual forces, P is also added on points 2 and 4 of the unit cell. The strain energy of the unit cell is given as:

$$U = 2\frac{(F\cos\theta)^2\, L/2}{2E_s A} + 2\frac{(P\cos\theta)^2\, L/2}{2E_s A} + 2\int_0^{L/2} \frac{(xF\sin\theta)^2}{2E_s I}\,dx + 2\int_0^{L/2} \frac{(xP\sin\theta)^2}{2E_s I}\,dx \qquad (1.1)$$

where E_s (as mentioned earlier) is the Young's modulus of the cell wall material, A is the cross sectional area of cell walls (i.e., for a rectangular cross section with unit depth, $A = t$), I is the second moment of area of the wall's cross section (cell walls are assumed to have a rectangular cross section with uniform thickness, t, and unit depth, i.e., $I = t^3/12$), and $\theta = tan^{-1}(2r/L)$ is the angle between each ligament and the line connecting the centers of two adjacent cylinders as shown in **Figure 1.3 (B)**. Next, $\partial U/\partial F|_{P=0}$ gives the total displacement of point 1 with respect to point 3 in the x-direction as, $\delta_x = \frac{FL}{E_s A}cos^2\theta + \frac{FL^3}{12E_s I}sin^2\theta$. From this, we can now calculate the structure's average strain in the x-direction as, $\epsilon_x = \delta_x/R$. The Young's modulus of the structure normalized by material's Young's modulus is then defined as the ratio of the average stress, σ_x and the average strain, ϵ_x and obtained as:

$$E_x/E_s = \frac{t/L}{cos^2\theta + sin^2\theta/(t/L)^2} \tag{1.2}$$

On the other hand, $\partial U/\partial P|_{P=0}$ gives the total displacement of points 2 and 4 in the direction of virtual forces as $\delta_y = 0$. Therefore, $\epsilon_y = \delta_y/R = 0$ and this will result in $\nu_{xy} = 0$.

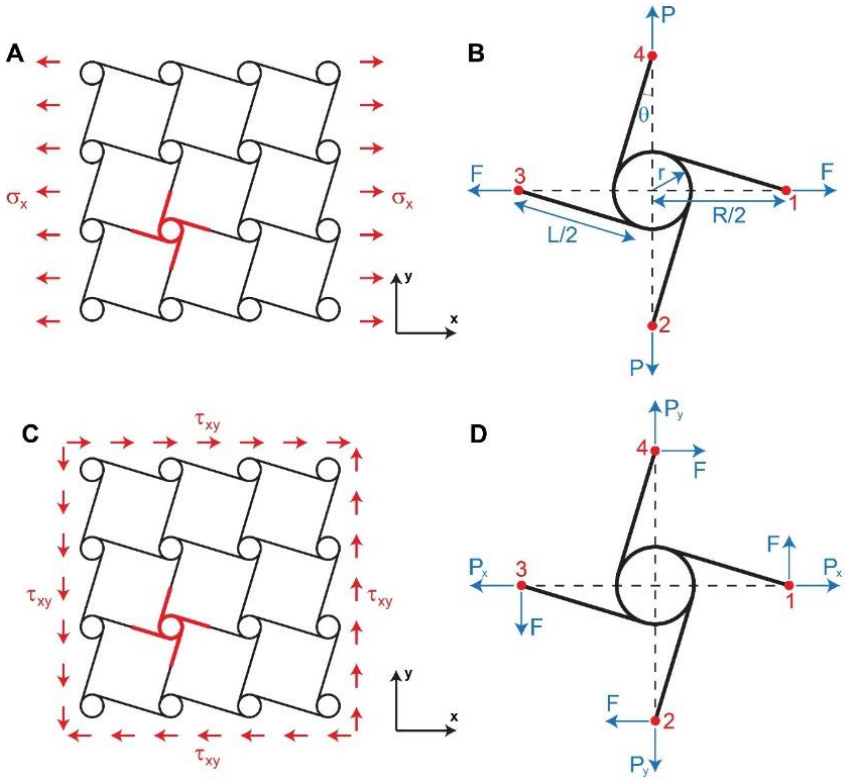

Figure 1.3 (A) Schematic of a tetra-chiral honeycomb under x-direction uniaxial loading. **(B)** Free body diagram of the structural unit cell under uniaxial loading. **(C)** Schematic of a tetra-chiral honeycomb under x-y shearing load. **(D)** Free body diagram of the structural unit cell under shearing load.

In the next step, we seek to determine the structure's shear modulus with respect to the x-y coordinate system. To this end, we consider a tetra-chiral structure undergoing a uniform far-field shear stress, τ_{xy}, as shown in **Figure 1.3 (C)**. FBD of a representative unit cell is also shown in **Figure 1.3 (D)**. The 180^o rotational symmetry of the structure implies unit cell's all four external cut points (i.e., points 1 through 4 in **Figure 1.3 (D)**) to be moment free. Furthermore, each of these external cut points must be free of any normal

forces (in the direction passing through the cut point and center of the cylinder), because there is no macroscopic normal stress acting on the structure in those directions. Thus, there are only four equal shearing forces acting on the unit cell's external cut points, F, which can be obtained as a function of applying stress as, $F = \tau_{xy}R$. We also apply two pairs of virtual forces, P_x, and P_y to the unit cell to be able to find the average strains in the x- and y- directions due to the applying shear stress. Therefore, based on the loadings on the unit cell shown in **Figure 1.3 (D)**, the strain energy is given as the following:

$$U = 2\frac{(Fsin\,\theta - P_x cos\,\theta)^2\, L/2}{2E_s A} + 2\frac{\left(Fsin\,\theta + P_y cos\,\theta\right)^2 L/2}{2E_s A} + 2\int_0^{L/2} \frac{\left((Fcos\,\theta + P_x sin\,\theta)x\right)^2}{2E_s I}\,dx + 2\int_0^{L/2} \frac{\left(\left(Fcos\,\theta - P_y sin\,\theta\right)x\right)^2}{2E_s I}\,dx \tag{1.3}$$

Next, $(\partial U/\partial F|_{P_x=P_y=0})/R$ gives the total change of angle between two straight lines initially parallel to the x- and y-axes which is the direct measure of the shear strain, γ_{xy}. Then, the shear modulus of the structure normalized with respect to the Young's modulus of cell wall material, is defined as the ratio of the average shear stress, τ_{xy} to the average shear strain, γ_{xy} and given as the following:

$$G_{xy}/E_s = \frac{0.5(t/L)^3}{cos^2\theta + (t/L)^2 sin^2\theta} \tag{1.4}$$

Note that as θ goes to zero, the structure transforms into a regular square honeycomb. Upon substituting $\theta = 0$ into the closed-form expressions for E_x and G_{xy}, we obtain $E_x/E_s = t/L$, and $G_{xy}/E_s = 0.5(t/L)^3$, which are the Young's and shear moduli of a regular square honeycomb, respectively [75]. For all values of θ, Poisson's ratio is equal to that of square honeycomb, $\nu_{xy} = 0$.

From the above calculations, the structure's 2D compliance tensor can be formed as the following:

$$S = \begin{bmatrix} S_{11} & S_{12} & S_{13} \\ S_{12} & S_{22} & S_{23} \\ S_{13} & S_{23} & S_{33} \end{bmatrix} \tag{1.5}$$

where $S_{11} = S_{22} = 1/E_x$, $S_{12} = -\nu_{xy}/E_x$, and $S_{33} = 1/G_{xy}$. Then, to completely determine all components of 2D compliance tensor of this structure, we still need to obtain S_{13} and S_{23}, which can respectively be given by calculating the average normal strains of the structure in the x- and y-directions due to the shearing load. $(\partial U/\partial P_x|_{P_x=P_y=0})/R$ and $(\partial U/\partial P_y\big|_{P_x=P_y=0})/R$ give the average normal strains in the x- and y-directions (ϵ_x and ϵ_y), respectively. Then, S_{13} and S_{23} are respectively defined as the ratio of the resulting normal strains in the x- and y-directions to the applying shear stress and given as the following:

$$S_{13} = \frac{\epsilon_x}{\tau_{xy}} = +\big((L/t)^3 - (L/t)\big) sin\theta cos\theta / E_s$$

$$S_{23} = \frac{\epsilon_y}{\tau_{xy}} = -\big((L/t)^3 - (L/t)\big) sin\theta cos\theta / E_s \tag{1.6}$$

Next, in order to find the orientation of principal coordinate system (i.e., directions in which S_{13} and S_{23} are both equal to zero which implies that no normal strains can be produced under shear stress) we rotate the x-y-z coordinate system with respect to the z-axis by an angle α (positive when counter-clockwise). The compliance tensor in the new system, $\bar{S}$ is determined using the compliance transformation rule [74], $\bar{S} = TST^T$, where T is the rotation tensor defined as:

$$T = \begin{bmatrix} m^2 & n^2 & mn \\ n^2 & m^2 & -mn \\ -2mn & 2mn & (m^2 - n^2) \end{bmatrix} \tag{1.7}$$

where $m = \cos\alpha$, and $n = \sin\alpha$. Performing this transformation, we will end up with $\bar{S}_{13} = -\bar{S}_{23} = \frac{1}{2E_s}\left(L/t\right)\left(\left(L/t\right)^2 - 1\right) sin(2\theta + 4\alpha)$. Thus, $\bar{S}_{13} = -\bar{S}_{23} = 0$ gives the orientation of the principal axes as, $\alpha = k\pi/4 - \theta/2$, where k is an integer.

Similar procedure has been performed to obtain closed-form expressions of elastic moduli for tri-, anti-tri-, and anti-tetra-chiral structures and the details have been presented in **Appendices**.

1.4 Self-similar hierarchical structures

In this section we investigate the linear elastic properties of hierarchical structures. To this end, we select two representative samples, hierarchical square and hierarchical diamond; which are respectively generated by replacing the vertices of a regular square honeycomb by smaller squares and diamonds (see **Figure 1.2**). The wall thickness of the structures is simultaneously reduced to maintain the overall density equal to that of regular square honeycomb.

Similar to chiral and anti-chiral honeycombs, the structural organization of hierarchical structures can be defined by the ratio, r/L, where r and L are defined for each structure in **Figure 1.2**. This figure also represents the dimensionless relative density (i.e., area fraction) of the structures in terms of r/L and t/L. For the special case, where $r = 0$, the normalized relative density of the hexagon (hierarchical hexagonal honeycomb), and square (hierarchical square and hierarchical diamond) based hierarchical structures respectively reduce to that of regular hexagonal $(2/\sqrt{3}\ .(\mathrm{t/L}))$, and square $(2\,\mathrm{t/L})$ honeycombs.

Note that among the three hierarchical structures shown in **Figure 1.2**, Ajdari et al. [76] studied the in-plane elastic properties of hierarchical hexagonal honeycombs. Thus, in this dissertation we focus on the other two structures and just report the results published by the authors for the sake of completeness.

1.4.1 Theoretical formulations

Similar to the previous section, Castigliano's second theorem is used to derive closed-form relations for elastic properties of hierarchical structures made of an isotropic linear elastic material with Young's modulus, E_s. It should be noted that hierarchical square and

diamond structures exhibit macroscopic anisotropy. Thus, in order to completely characterize their elastic behavior we need to obtain the Young's modulus, Poisson's ratio, and shear modulus along the principal directions. To this end, first a uniaxial loading in the x-direction is applied to each structure to determine the structure's Young's modulus, E_x and Poisson's ratio, ν_{xy} and then a shearing load is imposed to obtain the shear modulus, G_{xy}. Finally the orientation of principal coordinate systems is given for each structure. In contrast to chiral and anti-chiral lattices where we assumed the cylinders to be rigid, here we assume the entire structure including smaller squares and diamonds to have a linear elastic material property.

We will obtain closed-form expressions of the elastic moduli for hierarchical square structures as a demonstration of our proposed method. The details of the procedure for hierarchical diamond structures are presented in **Appendices**.

A schematic of a hierarchical square honeycomb under a uniaxial far-field stress in the x-direction, σ_x is shown in **Figure 1.4 (A)**. A detailed FBD of the structural unit cell of this structure is shown in **Figure 1.4 (B)**. It contains a smaller square and four half ligaments connecting the smaller squares together. Due to 180^o rotational symmetry of the structure and components of microscopic stress, all external cut points of the unit cell (i.e., points 1 through 4 in **Figure 1.4 (B)**) must be moment free. Furthermore, by using a cut line Δ_1, we can see that since there is no macroscopic stress on the structure in the y-direction, the unit cell must be free of any forces in the y-direction at point 4. Similar arguments also hold true for point 2. Also note that the structure is symmetric with respect to all four cut lines shown in **Figure 1.4 (A)**. This implies that the component of forces parallel to these cut lines at corresponding external cut point must be equal to zero. Thus, under the uniaxial stress on the structure, σ_x, each unit cell experiences the loading shown in **Figure 1.4 (B)**, where F can be obtained as a function of applied stress as, $F = \sigma_x L$.

In order to determine the distribution of forces and moments at any cross section of the smaller square (needed for strain energy calculation in the next step), let us consider the right portion of the unit cell as illustrated in **Figure 1.4 (B)** (right). For equilibrium to be satisfied for forces in the x-direction, two equal forces, $F/2$ must be applied to points 5 and 6. Also, shear forces at these two points must be equal to zero due to the fact that no

macroscopic stress is being applied to the structure in the *y*-direction. Moreover, symmetry of the structure requires that the rotation of point 5 (and similarly point 6) with respect to the *z*-axis be equal to zero. Using Castigliano's theorem, this condition is equivalent to the relation, $\partial U/\partial M = 0$, where U is the total strain energy of the portion of the unit cell shown in **Figure 1.4 (B)** and M is a yet unknown moment to be determined. This constraint will result in $M = rF/8$. Now, the unit cell's strain energy can be obtained as:

$$U = 2\frac{F^2(L/2-r)}{2E_sA} + 4\frac{(F/2)^2 r}{2E_sA} + 4\frac{(rF/8)^2 r}{2E_sI} + 4\int_0^r \frac{(rF/8 - xF/2)^2}{2E_sI}dx \qquad (1.8)$$

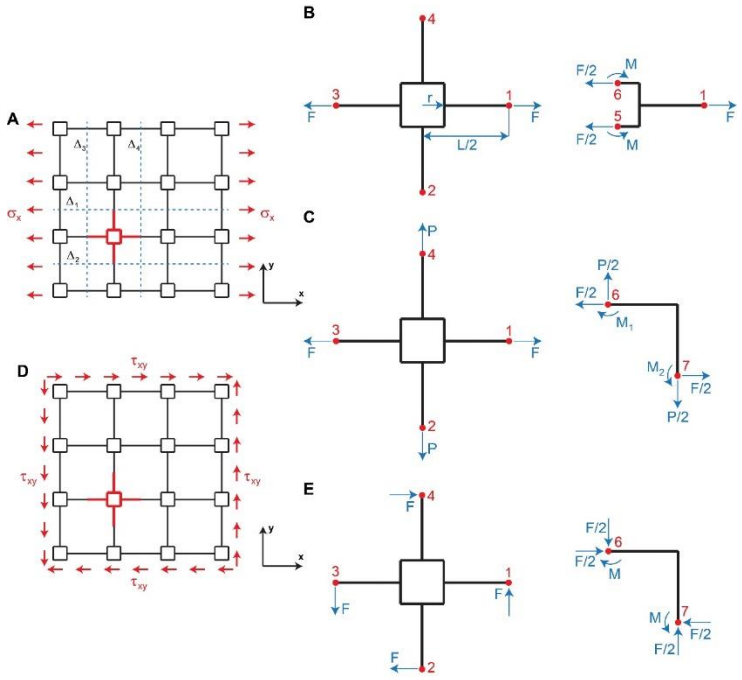

Figure 1.4 (A) Schematic of a hierarchical square honeycomb under $\boldsymbol{x}$-direction uniaxial loading. **(B)** and **(C)** Free body diagram of the structural unit cell under uniaxial loading, where *P* is a virtual force used for Poisson's ratio calculations. **(D)** Schematic of a hierarchical square honeycomb under $\boldsymbol{x}$-$\boldsymbol{y}$ shearing load. **(E)** Free body diagram of the structural unit cell under shearing load.

Using above equation, the total displacement of point 1 with respect to point 3 in the *x*-direction can be calculated as, $\delta_x = \frac{\partial U}{\partial F} = \frac{F(L-r)}{E_sA} + \frac{10Fr^3}{48E_sI}$. Next, the structure's average strain in the *x*-direction is obtained by using the relation, $\epsilon_x = \delta_x/L$. The Young's

modulus of the structure normalized by material's Young's modulus is then defined as the ratio of the average stress, σ_x and the average strain, ϵ_x and obtained as:

$$E_x/E_s = \frac{t/L}{1-(r/L)+2.5\,(r/L)^3/(t/L)^2} \tag{1.9}$$

Next, in order to calculate the Poisson's ratio, let us consider a pair of virtual forces acting on the unit cell in the lateral direction, as shown in **Figure 1.4 (C)**. One fourth of the smaller square of this unit cell is also shown in **Figure 1.4 (C)**. Similar procedure as employed earlier is used to determine the unknown moments, M_1 and M_2, acting on points 6 and 7 as $M_1 = rF/8 - 3rP/8$ and $M_2 = rP/8 - 3rF/8$. Thus, the strain energy of the unit cell is given as:

$$\begin{aligned} U = {} & 2\frac{F^2(L/2-r)}{2E_sA} + 2\frac{P^2(L/2-r)}{2E_sA} + 4\frac{(F/2)^2 r}{2E_sA} + 4\frac{(P/2)^2 r}{2E_sA} \\ & + 4\int_0^r \frac{(xF/2 + rP/8 - 3rF/8)^2}{2E_sI}\,dx \\ & + 4\int_0^r \frac{(xP/2 + rF/8 - 3rP/8)^2}{2E_sI}\,dx \end{aligned} \tag{1.10}$$

Now using Castigliano's second theorem on the strain energy calculated in **Equation (1.10)** we obtain $\delta_y = \partial U/\partial P|_{P=0} = \frac{-Fr^3}{8E_sI}$. Using this equation, we obtain $\epsilon_y = \delta_y/L$ which is the structure's average strain in the y-direction due to the uniaxial loading, σ_x. Poisson's ratio, ν_{xy} is then defined as the negative of the ratio of the average strain in the y-direction, ϵ_y to the average strain in the x-direction, ϵ_x and obtained as:

$$\nu_{xy} = \frac{0.6(r/L)^3}{(r/L)^3 - 0.4(t/L)^2(r/L) + 0.4(t/L)^2} \tag{1.11}$$

Finally, to determine the shear modulus, as shown in **Figure 1.4 (D)**, we apply a uniform far-field shear stress, τ_{xy} to the structure. A FBD of the unit cell of the structure is also shown in **Figure 1.4 (E)**. The 180^o rotational symmetry of the structure implies unit cell's all four external cut points (i.e., points 1 through 4 in **Figure 1.4 (E)**) to be moment free. Furthermore, each of these external cut points must be free of any normal forces (in

the direction of the ligament), because there is no macroscopic normal stress acting on the structure in those directions. Thus, there are only four equal shearing forces acting on the unit cell's external cut points, F, which can be obtained as a function of applying stress as, $F = \tau_{xy}L$. Next, consider one fourth of the smaller square as shown in **Figure 1.4 (E)**. Using the equilibrium equations, components of unknown forces and moment acting on the external cut points of this portion of the unit cell can be determined as functions of F, as shown in **Figure 1.4 (E)**, where $M = F/2 \cdot (L/2 - r)$. Hence, the strain energy of the unit cell can be written as:

$$U = 4\int_0^{L/2-r} \frac{(Fx)^2}{2E_sI}dx + 8\frac{(F/2)^2 r}{2E_sA} + 8\int_0^{r} \frac{(F/2\,(L/2-r) - Fx/2)^2}{2E_sI}dx \qquad (1.12)$$

Then, $(\partial U/\partial F)/L$ gives the total change of angle between two straight lines initially parallel to the x- and y-axes (i.e., the shear strain, γ_{xy}). Finally, shear modulus of the structure (G_{xy}, normalized with respect to the Young's modulus of cell walls material) is defined as the ratio of the average shear stress, τ_{xy} to the average shear strain, γ_{xy} and obtained as the following:

$$G_{xy}/E_s = \frac{0.5(t/L)^3}{1 - 3(r/L) - 6(r/L)^2 + 20(r/L)^3 + (t/L)^2(r/L)} \qquad (1.13)$$

Note that as r goes to zero, the structure transforms into a regular square honeycomb. Upon substituting $r = 0$ into **Equations (1.9)**, **(1.11)**, and **(1.13)**, we obtain $E_x/E_s = t/L$, $\nu_{xy} = 0$, and $G_{xy}/E_s = 0.5(t/L)^3$, which are the Young's modulus, Poisson's ratio, and shear modulus of a regular square honeycomb, respectively. The principal directions for the 2D compliance tensor (S_{13} and S_{23} are both equal to zero for the current x-y-z coordinate system) of this structure can be calculated as, $\alpha = k\pi/4$, where k is an integer.

Similar procedure has been performed to obtain closed-form expressions of elastic moduli for hierarchical diamond structures and demonstrated in detail in **Appendices**.

1.5 Numerical modeling

In order to validate the theoretical expressions of elastic moduli, FE-based numerical models were developed to conduct simulations on the structures. We carry out FE analysis at the structural level instead of the unit cell level with 2D models of the structures constructed using the FE software ABAQUS 6.11-2 (SIMULIA, Providence, RI). The relative characteristic length of the samples with respect to the unit cells was sufficiently large enough to mitigate boundary effects on the inner unit cells. The models were meshed using in-plane 2-node linear beam elements allowing for shear deformation (i.e., B21 beam element in ABAQUS) and a mesh sensitivity analysis was carried out to guarantee that the results were not mesh-dependent. Static-general solver of ABAQUS was used to simulate the response of these structures under uniaxial compression and shearing loads. Cell walls were assumed to have a rectangular cross section with unit length normal to the loading plane (i.e., normal to the x-y plane). R was taken to be equal to unity and the thickness (t) was adjusted to be consistent with the value of the relative density presented in **Figures 1.1** and **1.2**. Linear elastic properties of aluminum were assumed for the cell wall material with E_s=70 GPa and ν_s=0.3.

Figures 1.5 and **1.6** show the schematic diagrams of the FE models constructed in ABAQUS for simulating static uniaxial and shearing loads, as well as their corresponding exaggerated deformed configurations, for the structures with underlying hexagon and square based grids, respectively. In order to simulate the uniaxial loading, constant static displacement was assigned to the left nodes (see **Figures 1.5** and **1.6**), while the horizontal displacement of the right nodes was constrained (i.e., set to zero). Then, to eliminate any boundary effects, periodic boundary conditions were imposed on the structures on the top- and bottom-side nodes [77]. Also note that the vertical displacement of an arbitrary node was constrained (i.e., set to zero) in order to prevent rigid body motion of the structure in that direction. To simulate the square based honeycombs under shearing loads, shear forces were applied to the boundary nodes, while the horizontal and vertical displacements of an arbitrary node were constrained (i.e., set to zero) to avoid rigid body motion, **Figure 1.6**.

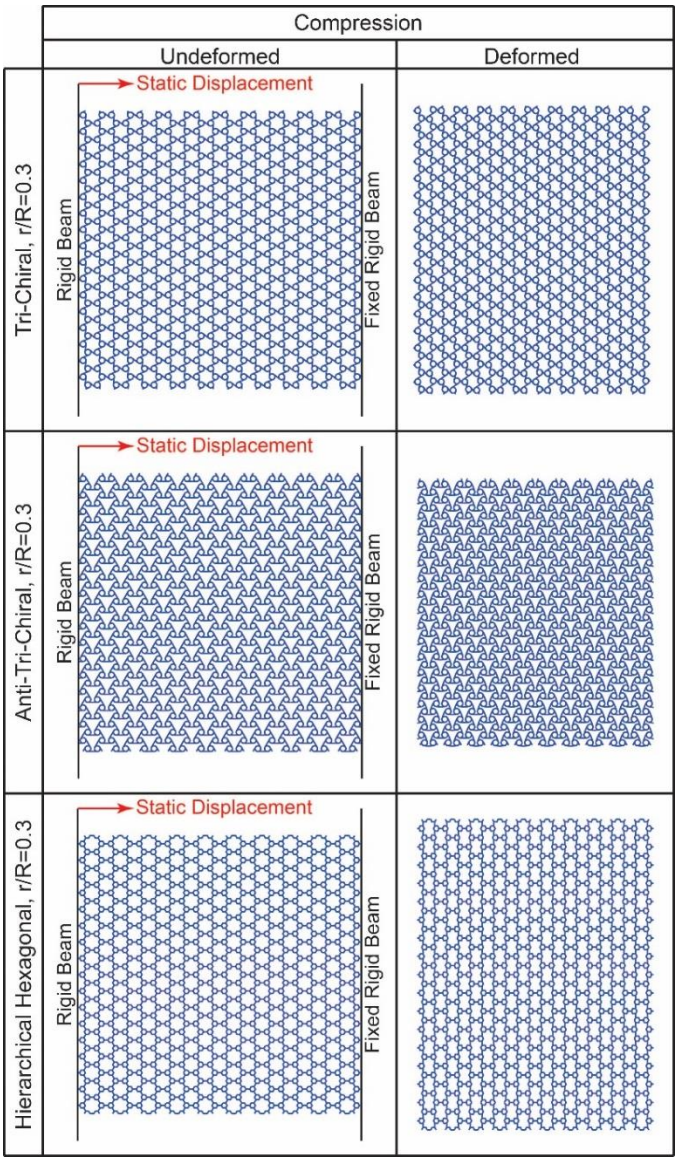

Figure 1.5 Schematic diagrams of the finite element models constructed in ABAQUS for simulating static uniaxial loads, as well as their corresponding exaggerated deformed configurations, for the structures with hexagon based grids with $r/R = 0.3$.

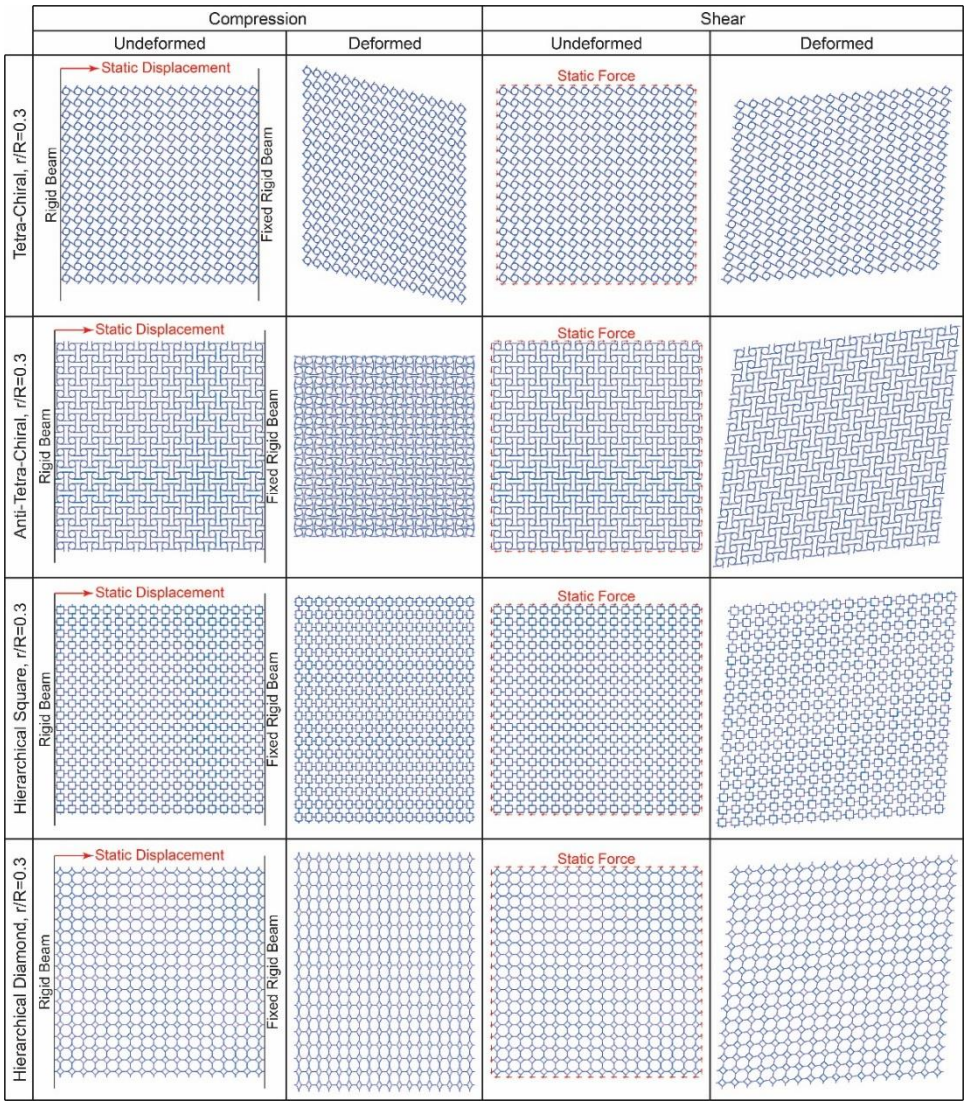

Figure 1.6 Schematic diagrams of the finite element models constructed in ABAQUS for simulating static uniaxial and shearing loads, as well as their corresponding exaggerated deformed configurations, for the structures with square based grids with $r/R = 0.3$.

1.6 Results

The analytical expressions of effective Young's modulus (Young's modulus of the structure normalized by cell wall material's Young's modulus), Poisson's ratio, and effective shear modulus (shear modulus of the structure normalized by cell wall material's Young's modulus) for the meta-lattices studied are tabulated in **Tables 1.1** and **1.2**. In **Table 1.1**, the structures are characterized into two categories - hexagon and square based honeycombs. The structural unit cell, effective Young's modulus, and Poisson's ratio for

each structure are reported in the next columns. For anisotropic structures (i.e., square based honeycombs), the effective shear modulus and material principal directions are reported in **Table 1.2**.

Table 1.1 Summary of the analytical relations for the effective Young's modulus and Poisson ratio of cellular lattices studied in this article. Asterisks (*) highlight anisotropic lattices. For these anisotropic lattices the analytical expressions for the effective shear modulus and material principal directions are given in **Table 1.2**.

	Name	Unit Cell	Effective Young's Modulus	Poisson's Ratio
Hexagon Based Honeycombs	Regular Hexagonal		$\frac{4}{\sqrt{3}}\left(\frac{t}{L}\right)^3$	1
	Hierarchical Hexagonal		$\frac{4}{\sqrt{3}}\left(\frac{t}{L}\right)^3\left(\frac{1}{1-4.7(r/L)+4.8(r/L)^2+3.87(r/L)^3}\right)$	$1-\frac{(r/L)^3}{2.9(r/L)^3+3.6(r/L)^2-3.525(r/L)+0.75}$
	Tri-Chiral		$\frac{4}{\sqrt{3}}\left(\frac{t}{L}\right)^3\left(\frac{3/2}{\cos^2(\pi/6-\theta)+4\sin^2(\theta)+\cos^2(\pi/6+\theta)}\right)$	$\sqrt{3}\left(\frac{\sin(\pi/6-\theta)\cos(\pi/6-\theta)+\sin(\pi/6+\theta)\cos(\pi/6+\theta)}{\cos^2(\pi/6-\theta)+4\sin^2(\theta)+\cos^2(\pi/6+\theta)}\right)$
	Anti-Tri-Chiral		$\frac{4}{\sqrt{3}}\left(\frac{t}{L}\right)^3\left(\frac{1}{1+24(r/L)^2}\right)$	$\frac{1-24(r/L)^2}{1+24(r/L)^2}$
Square Based Honeycombs	Square*		$\left(\frac{t}{L}\right)$	0
	Hierarchical Square*		$\frac{(t/L)}{1-(r/L)+2.5(r/L)^3/(t/L)^2}$	$\frac{0.6(r/L)^3}{(r/L)^3-0.4(t/L)^2(r/L)+0.4(t/L)^2}$
	Hierarchical Diamond*		$\frac{(t/L)}{1-(r/L)(2-1/\sqrt{2})+\sqrt{2}(r/L)^3/(t/L)^2}$	$\frac{(r/L)^3-0.5(t/L)^2(r/L)}{(r/L)^3-(\sqrt{2}-0.5)(t/L)^2(r/L)+(t/L)^2/\sqrt{2}}$
	Tetra-Chiral*		$\frac{(t/L)}{\cos^2(\theta)+\sin^2(\theta)/(t/L)^2}$	0
	Anti-Tetra-Chiral*		$\frac{(t/L)}{1+6(r/L)^2/(t/L)^2}$	$\frac{-6(r/L)^2}{6(r/L)^2+(t/L)^2}$

Table 1.2 Summary of the analytical expressions for the effective shear modulus and material principal directions for the anisotropic lattices studied.

	Name	Unit Cell	Effective Shear Modulus	Principal Direction
Square Based Honeycombs	Square		$0.5\left(\frac{t}{L}\right)^3$	$\frac{k\pi}{4}$
	Hierarchical Square		$\frac{0.5(t/L)^3}{1-3(r/L)-6(r/L)^2+20(r/L)^3+(t/L)^2(r/L)}$	$\frac{k\pi}{4}$
	Hierarchical Diamond		$\frac{0.5(t/L)^3}{(1-2(r/L))^2\left(1+(1.5\sqrt{2}-2)(r/L)\right)+\sqrt{2}(t/L)^2(r/L)}$	$\frac{k\pi}{4}$
	Tetra-Chiral		$\frac{0.5(t/L)^3}{\cos^2(\theta)+(t/L)^2\sin^2(\theta)}$	$\frac{k\pi}{4}-\frac{\theta}{2}$
	Anti-Tetra-Chiral		$0.5\left(\frac{t}{L}\right)^3$	$\frac{k\pi}{4}$

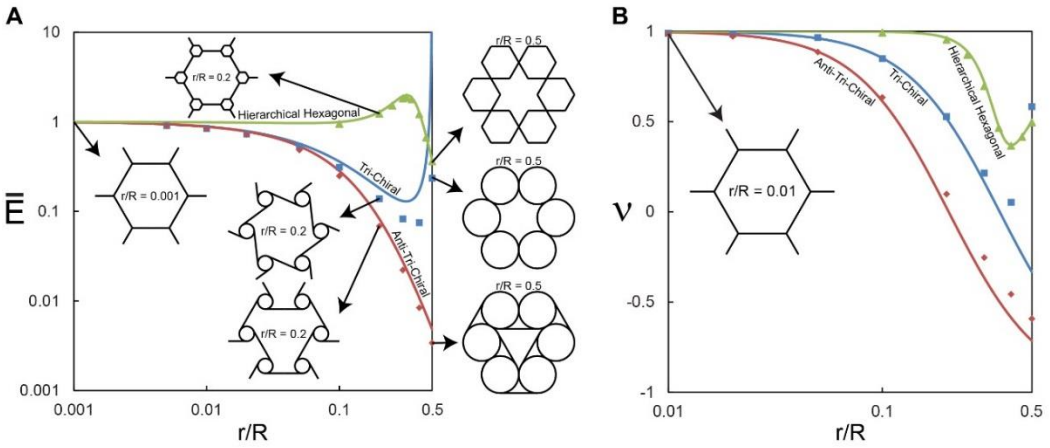

Figure 1.7 (A) Normalized Young's modulus, and **(B)** Poisson ratio as a function of geometrical parameter, r/R, for three different hexagon based hierarchical and chiral lattices. The effective Young's modulus of the structure is normalized by the effective Young's modulus of a regular hexagonal honeycomb ($r/R = 0$) with same relative density. The solid lines represent the results from the theoretical estimates (i.e. relations reported in **Table 1.1**), and circles show the finite element results.

In **Figure 1.7**, we plot the normalized Young's modulus (effective Young's modulus of the structure normalized by the effective Young's modulus of a regular hexagonal honeycomb with same relative density) (**Figure 1.7 (A)**) and the Poisson's ratio (**Figure 1.7 (B)**) of hexagon based chiral and hierarchical honeycombs varied via the r/R ratio which is a de-facto measure of the magnitude of alteration to the underlying structure. The solid lines represent the results from the analytical estimates of elastic moduli in **Table 1.1** and markers denote the FE results. Note that **Figure 1.7 (A)** is a log-log plot. Clearly as $r/R \to 0$, the chiral and hierarchical structures reduce trivially to the regular hexagonal honeycomb. A good agreement is observed between the theoretical and FE results except for tri-chiral structure where the theory predicts higher stiffness and negative Poisson's ratio when $r/R > 0.2$. This discrepancy is resulted from the assumed rigid behavior for the cylindrical components in the chiral structures. When $r/R \to 0.5$ in the tri-chiral structure, the cylindrical components become the only source of compliance for the structure as straight beams vanish, and therefore the theoretical results diverge from the FE results. Among the hexagon based structures, hierarchical hexagonal honeycomb shows higher stiffness with respect to the other structures and the normalized Young's modulus achieves the maximum value of $\bar{E} \cong 2$ at $r/R \cong 0.32$ [78]. The plot of Poisson's ratio

shown in **Figure 1.7 (B)** also shows a good agreement with the theoretical derivations presented earlier. Unlike the hierarchical structure, the chiral and anti-chiral structures are capable of showing auxetic behavior (i.e., negative Poisson's ratio) at higher r/R values. The anti-tri-chiral structure which is also the most compliant among the three exhibits auxeticity as Poisson's ratio becomes negative for r/R greater than $\cong 0.2$.

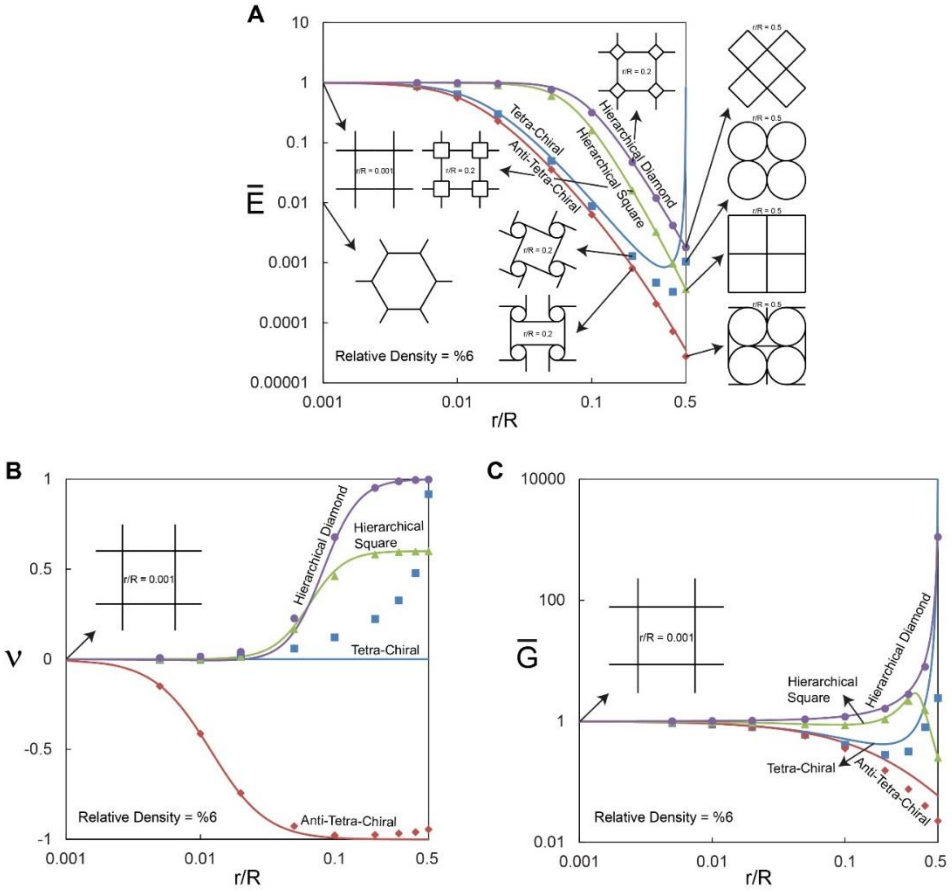

Figure 1.8 (A) Normalized Young's modulus, **(B)** Poisson ratio, and **(C)** Normalized shear modulus as a function of geometrical parameter, r/R, for four different anisotropic square based hierarchical and chiral lattices. The effective Young's and shear moduli of the structure are normalized by those of a square honeycomb ($r/R = 0$) with same relative density. The solid lines represent the results from the theoretical estimates (i.e. relations reported in **Tables 1.1** and **1.2**), and circles show the finite element results.

Figure 1.8 illustrates the behavior of square based structures which are anisotropic. Since the results for stretching dominated honeycombs depend on the relative density of the structures, we reported the results of square based honeycombs only at a constant

relative density of 6%. The solid lines in these figures represent the results from the closed-form estimates of elastic moduli from **Tables 1.1** and **1.2**, and markers denote the FE results. Similar to hexagon based honeycombs, there exist discrepancies between the theoretical and numerical results of square based structures in the case of chiral and anti-chiral lattices, which become more pronounced for tetra-chiral structure as r/R goes to 0.5. Again, these discrepancies stem from the assumed rigid behavior for the cylindrical components in the chiral and anti-chiral structures. We plot the normalized Young's modulus of the structure (effective Young's modulus of the structure normalized by the effective Young's modulus of a square honeycomb with same relative density) in **Figure 1.8 (A)** and notice a good agreement with FE results. Clearly, increasing r/R results in a sharp decrease in the in-plane stiffness of these structures which is especially pronounced in tetra- and anti-tetra-chiral lattices. Of all the square based structures studied, only anti-tetra-chiral honeycombs exhibit auxeticity for all values of r/R. In this structure, the Poisson's ratio starts to change quite appreciably with even small changes in r/R, then accelerates towards lesser values of r/R and finally reaches a plateau. On the other hand, although the tetra-chiral structure, along with the hierarchical structures show little initial sensitivity to the variations in r/R, at around $r/R \cong 0.03$, their behaviors begin to sharply diverge. The hierarchical structures show a rapid change followed by plateaus whereas the tetra-chiral structure starts with a slower variation which accelerates sharply as $r/R \to 0.5$ due to the effect of compliance of the cylinders as mentioned above. Finally **Figure 1.8 (C)** plots the variation of normalized shear modulus (effective shear modulus of the structure normalized by the effective shear modulus of a square honeycomb with same relative density) of these anisotropic structures. The normalized shear moduli of the two chiral and two hierarchical structures show little initial sensitivity to variation of r/R. However, soon at about $r/R \cong 0.01$, these two groups diverge completely in opposite directions unlike previous elastic constants. The chiral structures show increasingly low normalized shear modulus as r/R is increased whereas an increase in r/R positively affects the normalized shear modulus of the hierarchical structures. The trend for tetra-chiral structure changes course at an r/R of about 0.25 as the structure becomes increasingly stiff in shear, causing a rapid increase as $r/R \to 0.5$.

Table 1.3 Our theoretical and numerical results vs. numerical and experimental data available in the literature [46].

	Young's Modulus (MPa)				Poisson's Ratio			
Name	Theory	FE	FE [46]	EXP [46]	Theory	FE	FE [46]	EXP [46]
Tri-Chiral	0.63	0.48	0.65	1.10	+0.57	+0.57	+0.60	+0.68
Anti-Tri-Chiral	0.41	0.34	0.39	0.61	+0.02	+0.11	+0.06	+0.08
Tetra-Chiral	2.45	1.64	12.01	7.08	0.00	+0.20	-0.83	-0.26
Anti-Tetra-Chiral	1.42	1.32	2.50	3.11	-0.99	-0.96	-0.98	-0.98

Next, we compare our results with numerical and experimental data available in the literature. We choose the reported data from Alderson et al. [46] who carried out numerical and experimental analysis on the in-plane elastic properties of chiral and anti-chiral honeycombs subjected to uniaxial loading for small deformations. They employed selective laser sintering rapid-prototyping technique to fabricate the experimental samples out of nylon powder with geometrical parameters $r = 5mm$, $L = 25mm$, $t = 1.5mm$, and out-of-plane depth $d = 25mm$. **Table 1.3** compares our results with their numerical and experimental data. From this table we find favorable comparisons of our elastic constants (Young's modulus and Poisson's ratio) for almost all chirality except the tetra-chiral case. Note that some discrepancy is natural both due to the difference in the materials between the two cases and also from the different boundary conditions employed between the two FE models. Specifically, in contrast to our periodic boundary conditions imposed on the FE models at structural level, they employed slightly different non-periodic boundary conditions at the "RVE level" which led to a stiffening effect on the RVEs. For instance, for tri- and anti-tri-chiral honeycombs, instead of applying appropriate forces and moments on the RVE's edge nodes to simulate the uniaxial loading on a periodic structure, they used geometrical constraints (i.e., coupling interaction between RVE's edge nodes) to relate the displacements of particular edge nodes within the RVE. We believe that this difference may play an even greater role in the relatively large discrepancy between the results obtained for the case of tetra-chiral honeycombs. Interestingly, for this particular case, Alderson et al. [46] report auxeticity for this structure at small strains through both FE and experimental investigations (**Table 1.3**) whereas neither our theoretical prediction, nor FE simulations as seen in **Figure 1.6** show any auxeticity for this case.

1.7 Conclusions

We studied the effects of chirality and hierarchy, generally a hallmark of natural materials, on the static in-plane properties of a selected set of 2D honeycombs. Analytical closed-form formulas for square and hexagon based networks have been obtained, and the results are verified numerically. Comprehensive design graphs, comparing elastic moduli (Young's and shear moduli and Poisson's ratio) are provided. We find that both chirality and hierarchy crucially affect the in-plane mechanical properties of these structures. Overall, hierarchical structures are stiffer and have higher Poisson's ratio than their chiral counterparts for similar values of the r/R ratio which quantifies the amount of hierarchy or chirality. However, chirality remains the only route to auxeticity. This is due to the deformation mechanism observed in auxetic chiral and anti-chiral honeycombs. This mechanism is characterized by the rotation of cylindrical nodes and bending of the ligaments, which make the structures contract in the transverse direction when subjected to uniaxial compressive loads. The behavior of the elastic constants of anti-tetra-chiral structure shows a remarkable glimpse of an engineered material which can simultaneously exhibit anisotropy, auxeticity, and a shear modulus that is much lower than usual solids.

1.8 Appendices

1.A Tri-chiral

A schematic of a tri-chiral honeycomb derived from a regular hexagonal architecture undergoing an in-plane uniaxial far-field (macroscopic) loading in the *x*-direction characterized by the normal stress, σ_x is shown in **Figure 1.A.1 (A)**. A detailed free body diagram (FBD) of the structural unit cell of this honeycomb is shown in **Figure 1.A.1 (B)**. The unit cell contains a cylinder (node) which is assumed to be rigid and three half ligaments. Due to the 180^o rotational symmetry of the structure and the components of the microscopic stresses, all three external cut points of the unit cell (i.e., points 1 through 3 in **Figure 1.A.1 (B)**) must be moment-free under an arbitrary macroscopic stress state. Therefore, utilizing the equilibrium conditions of forces and moments, the horizontal force,

F, can be related to the far-field stress as, $F = \sigma_x R\sqrt{3}/2$, where R is the center to center distance of adjacent cylinders in the structure, as shown in **Figure 1.A.1 (B)**. The vertical force, P is a virtual force which will be used later in this subsection to compute the Poisson's ratio of the structure. Under the influence of this force system, neglecting the stretching and shearing terms, the strain energy stored in the unit cell of this bending dominated structure can be obtained as:

$$U = 1/(2E_s I)\left\{\int_0^{L/2}\left((F\cos(\pi/6+\theta) - P\sin(\pi/6+\theta))x\right)^2 dx + \int_0^{L/2}\left((2F\sin(\theta))x\right)^2 dx + \int_0^{L/2}\left((F\cos(\pi/6-\theta) - P\sin(\pi/6-\theta))x\right)^2 dx\right\} \quad (1.A.1)$$

where E_s (as mentioned earlier) is the Young's modulus of the cell wall material, I is the second moment of area of the wall's cross section (cell walls are assumed to have a rectangular cross section with uniform thickness, t, and unit depth, i.e., $I = t^3/12$), and $\theta = tan^{-1}(2r/L)$ is the angle between each ligament and the line connecting the centers of two adjacent cylinders as shown in **Figure 1.A.1 (B)**. Setting $P = 0$ in **Equation (1.A.1)** and using Castigliano's second theorem [72], $\partial U/\partial F$ gives the total displacement (δ_x) of points 1 and 2 (with respect to point 3) in the x-direction. Then the average strain of the structure in the x-direction is obtained by using the relation, $\epsilon_x = \delta_x/1.5R$. The effective Young's modulus of the structure (normalized by material's Young's modulus, E_s) is then defined as the ratio of the average stress, σ_x, and the average strain, ϵ_x, and obtained as:

$$E/E_s = 4/\sqrt{3}\,(t/L)^3\{1.5/(\cos^2(\pi/6-\theta) + 4\sin^2(\theta) + \cos^2(\pi/6+\theta))\} \quad (1.A.2)$$

Note that as r goes to zero, θ also approaches zero and the structure is reduced to a regular hexagonal honeycomb. Thus, letting $\theta = 0$ in **Equation (1.A.2)** will result in $E/E_s = 4/\sqrt{3}\,(t/L)^3$, which is a familiar result for the effective Young's modulus of a regular hexagonal honeycomb [75].

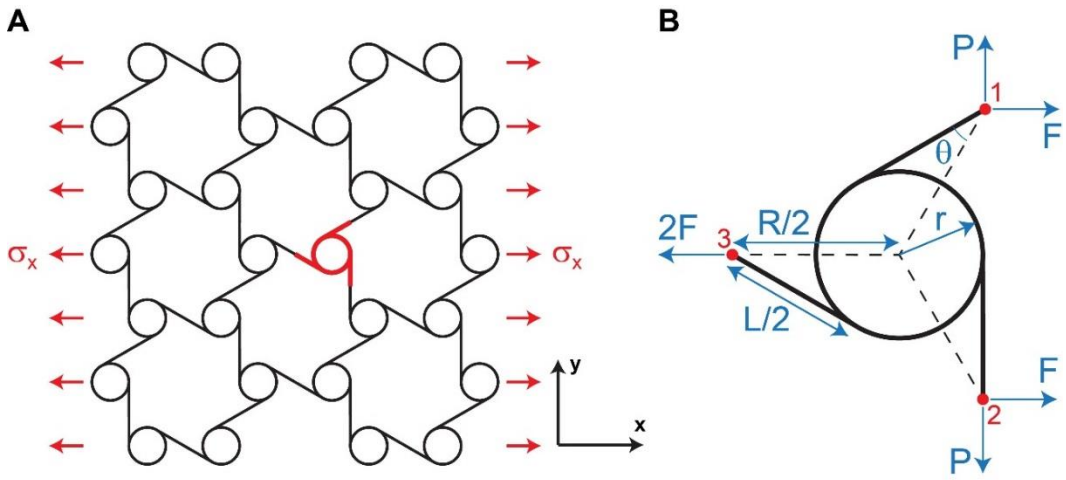

Figure 1.A.1 (A) Schematic of a tri-chiral honeycomb under x-direction uniaxial loading. **(B)** Free body diagram of the structural unit cell.

Next, to completely characterize the elastic behavior of tri-chiral honeycomb, we also need to determine its Poisson's ratio, ν. We again used Castigliano's second theorem to obtain the displacement between points 1 and 2 (δ_y) (see **Figure 1.A.1 (B)**) in the direction of the virtual forces as, $\delta_y = \partial U/\partial P|_{P=0}$. Using this relation we obtain $\epsilon_y = \delta_y/\left(R\sqrt{3}/2\right)$ which gives the structure's average strain in the y-direction due to the uniaxial loading, σ_x in the x-direction. The effective Poisson's ratio, ν, of the structure is finally defined as the negative of the ratio of the average strain in the y-direction, ϵ_y, to the average strain in the x-direction, ϵ_x, and obtained as the following:

$$\nu = \sqrt{3}\frac{(\sin(\pi/6-\theta)\cos(\pi/6-\theta)+\sin(\pi/6+\theta)\cos(\pi/6+\theta))}{\cos^2(\pi/6-\theta)+4\sin^2(\theta)+\cos^2(\pi/6+\theta)} \qquad (1.A.3)$$

Again, note that as r goes to zero, **Equation (1.A.3)** reduces to $\nu = 1$, which is the effective Poisson's ratio of a regular hexagonal honeycomb [75].

1.B Anti-tri-chiral

A schematic of an anti-tri-chiral structure which is also derived from an underlying hexagonal unit cell architecture is shown in **Figure 1.B.1 (A)**. An in-plane uniaxial far-field loading characterized by the normal stress, σ_x is applied to the structure in the x-

direction. A detailed FBD of the structural unit cell is also shown in **Figure 1.B.1 (B)**. It contains a rigid cylinder (node) and three half ligaments. As shown in **Figure 1.B.1 (A)**, by using a cut line Δ_1, since there is no macroscopic stress to the structure in the y-direction, the unit cell must be free of any forces in the y-direction at point 1. Similar argument holds true for point 2 (by using the cut line Δ_2 in **Figure 1.B.1 (A)**). Furthermore, due to the symmetry of the structure with respect to the cut line Δ_3 (see **Figure 1.B.1 (A)**), point 3 must also be free of any forces in the y-direction. Then, using the zigzag cut line Δ_4 shown in **Figure 1.B.1 (A)** and due to the symmetry of the structure mentioned above; points 1 and 2 must experience same forces in the x-direction and same moments with respect to the z-axis. Thus, the forces and moments acting on the external cut points of the unit cell are reduced as shown in **Figure 1.B.1 (B)** (recall from previous section that the virtual force P has been applied to calculate the Poisson's ratio and can be treated as zero in this part of the calculation). Note that the x-component of the force applied to point 3 (i.e., $2F$) comes from the equilibrium of forces in the x-direction. Now, the equilibrium of moments in the z-direction gives $2M + M^* - 3rF = 0$, where M and M^* are two yet unknown moments at external cut points of the unit cell as a result of the loading on the structure. Using this equation and neglecting the stretching and shearing terms, the strain energy stored in the unit cell is obtained as:

$$U = 1/(2E_sI)\left\{\int_0^{L/2}(2M - 3rF)^2dx + \int_0^{L/2}(M + Fx\sqrt{3}/2)^2dx + \int_0^{L/2}(M - Fx\sqrt{3}/2)^2dx\right\} \quad (1.B.1)$$

Now, for all horizontal lines of the structure to remain parallel in the deformed state, we can show that the following geometrical condition must hold: $\theta_1 = -\theta_2$, where θ_1 and θ_2 are respectively the total rotations of points 1 and 2 with respect to the z-axis. Using Castigliano's theorem, this geometrical condition is equivalent to the relation, $\partial U/\partial M = 0$. Now, substituting into this equation the strain energy given by **Equation (1.B.1)**, M is determined as a function of F as $M = rF$. Also using equation of equilibrium for the moments given earlier, M^* is obtained as $M^* = rF$. Next, substituting the values

obtained for unknown moments M and M^* into **Equation (1.B.1)**, the strain energy stored in the unit cell can be written as:

$$U = 1/(2E_sI)\left\{\int_0^{L/2}(rF)^2dx + \int_0^{L/2}(rF + Fx\sqrt{3}/2)^2dx + \int_0^{L/2}(rF - Fx\sqrt{3}/2)^2dx\right\} \quad (1.B.2)$$

where F can be obtained as a function of the applying stress, σ_x as $F = L\sigma_x\sqrt{3}/2$.

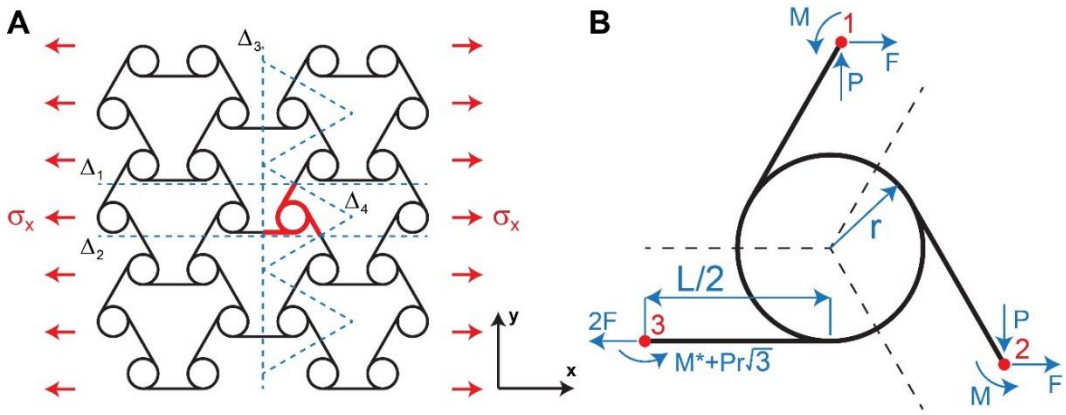

Figure 1.B.1 (A) Schematic of an anti-tri-chiral honeycomb under x-direction uniaxial loading. **(B)** Free body diagram of the structural unit cell.

Using Castigliano's second theorem, $\partial U/\partial F$ gives the total displacements of points 1 and 2 (with respect to point 3) in the loading direction as, $\delta_x = \frac{FL(L^2+24r^2)}{16E_sI}$. Furthermore, the structure's average strain in the x-direction is obtained by using the relation, $\epsilon_x = \delta_x/1.5L$. The effective Young's modulus of the structure (normalized by material's Young's modulus, E_s) is then defined as the ratio of the average stress, σ_x and the average strain, ϵ_x and obtained as:

$$E/E_s = 4/\sqrt{3}\,(t/L)^3/(1 + 24(r/L)^2) \quad (1.B.3)$$

In the remaining part of this subsection, in order to obtain the Poisson's ratio of the structure we add two virtual forces, P acting on points 1 and 2 of the unit cell, as shown in

Figure 1.B.1 (B). Note that for the unit cell to remain in the static equilibrium state, we also need to add a virtual moment ($Pr\sqrt{3}$) with respect to the *z*-axis acting on point 3. Thus, the strain energy stored in the unit cell will be modified as follows:

$$U = 1/(2E_sI)\left\{\int_0^{L/2}(rF + Pr\sqrt{3})^2dx + \int_0^{L/2}(rF + Fx\sqrt{3}/2 - Px/2)^2dx + \int_0^{L/2}(rF - Fx\sqrt{3}/2 + Px/2)^2dx\right\} \quad (1.B.4)$$

Next, we use Castigliano's second theorem to obtain the total displacement of points 1 and 2 (see **Figure 1.B.1 (B)**) in the direction of the virtual forces as, $\delta_y = \partial U/\partial P|_{P=0}$. Using **Equation (1.B.4)**, δ_y is obtained as, $\delta_y = \frac{FL\sqrt{3}(24r^2-L^2)}{48E_sI}$. Then, using this equation, $\epsilon_y = \delta_y/\left(L\sqrt{3}/2\right)$ gives the structure's average strain in the *y*-direction due to the uniaxial loading in the x-direction (σ_x). The effective Poisson's ratio, ν of the structure is then defined as the negative of the ratio of the average strain in the y-direction, ϵ_y to the average strain in the x-direction, ϵ_x and given as follows:

$$\nu = \frac{1 - 24(r/L)^2}{1 + 24(r/L)^2} \quad (1.B.5)$$

Note that similar to the tri-chiral structure, here as r goes to zero, the structure transforms into a regular hexagonal honeycomb. Letting $r = 0$ in **Equations (1.B.3)** and **(1.B.5)** will result in $E/E_s = 4/\sqrt{3}\,(t/L)^3$, and $\nu = 1$, which are the effective Young's modulus and Poisson's ratio of a regular hexagonal honeycomb, respectively, as noted earlier.

1.C Anti-tetra-chiral

We now turn our attention to the next alteration of the square based unit cell which is an anti-tetra-chiral structure. Note that the Young's modulus and Poisson's ratio of the anti-tetra-chiral lattice with square and rectangle based networks have been analytically

determined assuming the square based anti-tetra-chiral lattice (i.e., when all straight beams having identical lengths) is macroscopically isotropic [33]. In contrast, in the current paper we will show that the square anti-tetra-chiral structure is macroscopically orthotropic (i.e., having four-fold rotational symmetry and defined by three in-plane materials constants), and will derive analytical relations for the shear modulus and the material's principal directions.

An anti-tetra-chiral structure is depicted schematically in **Figure 1.C.1 (A)** under a uniaxial far-field stress in the x-direction, σ_x. FBD of a representative unit cell of the structure is shown in **Figure 1.C.1 (B)**. It contains a rigid cylinder (node) and four half ligaments. The 180° rotational symmetry of the structure and loading, requires that any two external cut points (i.e., points 1 through 4 in **Figure 1.C.1 (B)**) located opposite to each other in the unit cell experience same forces and moments. Then, using the cut line Δ_1, since there is no macroscopic stress applied to the structure in the y-direction, the unit cell must be forceless in that direction at point 4. Similar statement holds true for point 2, by using the cut line Δ_2. Also note that the component of forces parallel to each cut line at corresponding external cut point of the unit cell must be equal to zero, because no macroscopic shear stress acts on the structure. Thus, under this uniaxial stress on the structure, σ_x, each unit cell experiences the loading shown in **Figure 1.C.1 (B)** (for instance neglect the terms containing P in the forces and moments), where F can be given as a function of applied stress as, $F = \sigma_x L$. Also, M and M^* are two yet unknown moments to be determined. Then, equilibrium of moments with respect to the z-axis gives $M + M^* - rF = 0$. Using this equation and neglecting the shearing terms, the strain energy of the unit cell can be written as, $U = 2\frac{F^2 L/2}{2E_S A} + 2\int_0^{L/2} \frac{M^2}{2E_S I} dx + 2\int_0^{L/2} \frac{(rF-M)^2}{2E_S I} dx$. Next, for all horizontal lines in the structure to remain parallel in the deformed state, the following condition must hold: $\frac{\partial U}{\partial M} = 0$. Upon substituting the strain energy into this equation, M is obtained as a function of F as $M = rF/2$. Then, using the equation of equilibrium of moments given earlier, M^* is also obtained as $M^* = rF/2$. Then, substituting the values obtained for unknown moments, M and M^* into the equation of strain energy, it will be modified as $U = 2\frac{F^2 L/2}{2E_S A} + 4\frac{(rF/2)^2 L/2}{2E_S I}$. Using Castigliano's theorem, $\partial U/\partial F$ gives the

total displacement of point 1 with respect to the point 3 in the *x*-direction as $\delta_x = \frac{FL}{E_s A} + \frac{Fr^2 L}{2E_s I}$. Then the structure's average strain in the x-direction is given by using the relation, $\epsilon_x = \delta_x / L$. The effective Young's modulus of the structure (normalized by material's Young's modulus, E_s) is then defined as the ratio of the average stress, σ_x and the average strain, ϵ_x and obtained as:

$$E_x / E_s = \frac{t/L}{1 + 6(r/L)^2/(t/L)^2} \tag{1.C.1}$$

Next, in order to obtain the Poisson's ratio of the structure, we add two virtual forces of magnitude *P* acting on points 2 and 4 as shown in **Figure 1.C.1 (B)** to be able to find the elongation of the unit cell in the y-direction. Note that for the unit cell to remain in the equilibrium state, we must include virtual moments, $rP/2$, with respect to the z-axis acting on points 1 through 4 (see **Figure 1.C.1 (B)**). Thus, the strain energy of the unit cell will be modified into: $U = 2\frac{F^2 L/2}{2E_s A} + 2\frac{P^2 L/2}{2E_s A} + 4\frac{(rF/2 + rP/2)^2 L/2}{2E_s I}$. Then, using Castigliano's theorem, the displacement of point 4 with respect to point 2 in the y-direction can be obtained as, $\delta_y = \frac{Fr^2 L}{2E_s I}$. Using this equation, $\epsilon_y = \delta_y / L$ gives the structure's average strain in the y-direction due to the uniaxial loading, σ_x. The effective Poisson's ratio of the structure is then defined as the negative of the ratio of the average strain in the y-direction, ϵ_y to the average strain in the x-direction, ϵ_x and obtained as follows:

$$\nu_{xy} = \frac{-6(r/L)^2}{6(r/L)^2 + (t/L)^2} \tag{1.C.2}$$

Finally, to determine the shear modulus, as shown in **Figure 1.C.1 (C)**, consider an anti-tetra-chiral structure under a uniform far-field shear stress, τ_{xy}. A representative unit cell of the structure is also shown in **Figure 1.C.1 (D)**. Similar to tetra-chiral honeycombs studied in the dissertation, we can show that under the shearing load, τ_{xy}, the unit cell must experience the loading shown in **Figure 1.C.1 (D)**, where F can be obtained as a function of applying stress as, $F = \tau_{xy} L$. Thus, the unit cell's strain energy is obtained as $U =$

$4\int_0^{L/2}\frac{(Fx)^2}{2E_sI}dx$. Then, $(\partial U/\partial F)/L$ gives the total change of angle (i.e., the shear strain, γ_{xy}) between two straight lines initially parallel to the x- and y-axes. Finally, the effective shear modulus of the structure (G_{xy}, normalized with respect to the Young's modulus of cell wall material) is defined as the ratio of the average shear stress, τ_{xy} to the average shear strain, γ_{xy} and obtained as the following:

$$G_{xy}/E_s = 0.5(t/L)^3 \tag{1.C.3}$$

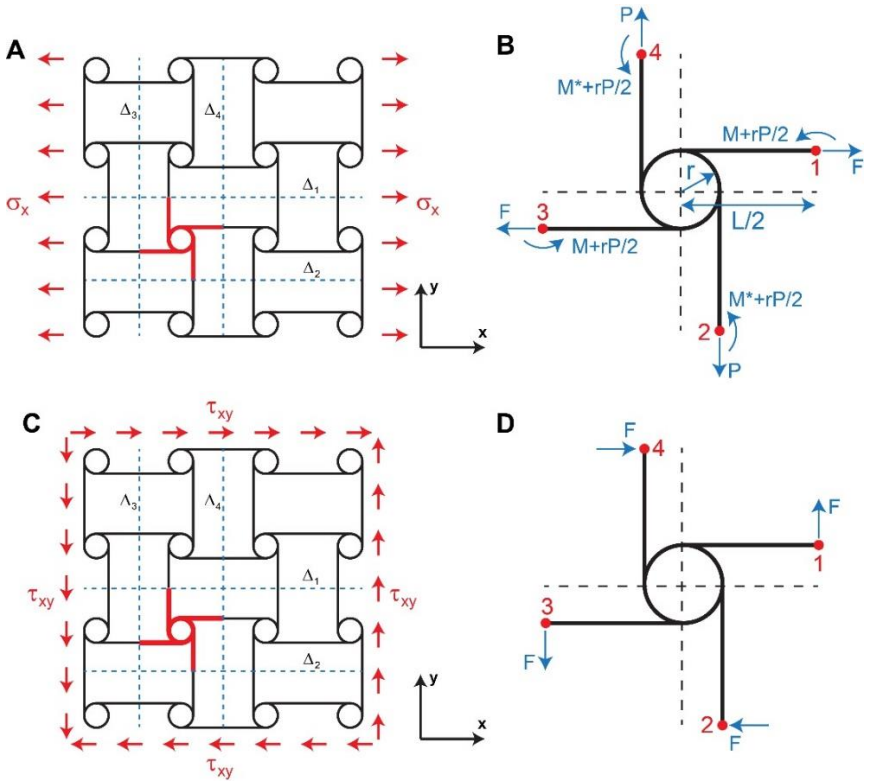

Figure 1.C.1 (A) Schematic of an anti-tetra-chiral honeycomb under x-direction uniaxial loading. **(B)** Free body diagram of the structural unit cell under uniaxial loading. **(C)** Schematic of an anti-tetra-chiral honeycomb under x-y shearing load. **(D)** Free body diagram of the structural unit cell under shearing load.

Note that as r goes to zero, the structure transforms into a regular square honeycomb. Upon substituting $r = 0$ into **Equations (1.C.1)-(1.C.3)**, we get $E_x/E_s = t/L$, $\nu_{xy} = 0$, and $G_{xy}/E_s = 0.5(t/L)^3$, which are the Young's modulus, Poisson's ratio, and shear modulus of a regular square honeycomb, respectively. Employing the same

procedure as outlined in the paper yields the principal directions for the two-dimensional compliance tensor of this honeycomb as $k\pi/4$, where k is an integer.

1.D Hierarchical diamond

We now turn our attention to determining the linear elastic constants of hierarchical diamond structure. **Figure 1.D.1 (A)** shows a hierarchical diamond structure under a uniaxial far-field stress in the *x*-direction, σ_x. The corresponding FBD of the unit cell is shown in **Figure 1.D.1 (B)**. It contains a diamond and four half ligaments connecting the diamonds together. Similar to the previous section, under a uniaxial stress on the structure, σ_x, each unit cell experiences the loading shown in **Figure 1.D.1 (B)**, where F can be obtained as a function of applied stress as, $F = \sigma_x L$. Consider the right portion of the unit cell as shown in **Figure 1.D.1 (B)**. Unknown forces and moment acting on points 5 and 6 of the unit cell are obtained by satisfying the equilibrium conditions discussed earlier. M is found to be $M = rF/4$. Then, using this equation, the unit cell's strain energy is obtained as:

$$U = 2\frac{F^2(L/2 - r)}{2E_s A} + 4\frac{\left(F\sqrt{2}/4\right)^2 r\sqrt{2}}{2E_s A} + 4\int_0^{r\sqrt{2}} \frac{\left(rF/4 - xF\sqrt{2}/4\right)^2}{2E_s I}\,dx \qquad (1.D.1)$$

Using above equation we can obtain the total displacement of point 1 with respect to point 3 in the x-direction as $\delta_x = \frac{\partial U}{\partial F} = \frac{F\left(L - r\left(2 - 1/\sqrt{2}\right)\right)}{E_s A} + \frac{\sqrt{2}Fr^3}{12E_s I}$. Next, the structure's average strain in the x-direction is obtained by using the relation $\epsilon_x = \delta_x/L$. The effective Young's modulus of the structure (normalized by material's Young's modulus, E_s) is then defined as the ratio of the average stress, σ_x and the average strain, ϵ_x and obtained as:

$$E_x/E_s = \frac{t/L}{1 - (r/L)\left(2 - 1/\sqrt{2}\right) + \sqrt{2}\,(r/L)^3/(t/L)^2} \qquad (1.D.2)$$

Next, in order to obtain the Poisson's ratio, consider a pair of virtual forces acting on the unit cell in the lateral direction, as shown in **Figure 1.D.1 (C)**. One fourth of the diamond is also shown in **Figure 1.D.1 (C)**. Similar procedure is used to determine the

unknown moments (M_1 and M_2) acting on points 6 and 7. M_1 and M_2 are obtained as $M_1 = -M_2 = rF/4 - rP/4$. Then, the strain energy of the unit cell is given as:

$$U = 2\frac{F^2(L/2-r)}{2E_sA} + 2\frac{P^2(L/2-r)}{2E_sA} + 4\frac{\left((F+P)\sqrt{2}/4\right)^2 r\sqrt{2}}{2E_sA} + 4\int_0^{r\sqrt{2}} \frac{\left(\left(r/4 - x\sqrt{2}/4\right)(P-F)\right)^2}{2E_sI}\,dx \quad (1.D.3)$$

Castigliano's second theorem states that the total displacement of points 2 and 4 in the direction of virtual forces can be obtained using the relation, $\delta_y = \partial U/\partial P|_{P=0}$. Substituting **Equation (1.D.3)** into this equation gives, $\delta_y = \frac{Fr}{\sqrt{2}E_sA} - \frac{\sqrt{2}Fr^3}{12E_sI}$. Then, using this equation, $\epsilon_y = \delta_y/L$ gives the structure's average strain in the *y*-direction due to the uniaxial loading, σ_x. The effective Poisson's ratio of the structure is then defined as the negative of the ratio of the average strain in the *y*-direction, ϵ_y to the average strain in the x-direction, ϵ_x and obtained as the following:

$$\nu_{xy} = \frac{(r/L)^3 - 0.5(t/L)^2(r/L)}{(r/L)^3 - \left(\sqrt{2}-0.5\right)(t/L)^2(r/L) + (t/L)^2/\sqrt{2}} \quad (1.D.4)$$

Finally, to determine the shear modulus, as shown in **Figure 1.D.1 (D)**, we apply a uniform far-field shear stress, τ_{xy} to a typical hierarchical diamond honeycomb. FBD of the unit cell is also shown in **Figure 1.D.1 (E)**. Likewise the previous section, there are only four equal shear forces acting on the unit cell's external cut points, F, which can be obtained as a function of applying stress as, $F = \tau_{xy}L$. Next, consider one fourth of the diamond as shown in **Figure 1.D.1 (E)**. Components of unknown forces and moment acting on the external cut points of this portion of the unit cell can be determined as functions of F, as shown in **Figure 1.D.1 (E)**, where $M = {}^{F}/_{2}\,(L/2-r)$. Hence, the strain energy of the unit cell is obtained as:

$$U = 4\int_0^{L/2-r} \frac{(Fx)^2}{2E_sI}\,dx + 4\frac{\left(F/\sqrt{2}\right)^2 r\sqrt{2}}{2E_sA} + 4\int_0^{r\sqrt{2}} \frac{\left(F/2\,(L/2-r)\right)^2}{2E_sI}\,dx \quad (1.D.5)$$

Then, $(\partial U/\partial F)/L$ gives the total change of angle (i.e., the shear strain, γ_{xy}) between two straight lines initially parallel to the x- and y-axes. Finally, the effective shear modulus of the structure (G_{xy}, normalized with respect to the Young's modulus of cell walls material) is defined as the ratio of the average shear stress, τ_{xy} to the average shear strain, γ_{xy} and obtained as the following:

$$G_{xy}/E_s = \frac{0.5(t/L)^3}{\left(1-2(r/L)\right)^2\left(1+\left(1.5\sqrt{2}-2\right)(r/L)\right)+\sqrt{2}(t/L)^2(r/L)} \tag{1.D.6}$$

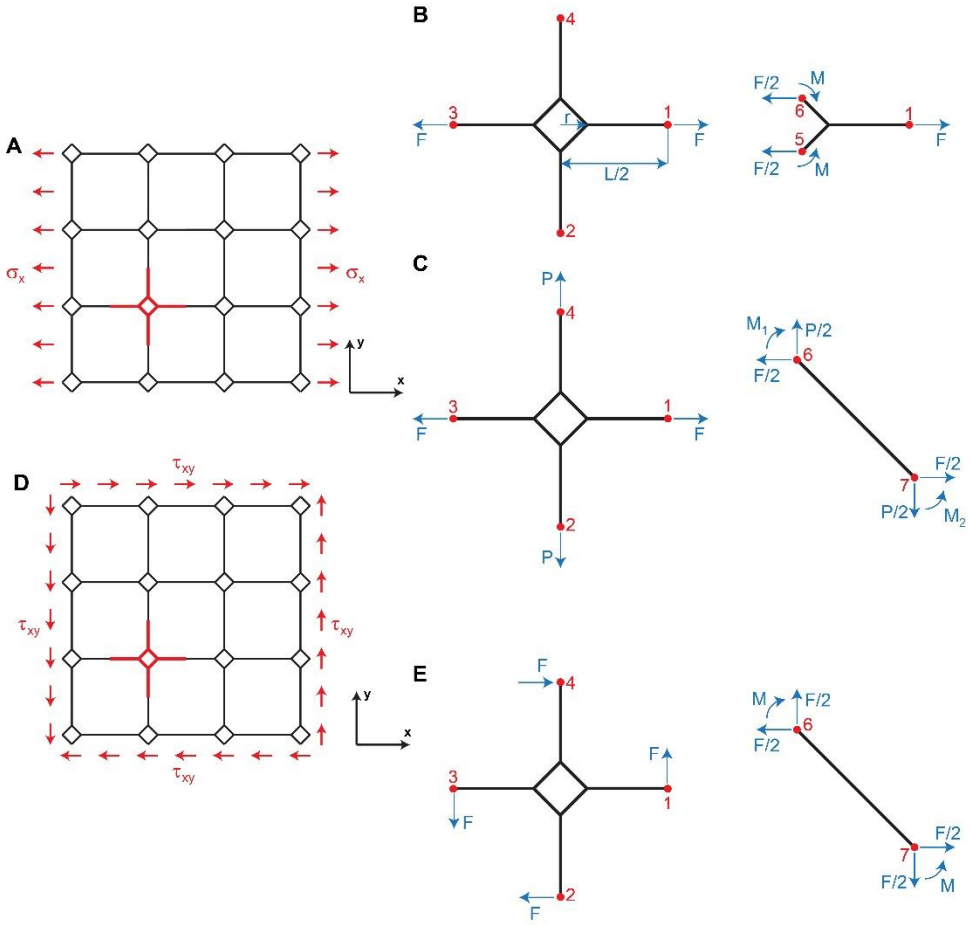

Figure 1.D.1 (A) Schematic of a hierarchical diamond honeycomb under x-direction uniaxial loading. **(B)** and **(C)** Free body diagram of the structural unit cell under uniaxial loading, where P is a virtual force used for Poisson's ratio calculations. **(D)** Schematic of a hierarchical diamond honeycomb under x-y shearing load. **(E)** Free body diagram of the structural unit cell under shearing load.

Note that as r goes to zero, the structure transforms into a regular square honeycomb. Upon substituting $r = 0$ into **Equations (1.D.2), (1.D.4)**, and **(1.D.6)**, we get $E_x/E_s = t/L,\ \nu_{xy} = 0,$ and $G_{xy}/E_s = 0.5(t/L)^3$, which are the Young's modulus, Poisson's ratio, and shear modulus of a regular square honeycomb, respectively. The principal directions for the two-dimensional compliance tensor of this structure are $\alpha = k\pi/4$, where k is an integer.

Chapter 2

Spiderweb Honeycombs

2.1 Abstract

Small and large deformation in-plane elastic response of a new class of hierarchical fractal-like honeycombs inspired by the topology of the "spiderweb" were investigated through analytical modeling, detailed numerical simulations, and mechanical testing. Small deformation elasticity results show that the isotropic in-plane elastic moduli (Young's modulus and Poisson's ratio) of the structures are controlled by dimension ratios in the hierarchical pattern of spiderweb, and the response can vary from bending to stretching dominated. In large deformations, spiderweb hierarchy postpones the onset of instability compared to stretching dominated triangular honeycomb (which is indeed a special case of the proposed spiderweb honeycomb), and exhibits hardening behavior due to geometrical nonlinearity. Furthermore, simple geometrical arguments were obtained for large deformation Poisson's ratio of first order spiderweb honeycombs, which show good agreement with numerical and experimental results. Spiderweb honeycombs exhibit auxetic behavior depending on the non-dimensional geometrical ratio of spiderweb.

2.2 Introduction

The spider's web is a highly efficient network of natural fibers where the geometry plays a major role in unique properties such as significant strength, toughness and reversible extensibility. From the structural point of view, the current state of literature on the spiderweb includes evaluation of the elastic properties of spider silk [79-86] and the out-of-plane mechanical properties of the structure under various static, dynamic, and impact loadings produced by wind, insects, or other natural sources [87-89]. In this dissertation we incorporate the spiderweb structural organization into hexagonal honeycombs resulting in a centrosymmetrical fractal-like pattern.

Recently, it has been shown that engineered self-similarity can be exploited to control the mechanical properties of cellular structures [53, 54, 60, 90-97]. Haghpanah et al. [71] carried out a comprehensive study of hierarchical design which considered multiple parameter enhancements of high order hierarchical honeycomb lattices and showed that remarkably favorable combinations of specific stiffness and specific strengths can be simultaneously achieved via hierarchical organization. However, unlike previously introduced geometries, the current topology has the advantage of controlling the response through a critical transition between two main structural responses in a cellular solid, namely the stretching and bending dominated behaviors. The transverse (i.e. in-plane) elastic modulus of a regular hexagonal honeycomb is governed mostly by the bending deformation of cell walls and is related to the structure's relative density through the closed-form expression: $E/E_s = 1.5\rho^3$, where E and E_s are respectively the Young's moduli of the structure and cell wall material, and ρ is the relative density of the structure [98]. On the other hand, in an equilateral triangular honeycomb, the elastic deformation is dominated by the axial extension or compression of cell walls, so that the resulting elastic modulus is much higher than the regular hexagonal honeycomb and is given as: $E/E_s = (1/3)\rho$ [98].

To this end, we introduce spiderweb hierarchy by adding smaller hexagons at the centers of cells in an underlying hexagonal network and connecting the adjacent vertices by straight beams. This procedure can be repeated at smaller scales to produce higher orders of spiderweb structure, yet the thickness of the cell walls is reduced simultaneously

to conserve the overall relative density of the structure. The resulting structural organization has an isotropic in-plane linear elastic response due to the preservation of six-fold symmetry. **Figure 2.1** shows the evolution of a regular hexagonal honeycomb cell as the order of hierarchy is increased through the introduction of successive spiderweb topology. The structural organization of the spiderweb honeycomb at each order of hierarchy can be defined by the ratio of the newly added hexagonal edge length (b for first order and c for second order spiderwebs), to the original hexagonal edge length, a, as illustrated in **Figure 2.1** (i.e., $\gamma_1 = b/a$ and $\gamma_2 = c/a$). For first order spiderweb honeycomb, $0 \leq b \leq a$ and thus, $0 \leq \gamma_1 \leq 1$, where $\gamma_1 = 0$ represents the equilateral triangular grid and $\gamma_1 = 1$ denotes the regular hexagonal honeycomb structure where each cell wall consists of three separate cell walls with a thickness equal to one third of the overall wall thickness. For a second order spiderweb honeycomb, $0 \leq c \leq b$ and thus, $0 \leq \gamma_2 \leq \gamma_1$. The relative density (equal to area fraction) can be given as:

$$\rho = 6/\sqrt{3}\ .(t/a) \qquad n = 0, 1$$

$$\rho = 2/\sqrt{3}\ .(t/a)\ .\left(3 + 2\sum_{i=1}^{n-1}\gamma_i\right) \qquad n \geq 2 \tag{2.1}$$

where t is the thickness of the cell walls and n is the order of hierarchy. Using this equation, one can easily obtain the wall thickness for a structure with specified geometry and relative density. For instance, for a second order hierarchical structure with $\gamma_1 = 1/6$, $\gamma_2 = (1/6)^2$, and 5% relative density, assuming the original edge length to be equal to unity, **Equation (2.1)** gives: $0.05 = 2/\sqrt{3} * (t/1) * (3 + 2 * (1/6))$, and then the thickness is obtained as $t = 0.01299$.

Analytical models based on energy methods were provided in **Section 2.3** to determine the closed-form expressions of small deformation Young's modulus and Poisson's ratio of first order spiderweb honeycombs. The analytical results were then compared with FE simulations. We provided numerical results for small deformation Young's modulus of second and higher orders of spiderweb hierarchy in **Section 2.4**.

Furthermore, large deformation elastic response of first order spiderweb honeycomb was investigated in **Section 2.5**. Conclusions were drawn in **Section 2.6**.

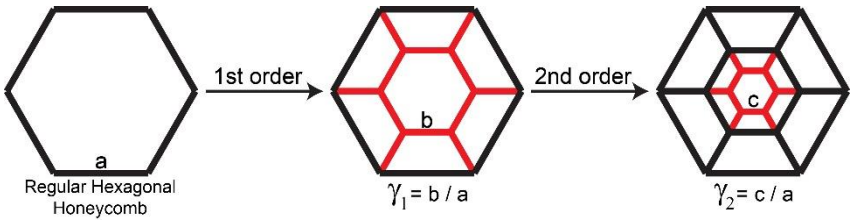

Figure 2.1 Schematics showing the evolution of the unit cell in a regular hexagonal honeycomb into first and second order spiderweb honeycombs.

2.3 First order spiderweb honeycombs under small deformations

2.3.1 Theoretical investigations

In this section, an analytical approach based on energy methods [72] is used to determine closed-form expressions for small deformation in-plane elastic moduli (Young's modulus and Poisson's ratio) of the first order spiderweb honeycomb. The cell walls of the structure were assumed to have an isotropic linear elastic behavior with the Young's modulus, E_s. A six-fold symmetry seen within the structure makes it exhibit macroscopic isotropy in the in-plane elastic behavior [73]. Therefore, for complete characterization of the in-plane elastic behavior of first order spiderweb honeycomb, we only need to determine two elastic constants. These constants can be obtained by employing any type of in-plane loading. Here without loss of generality, we chose biaxial loading in the principal directions of the material, *x* and *y* in **Figure 2.2**, to obtain the Young's modulus and Poisson's ratio.

To find the Young's modulus of a first order spiderweb honeycomb described earlier, we first imposed a far field biaxial state of stress (σ_{xx} and σ_{yy} in the *x*- and *y*-directions, respectively) as illustrated in **Figure 2.2 (A)**. Next, we choose the triangular area shown by dashed lines in **Figure 2.2 (A)** as a structural unit cell of the structure. This implies that we can restore the entire structure solely by translating and/or reflecting this triangle. Considering small deformations, we can assume that the deformation is symmetrical due to inherent geometrical symmetries of the structure as well as the symmetry of the applied macroscopic stresses (i.e., σ_{xx} and σ_{yy}). Therefore, the chosen

unit cell can only be utilized for this part of the study and cannot be employed for large and unsymmetrical deformation analysis. A free body diagram (FBD) of the unit cell is shown in detail in **Figure 2.2 (B)**. We assigned numbers (1 through 5) to the mid-points of the edges in the unit cell cut by the dashed lines, L_1-L_3. The horizontal edge in the unit cell with length $a/2 + (a - b)$ (see **Figure 2.2 (B)**) is an axis of symmetry for the unit cell. Thus, any pair of mirror points with respect to this edge experiences the same internal forces and moments, so same numbers were assigned to them. Consider the edges cut at their mid-points 1 and 3. Due to the 180^o rotational symmetry of the structure and the components of macroscopic stresses, no bending moment is transmitted by these edges at their mid-points. For example, if the bar at point 1 bulges 'downward', rotating the structure in the *x*-*y* plane by 180^o makes point 1 to bulge 'upward' breaking the symmetry of the structure and loading mentioned earlier. Next, considering the mid-points 1 and 2 and their corresponding edges, we can conclude that no vertical forces are transmitted by these edges through their mid-points, because that would again break the requirements of symmetry. For example, if the bar at point 1 transmits a 'downward' vertical force, reflecting the structure with respect to the *x* axis makes the vertical force to point 'upward'. Finally, symmetry of the structure also implies that points 4 and 5 transmit same forces and moments as shown in the figure. This is because point 5 can be mapped onto point 4 through a half plane rotation of the structure and loading around the intersection of lines L_1 and L_2 in **Figure 2.2 (A)**, followed by a rigid body translation along the line L_2 (in the down right direction by the magnitude $a\sqrt{3} + b\sqrt{3}/2$).

The unknown forces and moments being transmitted through the points 1-5 are summarized in **Figure 2.2 (B)**. They include four unknown horizontal forces, F_{x1} - F_{x4}, two unknown vertical forces, F_{y3} and F_{y4}, and two unknown moments, M and M', thus representing eight unknown variables, which would be uniquely determined through eight appropriate equations.

Note that based on the FBD of the unit cell (see **Figure 2.2 (B)**), two out of three equations of equilibrium in the *x*-*y* plane, i.e. $\Sigma F_y = 0$ and $\Sigma M = 0$, are automatically satisfied. Thus, we only need to take into account the *x*-component of equilibrium equation; i.e., $\Sigma F_x = 0$. This gives us, $F_{x1} = -(2F_{x2} + 2F_{x3} + 4F_{x4})$. Then, neglecting the

contribution of shearing energy, the strain energy stored in the unit cell can be written as a function of unknown forces and moments as, $U = U\left(F_{x2}, F_{x3}, F_{x4}, F_{y3}, F_{y4}, M, M'\right)$, in which the equations of equilibrium are already satisfied. Next, considering the cut line L_1, the average force per unit length transmitted through this vertical line is σ_{xx}, or in other words we can write the following relation between σ_{xx} and the forces acting on L_1:

$$\sigma_{xx} = \frac{F_{x1} + 2F_{x2}}{a\sqrt{3}} \tag{2.2}$$

Similarly, σ_{yy} is related to F_{y3} and F_{y4} through the following relation:

$$\sigma_{yy} = \frac{-\left(F_{y3} + 2F_{y4}\right)}{3a/2} \tag{2.3}$$

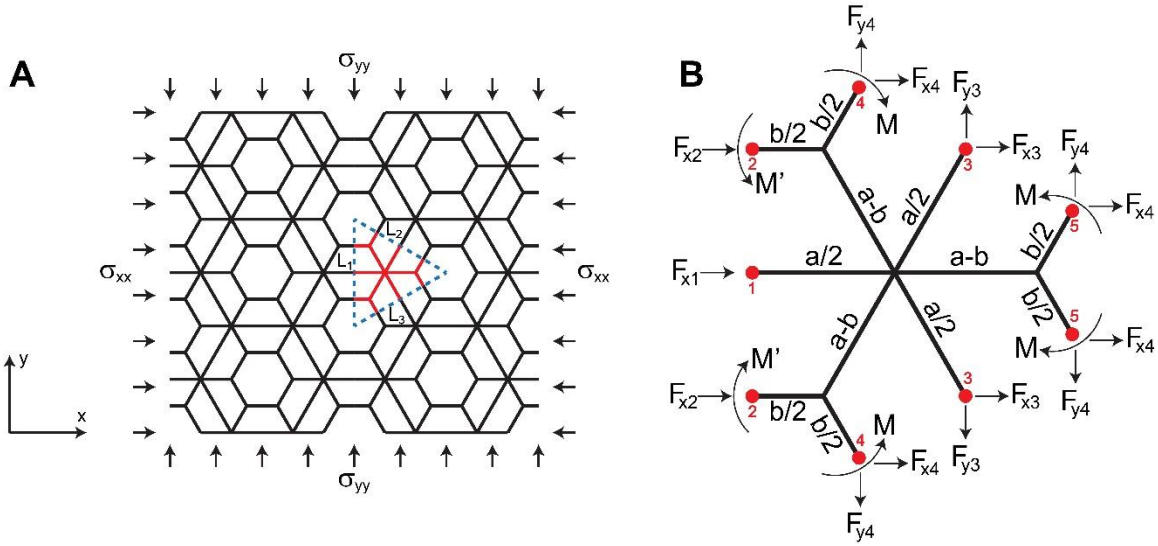

Figure 2.2 (A) First order spiderweb honeycomb under biaxial loading in x and y directions. A unit cell of the structure is shown by red. The area bounded by dotted lines is the effective area of the unit cell used in strain energy calculations. **(B)** Free body diagram of the unit cell.

Line L_1 is an axis of symmetry for the structure. So, the unit cell's three horizontal lines which are cut in half by L_1 through their mid-points 1 and 2 must deform in a fashion in which their right and left halves are mirror images with respect to line L_1. This implies that by fixing the coordinate system at the center of the unit cell, point 2 must have zero

displacement in the *x* direction and zero rotation with respect to the *z* axis. These constraints can be expressed mathematically using Castigliano's theorem [72] as:

$$\frac{\partial U}{\partial F_{x2}} = 0 \quad and \quad \frac{\partial U}{\partial M'} = 0 \tag{2.4}$$

Again, symmetries seen within the structure impose identical rotations of points 4 and 5. Since the direction of moment acting at point 4 is opposite to the direction of moment acting on point 5, the total amount of rotation of these two points in the direction of their moments must be equal to zero. Using Castigliano's theorem, this can be written as:

$$\frac{\partial U}{\partial M} = 0 \tag{2.5}$$

To be able to reconstruct the structure using deformed unit cells, points 3, 4, and 5, which are initially collinear must remain so during deformation. It can be shown that this constraint will be satisfied if the vector relation $\overrightarrow{u_3} = (\overrightarrow{u_4} + \overrightarrow{u_5})/2$ is satisfied, where $\overrightarrow{u_i}$ is the displacement vector of point i and $i = 3{,}4{,}5$. This equation actually includes two separate equations, i.e. one in the *x* and the other in the *y* directions as $u_{x3} = (u_{x4} + u_{x5})/2$, and $u_{y3} = \left(u_{y4} + u_{y5}\right)/2$, where u_{xi} and u_{yi} are respectively the displacements of point i ($i = 3{,}4{,}5$) in the *x* and *y* directions. Using Castigliano's theorem, these relations can be expressed as:

$$\frac{\partial U}{\partial F_{x4}} = 2\frac{\partial U}{\partial F_{x3}}$$

$$\frac{\partial U}{\partial F_{y4}} = 2\frac{\partial U}{\partial F_{y3}} \tag{2.6}$$

Equations (2.2)-(2.6), make a system of seven equations with seven unknowns. We employed Matlab® (Mathworks Inc., Natick, MA) to solve this system of equations using symbolic variables.

Note that under a uniaxial state of stress (i.e., $\sigma_{xx} \neq 0$ and $\sigma_{yy} = 0$), the Young's modulus of the structure is defined as $E = {\sigma_{xx}}^2/(2U_0)$, where U_0 is the strain energy density stored in the unit cell of the structure and is given as $U_0 = U/\left(3\sqrt{3}a^2/4\right)$. Then,

closed-form relation for the Young's modulus (to be normalized by the Young's modulus of cell wall material) is obtained as follows:

$$\frac{E}{E_s} = 4\sqrt{3}\delta^3 \frac{f_1(\gamma) + f_2(\gamma)\delta^2 + f_3(\gamma)\delta^4}{g_1(\gamma) + g_2(\gamma)\delta^2 + g_3(\gamma)\delta^4 + g_4(\gamma)\delta^6} \tag{2.7}$$

where $\delta = t/a$, $\gamma = \gamma_1$, and the functions appearing in the equation are listed below:

$$f_1(\gamma) = 6 - 16\gamma + 12\gamma^2 + 6\gamma^3 - 22\gamma^4 + 24\gamma^5 - 12\gamma^6 + 2\gamma^7$$

$$f_2(\gamma) = 12 - 23\gamma + 24\gamma^2 - 13\gamma^4 + 4\gamma^5$$

$$f_3(\gamma) = 6 - 7\gamma - \gamma^2 + 2\gamma^3$$

$$g_1(\gamma) = 18\gamma^3 - 60\gamma^4 + 72\gamma^5 - 36\gamma^6 + 6\gamma^7$$

$$g_2(\gamma) = 36 - 111\gamma + 88\gamma^2 + 78\gamma^3 - 169\gamma^4 + 132\gamma^5 - 60\gamma^6 + 10\gamma^7$$

$$g_3(\gamma) = 48 - 100\gamma + 97\gamma^2 + 6\gamma^3 - 59\gamma^4 + 20\gamma^5$$

$$g_4(\gamma) = 12 - 5\gamma - 17\gamma^2 + 10\gamma^3 \tag{2.8}$$

For the special case where $\gamma = 0$ (and $\delta \ll 1$), **Equation (2.7)** reduces to $E/E_s = \left(2/\sqrt{3}\right)\delta$, which is equivalent to the relative Young's modulus of an equilateral triangular honeycomb reported in the literature [98]. Interestingly, for the other special case where $\gamma = 1$ (and $\delta \ll 1$), **Equation (2.7)** reduces to $E/E_s = 4\sqrt{3}\delta^3$, which is three times the relative Young's modulus of a regular hexagonal honeycomb with thickness, t and edge length, a. This is because when $\gamma = 1$, the structure geometrically transforms to a regular hexagonal honeycomb with each cell wall consisting of three separate cell walls with thickness, t, and three-fold bending rigidity.

As mentioned earlier, to completely identify the linear elastic behavior of first order spiderweb honeycomb, we need to determine the Poisson's ratio of the structure, ν. We again use energy methods and consider the same structure as in **Figure 2.2** under biaxial state of stress. It should be emphasized that we ignored the contribution of beam shear deformation in strain energy density of the structure; however the bending and stretching terms are fully considered.

Under equi-biaxial state of stress (i.e. $\sigma_{xx} = \sigma_{yy} = \sigma$), the relation $\nu = 1 - U_0 E/\sigma^2$ can be used to obtain the Poisson's ratio of the structure [72], where again U_0 is the strain energy density of the unit cell and E is the Young's modulus of the structure that was determined earlier (**Equation (2.7)**). Therefore, closed-form relation for the Poisson's ratio of a first order spiderweb honeycomb can be derived as:

$$\nu = 1 - 4\delta^2 \frac{f_1(\gamma) + f_2(\gamma)\delta^2 + f_3(\gamma)\delta^4}{g_1(\gamma) + g_2(\gamma)\delta^2 + g_3(\gamma)\delta^4 + g_4(\gamma)\delta^6} \tag{2.9}$$

We now rewrite the above equation as a function of the Young's modulus of the structure as (see **Equation (2.7)**):

$$\nu = 1 - \frac{E/E_s}{\delta\sqrt{3}} \tag{2.10}$$

Note that for two special cases where $\gamma = 0$ and $\gamma = 1$ (in both cases take $\delta \ll 1$), **Equation (2.9)** reduces to $\nu = 1/3$ and $\nu = 1$ which are the Poisson's ratio of equilateral triangular and hexagonal honeycombs, respectively.

2.3.2 Numerical investigations

In this section, the finite element (FE) method was used to verify the analytical formulations of elastic response of first order spiderweb honeycombs derived in the previous subsection of this dissertation. Commercially available FE software ABAQUS 6.11-2 (SIMULIA, Providence, RI) was used to carry out all the simulations in this study. 3D models of first order spiderweb honeycomb structure were meshed using 4-node shell elements (S4R). A mesh sensitivity analysis was also performed to ensure that the results are not dependent on the mesh size. Cell walls were assumed to have a rectangular cross section with unit length normal to the plane of loading (i.e., normal to the *x-y* plane (see **Figure 2.2**)) and the thickness was adjusted to be consistent with the value of the relative density. Linear elastic properties of aluminum were assumed for the cell wall material with $E_s = 70GPa$, and $\nu_s = 0.3$.

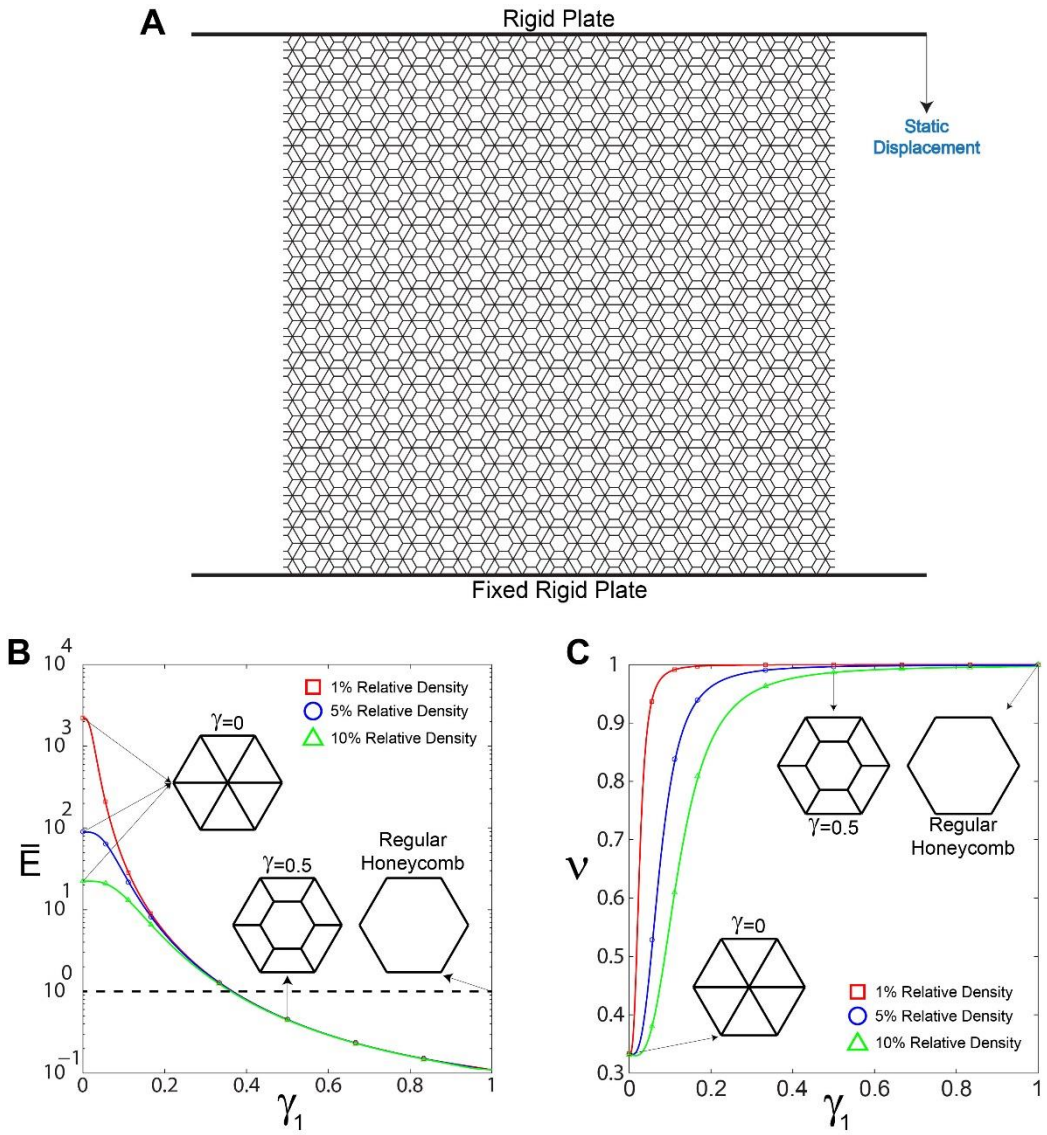

Figure 2.3 (A) Schematic of the finite element model of first order spiderweb honeycomb under in-plane compressive loading. **(B)** Normalized Young's modulus, and **(C)** Poisson's ratio, versus γ_1 for honeycombs with three different relative densities (solid lines show the analytical estimates, markers show the finite element results).

Figure 2.3 (A) shows the schematic diagram of the FE model constructed in ABAQUS for simulating static uniaxial loading on first order spiderweb honeycomb. Vertical displacement of the top and bottom nodes of the structure was coupled to the corresponding rigid flat plates. A constant downward static displacement was then assigned to the top plate, while the bottom plate was fixed. To eliminate any boundary effects,

periodic boundary conditions were imposed to the structure on the right and left side nodes [77]. Also note that the horizontal displacement of an arbitrary node in the structure was constrained (i.e., set to zero) in order to prevent rigid body motion of the structure in that direction. The out-of-plane degrees of freedom of the model were also constrained to avoid the out-of-plane buckling of the structure.

Figures 2.3 (B) and **2.3 (C)** respectively show the normalized Young's modulus, $\bar{E}$ and Poisson's ratio, ν of first order spiderweb honeycombs for all possible values of γ_1. The Young's modulus is normalized by the Young's modulus of a regular hexagonal honeycomb with same relative density, $E = 1.5E_s\rho^3$. The results are presented for three different values of relative densities, 1%, 5%, and 10%. In the figures, solid lines represent the results obtained directly by using the theoretical closed-form expressions derived in the previous subsection of this dissertation, and markers denote the FE results. Excellent agreement between the analytical and numerical approaches was observed even though the contribution of shearing energy was neglected in the analytical method presented in the previous subsection. For the values of γ_1 greater than $\gamma_1 \cong 0.25$, the structure exhibits a bending dominated behavior (i.e., $E/E_s \propto \rho^3$), with the normalized Young's modulus independent of the relative density $\bar{E} \propto \rho^0$. In contrast, for the values of γ_1 smaller than $\gamma_1 \cong 0.25$, the honeycomb transforms into a stretching dominated structure with $E/E_s \propto \rho$ or equally $\bar{E} \propto \rho^{-2}$. At $\gamma_1 = 0$, the normalized Young's modulus is obtained as 2222, 89, and 22 for the relative densities of 1%, 5%, and 10%, respectively. As the value of γ_1 increases, since the structure transforms from stretching to bending dominated one, its normalized Young's modulus decreases. At $\gamma_1 \cong 0.35$ the stiffness of the structure is about the stiffness of a regular hexagonal honeycomb with same relative density. After this point, the structure becomes more compliant compared to a regular honeycomb. At the $\gamma_1 = 1$ limit, the structure transforms into a regular hexagonal honeycomb with each cell wall consisting of three separate cell walls. At this point the normalized Young's modulus can be obtained using **Equation (2.7)** as, $4\sqrt{3}\left(\rho\sqrt{3}/6\right)^3/(1.5\rho^3) = 1/9$. **Figure 2.3 (C)** shows the Poisson's ratio of first order spiderweb honeycomb varying from $1/3$ (equilateral triangular lattice) to 1 (regular hexagonal honeycomb). With decrease in the relative density, the Poisson's ratio for a constant value of γ_1 ($\gamma_1 \neq 0$) approaches unity.

2.4 Higher order spiderweb honeycombs under small deformations – Young's modulus

FE analysis was used to evaluate the small deformation elastic response in higher order spiderweb honeycombs. Finite size, 3D models of the structure were constructed in ABAQUS, and were subjected to uniaxial static compression along y-direction. Material properties, FE models, boundary conditions, and loadings are similar to those explained in **Section 2.3**. The overall relative density of the structures was fixed at 5%.

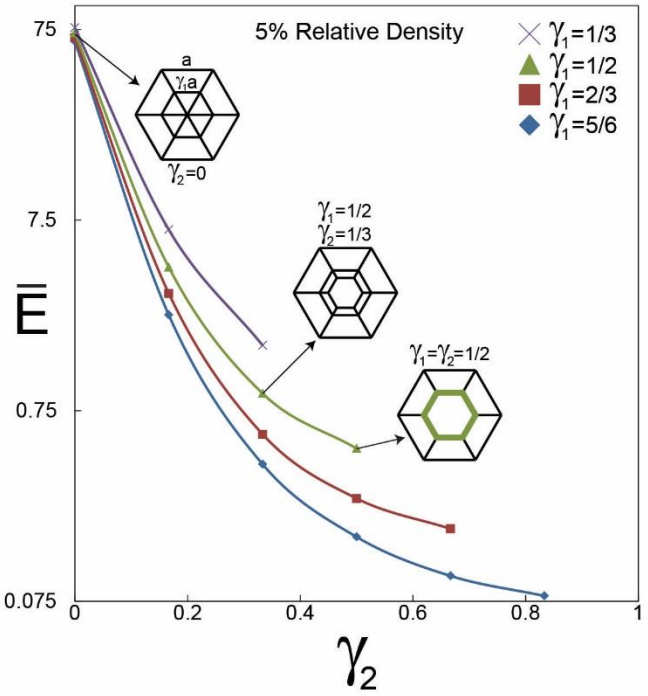

Figure 2.4 Normalized Young's modulus versus γ_2 for second order spiderweb honeycombs with different values of γ_1. The relative density of honeycombs was kept constant as 5%.

Figure 2.4 shows the FE results on the Young's modulus of second order spiderweb honeycombs normalized by that of a regular hexagonal honeycomb of equal relative density ($E = 1.5E_s\rho^3$), versus γ_2. The results are plotted for four different values of γ_1= 1/3, 1/2, 2/3, 5/6. Geometrically, the structural parameter γ_2 is bound on the upper limit by the value of γ_1, i.e., $\gamma_2 \leq \gamma_1$. Similar to the first order spiderweb honeycombs, lower values of γ_1 result in higher Young's modulus at a constant value of γ_2. At a constant value of γ_1,

increasing the value of γ_2 decreases the Young's modulus of the structure since the bending compliance of the structure is increased and less portion of the strain energy is stored through the axial stretching of the beams.

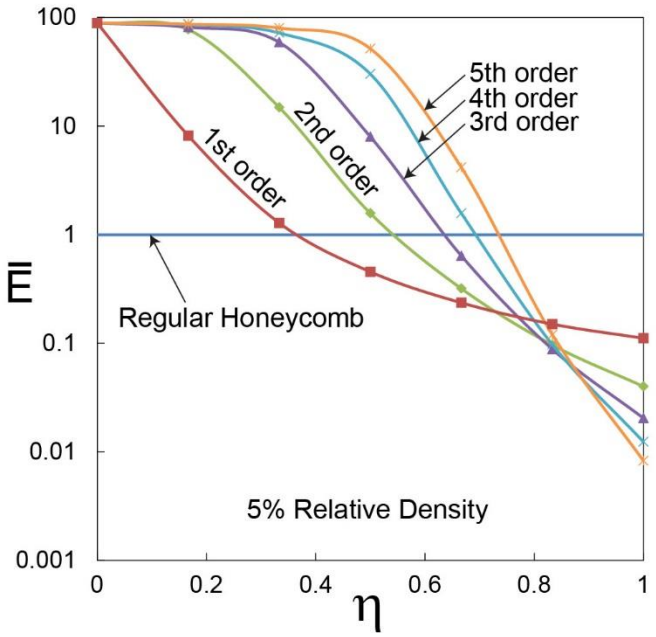

Figure 2.5 Normalized Young's modulus versus η for higher order spiderweb honeycombs (up to fifth order). The relative density of honeycombs was kept constant as 5%.

To investigate the Young's modulus of higher order spiderweb honeycombs, we introduced a scalar geometrical ratio, η, defined as $\gamma_i = \eta^i$ (e.g., $\gamma_1 = 1/6$ and $\gamma_2 = 1/36$ for a second order spiderweb honeycomb with $\eta = 1/6$). This relation in fact describes a subclass of fractal-like spiderweb honeycomb with constant ratios between successive hexagonal sides. The normalized Young's modulus of higher order spiderweb honeycombs (up to fifth order) with different values of η is plotted in **Figure 2.5**. The Young's modulus of the structures is normalized by the Young's modulus of a regular hexagonal honeycomb of equal relative density ($E = 1.5E_s\rho^3$). For honeycombs with $\eta < \sim 0.8$, increasing the hierarchical order increases the Young's modulus of the structure. However, for $\eta > \sim 0.8$ a negative correlation is found between the hierarchical order and Young's modulus. In fact, the mechanical response in spiderweb honeycombs is governed by the size of the smallest hexagonal feature (i.e., η^n for nth order of hierarchy). Therefore, based on the

results obtained for first order hierarchy (i.e., $\gamma_1 = 0.25$ as the boundary between stretching and bending dominated behaviors), as well as the results shown in **Figure 2.5** for higher order structures, we can define an empirical equation to estimate the boundary between stretching and bending dominated behaviors of self-similar spiderweb honeycombs as $\eta^n = 0.25$. This empirical condition states that the transition from stretching to bending dominated behaviors occurs at increasing η value as the order of hierarchy increases. For instance, $\eta = 0.25$ and $\eta \sim 0.76$, respectively for first and fifth orders of hierarchy. In general, in a fully stretching dominated regime (lower values of η), a smaller hexagon will result in a more stretching dominated structure and increased Young's modulus. However, in the fully bending dominated regime (higher values of η), the increase in Young's modulus due to higher stretching energy is somewhat offset by the fact that an addition to the order of hierarchy will only reduce the effective bending rigidity of the cell walls (beams) due to conservation of mass, resulting in a decreased Young's modulus.

2.5 First order spiderweb honeycombs under large deformations

In this section, we investigated the large deformation elastic response of first order spiderweb honeycombs under quasi-static compressive loading. Material properties, FE models, boundary conditions, and loadings are similar to those discussed in the previous sections, and similar to the previous section the overall relative density of the structure was kept constant at 5%. Similar to previous sections, a mesh sensitivity analysis was also performed to ensure that the results are not dependent on the mesh size. The deformation of first order spiderweb honeycomb with different values of γ_1 was simulated up to at least 40% crushing strain.

It is well known [10] that typical cellular solids have a distinctive sequence of practically linear elastic behavior, weakly stable or unstable collapse due to instability or plasticity, followed by a significant restiffening caused by densification. The latter regime occurs at 70% - 80% strain for low density cellular structures. The compressive stress-strain response of spiderweb honeycomb obtained for different values of γ_1 is plotted in

Figure 2.6 (A). For $\gamma_1 = 0$ (equilateral triangular honeycomb), the "stress plateau" regime begins at the very early stages of crushing (strain ~ 0.1%) as the result of elastic buckling (i.e., instability) of the cell walls. This very low buckling strain is due to the highly stretching-dominated behavior of the structure [99]. As the value of γ_1 increases, although the small deformation Young's modulus of the structure decreases dramatically, instability occurs at higher strains. For example, for $\gamma_1 = 1/4$ the instability occurs at 8% crushing strain. This effect would cause the structures with γ_1 equal or greater than 1/3 to not experience instability until 40% crushing strain. In fact, the large static deformation along with large lateral load components in the cell walls would entirely suppress instability in these structures [99]. At $\gamma_1 = 1/3$, although the small deformation stiffness is much lower than that of the triangular honeycomb, the structure is much stronger in crushing strains greater than 7.5%.

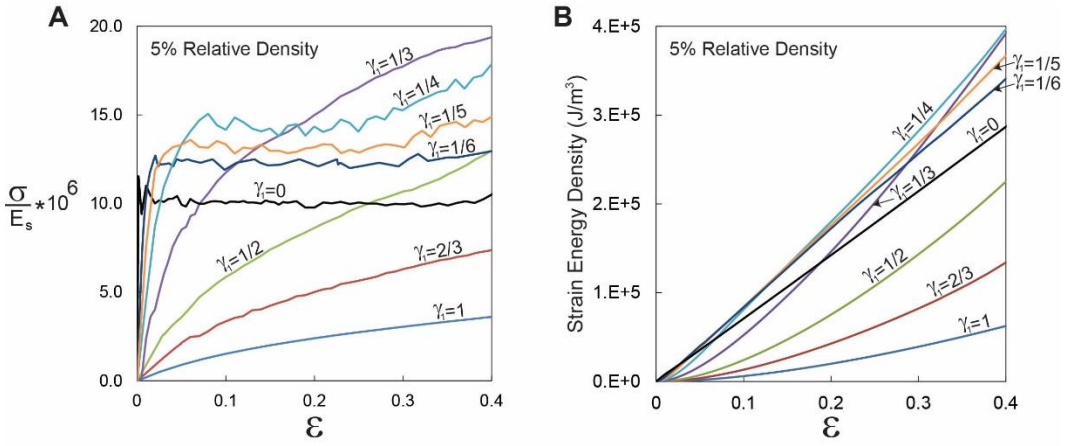

Figure 2.6 Nonlinear elastic response of first order spiderweb honeycombs under large deformations. **(A)** Normalized stress (with respect to the Young's modulus of cell wall material), and **(B)** Strain energy density of the honeycombs versus crushing strain plotted for first order spiderweb honeycombs with different values of γ_1. The relative density of honeycombs was kept constant as 5%.

The load-displacement response of the spiderweb honeycombs promises potentially enhanced values of toughness and energy absorption at certain geometries, which we will investigate next. **Figure 2.6 (B)** shows plots of the strain energy density versus crushing strain. Note that the strain energy density shown in this figure is equivalent to the area of the region bounded by the graph of stress and x-axis in **Figure 2.6 (A)**. Smaller values of

γ_1 correspond to the higher elastic energy storage in the structure at small deformation range (ε < 2.5%). For $\gamma_1 \leq 1/3$, this behavior is reversed as deformation proceeds to larger strains. For example at 40% crushing strain, the elastic energy storage capacity of spiderweb honeycombs with $\gamma_1 = 1/4$ and $\gamma_1 = 1/3$ is equally about 40% greater than that of a triangular honeycomb ($\gamma_1 = 0$). The noticeable difference between energy storage performance for structures $\gamma_1 = 1/3$ and $\gamma_1 = 1/4$ is due to cell wall buckling in the latter structure starting at ε = 8%. At 40% strain, the spiderweb structure with $\gamma_1 = 1/3$ has not experienced instability, yet it has the greatest strain energy density among all the values of γ_1 studied (equal to $\gamma_1 = 1/4$).

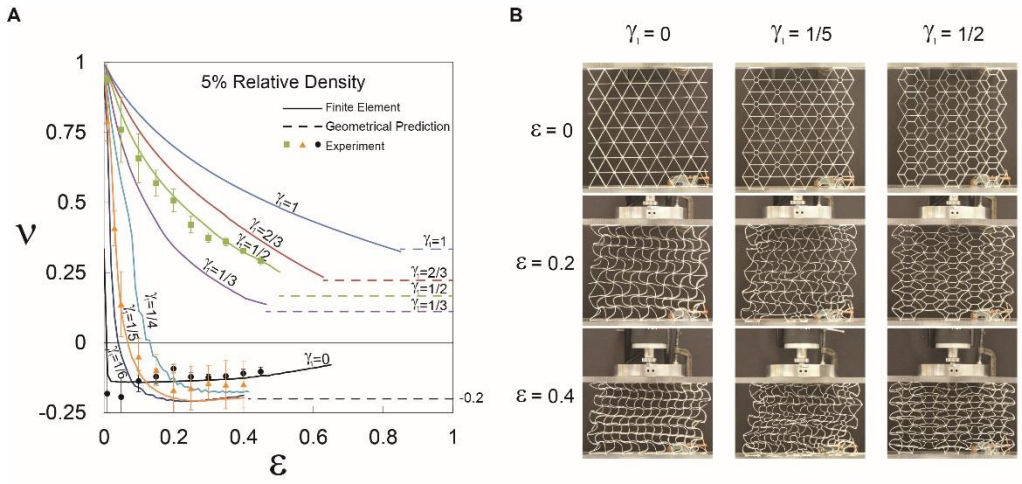

Figure 2.7 (A) Poisson's ratio versus crushing strain for first order spiderweb honeycombs under large deformations. The solid lines show the finite element results and dashed lines denote the geometrical predictions at 100% crushing strain for honeycombs with different values of γ_1. The markers show the experimental results for $\gamma_1 = 0$, $\gamma_1 = 1/5$, and $\gamma_1 = 1/2$. **(B)** Undeformed ($\varepsilon = 0$) and deformed configurations of specimens at two different crushing strains, $\varepsilon = 0.2$ and $\varepsilon = 0.4$. The specimen with $\gamma_1 = 0$ has an overall size of 245 mm * 243 mm with wall thickness of 0.5 mm and wall length of 35 mm. The specimens with $\gamma_1 = 1/5$ and $1/2$ have an overall size of 225 mm * 243 mm with wall thickness of 0.4 mm and wall length of 28 mm. All specimens maintain a relative density of 5%.

As previously observed, occurrence of instability could significantly influence the deformation mechanisms and large deformation elastic response of first order spiderweb honeycombs. For further studying this effect, the effect of large deformation elasticity on Poisson's ratio is studied next. In **Figure 2.7 (A)**, Poisson's ratio is plotted against the

crushing strain. The solid lines denote the FE results and the dashed lines represent the Poisson's ratio estimations at 100% crushing strain obtained by a geometrical estimation which will be discussed shortly in this section. The markers show the experimental data for $\gamma_1 = 0$, $\gamma_1 = 1/5$, and $\gamma_1 = 1/2$, which are in good agreement with numerical results. For the experimental investigations, the specimens were fabricated using PolyJet 3D printing (Objet24 3D printer, Stratasys Inc., Eden Prairie, MN) with VeroWhitePlus© (see **Appendices** for material's stress-strain response). The specimen with $\gamma_1 = 0$ has an overall size of 245 mm * 243 mm with wall thickness of 0.5 mm and wall length of 35 mm. The specimens with $\gamma_1 = 1/5$ and $1/2$ have an overall size of 225 mm * 243 mm with wall thickness of 0.4 mm and wall length of 28 mm. All specimens maintain a relative density of 5%. The specimens were then tested under uniaxial compression using an Instron 5582 testing machine at the rate of 5 mm/min (i.e. strain rate of 2%/min). Images of deformed configurations were taken to obtain the values of Poisson's ratio in the section of the structure far from the boundaries. For each specimen the measurement were repeated 4 times. The figure shows that the value of Poisson's ratio for each structure at very small strains is equal to the value predicted by theoretical analysis presented in **Section 2.3.1**. As the crushing proceeds, Poisson's ratio decreases. The rate of reduction is higher for smaller values of γ_1. **Figure 2.7 (B)** shows the undeformed and deformed configurations of the experimental samples at two different stages, $\varepsilon = 0.2$ and $\varepsilon = 0.4$, where two different behaviors are observed which will be discussed shortly. For values of γ_1 greater than 1/3 the Poisson's ratio remains positive. On the other hand, an auxetic behavior (i.e. negative Poisson's ratio) is seen for the structures with γ_1 less than 1/3. $\gamma_1 = 1/4$ seems to be a threshold value of γ_1 in which the deformation mechanism of the structure completely changes. To understand the difference between these two behaviors, we studied deformation mechanism of the structures at 40% strain. Schematics of undeformed configuration for the unit cell of spiderweb structures with eight different values of γ_1 are shown in **Figure 2.8**. FE results on deformed configurations at 40% strain are also depicted in this figure. Two different types of deformation mechanism were seen within the structures. In mechanism #1, the structure deformation is mostly governed by static deflection in the cell walls. No instability (i.e., elastic buckling) is observed in the structures deforming based on this deformation mechanism, which is dominant in the

structures with $\gamma_1 > 1/3$. All nodal rotations are zero (or very close to zero approaching $\gamma_1 = 1/3$) due to the reflection symmetry of the structure and loading. The second mechanism takes place in the structures with $\gamma_1 < 1/3$ (i.e., stretching dominated) and is mostly governed by elastic buckling of cell walls and rotation of the smaller hexagons which remain almost intact. The limit structure is the case of $\gamma_1 = 0$, where the periodic deformation is characterized by the equal rotation of all nodes in a row, while adjacent rows have opposite rotations.

To estimate the Poisson's ratio at 100% crushing strain for the structures whose deformation is governed by deformation mechanism # 1, we considered an undeformed unit cell of the structure with the geometrical ratio $\gamma_1 = b/a$ as shown in **Figure 2.8**. The simplified geometry of deformed unit cell at 100% strain is also shown in the bottom of **Figure 2.8**. Using this, the transverse engineering strain (ε_x) is obtained as $\big((3a + \mathrm{b}) - (3a)\big)/(3a) = b/(3a)$, while the axial engineering strain (ε_y) is given as $\big(0 - a\sqrt{3}\big)/\big(a\sqrt{3}\big) = -1$. Thus, the Poisson's ratio can be estimated as $-(b/(3a))/(-1) = b/(3a) = \gamma_1/3$. Regarding the deformation mechanism # 2, an undeformed unit cell of the structure with the geometrical ratio $\gamma_1 = b/a$ is shown in **Figure 2.8**. Simplified deformed configuration is also shown in this figure. Based on FE observations at 100% crushing strain, the midpoints in beams oriented initially at 60° (or 120°, based on rotation direction) become in contact with midpoints of initially horizontal beams. Therefore, we considered that the smaller hexagon rotates 60° in the plane of loading at 100% crushing strain. It was also assumed that the deformation (u) in edges that are originally horizontal in the undeformed configuration will be a cubic function of the position (s) along the beam (i.e., $\partial^4 u/\partial s^4 = 0$), since there is no distributed load acting on the edges. Using these assumptions it can be shown that a horizontal edge with length L will bend such that its final length in horizontal direction will be $0.8L$ (see **Appendices**). So the transverse engineering strain (ε_x) is obtained as $\big((0.8(a-b)*2 + 0.8(a/2)*2 + b) - 3a\big)/(3a) = -0.2(1+\gamma_1)$. The axial engineering strain (ε_y) is again evaluated as -1. Thus the Poisson's ratio is estimated as $-\big(-0.2(1+\gamma_1)\big)/(-1) = -0.2(1+\gamma_1)$. Note that the value of γ_1 in this deformed configuration is smaller than 1/3, so we can estimate the Poisson's ratio to be -0.2 for all

the structures following this deformation mechanism. A very good agreement is observed between the FE results and the values estimated by geometrical predictions.

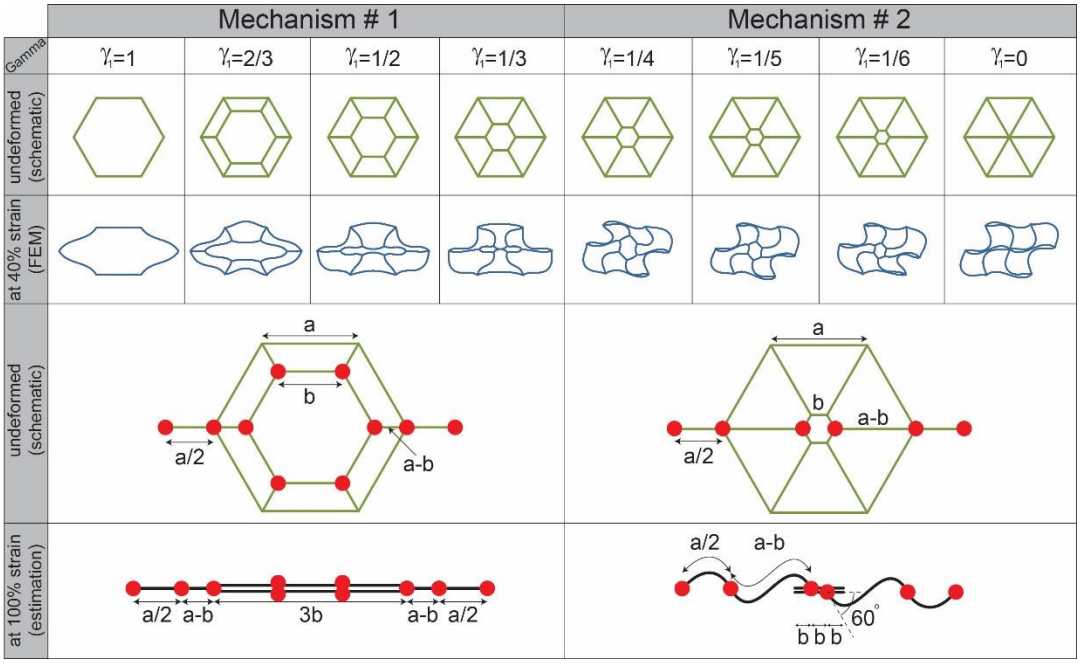

Figure 2.8 Nonlinear elastic response of first order spiderweb honeycombs under large deformations. Two different types of deformation mechanism are seen in the honeycombs under uniaxial compression. For each γ_1, the schematic of undeformed unit cell and finite element result of deformed unit cell at 40% crushing strain are shown (two top rows). For each deformed mechanism, the schematic of undeformed unit cell and predicted configuration of deformed unit cell at 100% crushing strain are also shown (two bottom rows).

2.6 Conclusions

The effect of spiderweb hierarchical organization on the in-plane elastic response of honeycombs in small and large deformation regimes was studied. Analytical closed-form formulas for the Young's modulus and Poisson's ratio for the first order spiderweb honeycomb were obtained and verified numerically. It was shown that a relatively broad range of linear elastic response, varying from bending to stretching dominated, can be achieved by tailoring the structural organization of spiderweb honeycombs. While the geometrical parameters influence the linear elastic moduli in small deformations, they also

significantly influence the mechanisms of deformation in large deformation regime. In structures with $\gamma_1 > 1/3$, large deformation is symmetrical and is formed by the static deflection in the cell walls. When $\gamma_1 < 1/3$ (i.e., stretching dominated structures), deformation is nonlinear, asymmetric and is accompanied by elastic buckling of cell walls and rotation of the nodes. The latter mechanism is not unique for a given macroscopic state of stress and is influenced by boundary conditions [99]. Furthermore, a geometrical estimation for the large deformation Poisson's ratio of spiderweb honeycombs at 100% crushing strain was presented. Large deformation auxetic behavior was observed in first order spiderweb honeycombs with γ_1 less than 1/3.

A unique feature in the spiderweb honeycomb is a combination of high stiffness and toughness. Toughness of the spiderweb honeycomb - a measure of structure's ability to absorb energy under quasi-static loading - is greater than that of a stretching dominated structure (e.g., triangular lattice). In a stretching dominated cellular solid under crushing, the capacity of the structure to absorb energy is limited by the early onset of buckling occurring at low crushing strains. A bending dominated structure, on the other hand, has a relatively low relative stiffness which makes it unsuitable for many in-plane applications. Spiderweb design can therefore provide required stiffness and toughness, as the geometrical parameters can be tuned to create a sweet spot between bending and stretching dominant responses. The elastic energy storage capacity of the spiderweb honeycombs with $\gamma_1 = 1/4$ and $\gamma_1 = 1/3$ was shown to be about 40% greater than triangular honeycomb ($\gamma_1 = 0$) at 40% crushing strain.

2.7 Appendices

2.A Material properties

For the experiments we used VeroWhitePlus© material with the stress-strain response shown in **Figure 2.A.1**.

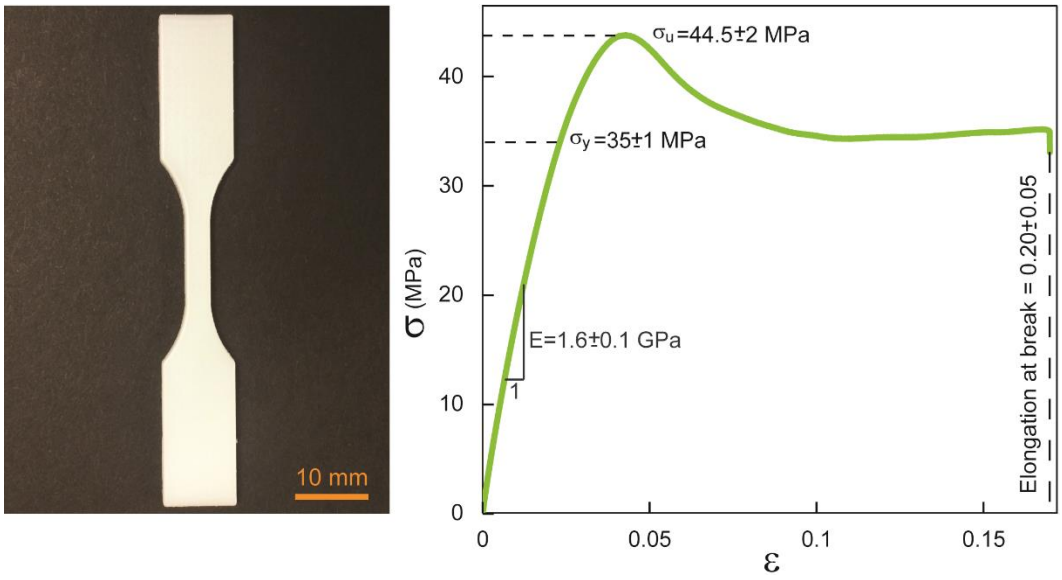

Figure 2.A.1 (left) 3D printed dog-bone specimen for uniaxial tension test. **(right)** engineering stress vs. engineering strain for the tested material.

Note that five dog-bone samples (**Figure 2.A.1 (left)**) were tested under uniaxial tensile loading to obtain the stress-strain response of the material (engineering stress vs. engineering strain). The tension tests were based on ASTM-D638-10 standard, which is the standard test method for tensile properties of plastics.

2.B Geometrical estimation

As shown in **Figure 2.B.1**, consider a horizontal line with length L under a loading in which it bends such that it forms a cubic function (i.e., $y = ax^3 + bx^2 + cx + d$ where x here denotes position along beam direction) with the slope of -60° at both ends. Also assume that the length of the curved line remains L and the horizontal distance between two ends is L'. The following geometrical boundary conditions can be written based on the assumptions:

$$y(0) = 0, \quad y''(0) = 0, \quad y(L'/2) = 0, \quad y'(L'/2) = -\sqrt{3} \tag{2.B.1}$$

where y' and y'' are respectively the first and second derivatives of y with respect to x. Solving **Equation (2.B.1)**, the unknown constants appearing in y are obtained as, $b = d =$

0, $a = -\frac{2\sqrt{3}}{L'^2}$, and $c = \frac{\sqrt{3}}{2}$. Using the assumption that the length of the curved line remains L we can finally obtain the unknown length L' by using the following relation:

$$2\int_0^{\frac{L'}{2}} \sqrt{1 + y'^2}\,dx = L \tag{2.B.2}$$

Solving this equation will result in $L' = 0.8L$.

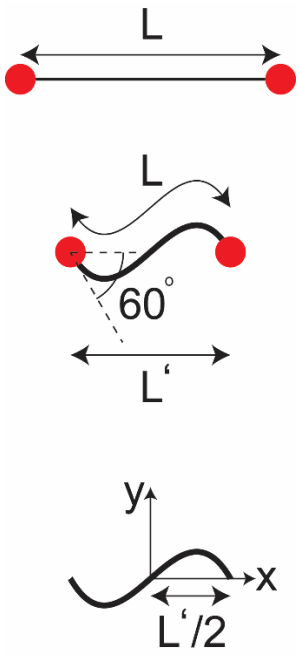

Figure 2.B.1 Undeformed and deformed line with original length L.

Chapter 3

Hierarchical Honeycomb Auxetic Metamaterials

3.1 Abstract

Most conventional materials expand in transverse directions when they are compressed uniaxially resulting in the familiar positive Poisson's ratio. Here we develop a new class of two dimensional (2D) metamaterials with negative Poisson's ratio that contract in transverse directions under uniaxial compressive loads leading to auxeticity. This is achieved through mechanical instabilities (i.e., buckling) introduced by structural hierarchy and retained over a wide range of applied compression. This unusual behavior is demonstrated experimentally and analyzed computationally. The work provides new insights into the role of structural organization and hierarchy in designing 2D auxetic metamaterials, and new opportunities for developing energy absorbing materials, tunable membrane filters, and acoustic dampeners.

3.2 Introduction

In recent years, synthetic metamaterials with negative Poisson's ratio (defined as the negative of the ratio between transverse and longitudinal strains in uniaxial elastic loading) have been proposed [100-105]. In contrast to conventional materials, these so-called "auxetic" metamaterials contract in the transverse directions when compressed uniaxially [106]. This behavior is usually linked to specific microstructural deformation mechanisms also observed in traditional auxetic structures such as re-entrant, chiral, and rotating-units structures [32, 107-114]. On the other hand, elastic instability (i.e., buckling) can also be utilized to induce auxetic behavior over a wide range of applied strains in the structures, which otherwise show positive Poisson's ratio at small deformations [115-117]. Particularly, in this context, the role of hierarchy has been recently explored by Mousanezhad et al. [115] who demonstrated auxetic behavior in a hierarchical "spiderweb" honeycomb at large deformations through a combination of numerical simulations and experiments.

Here, we exploit elastic instabilities along with structural hierarchy to design a new class of 2D auxetic metamaterials capable of exhibiting negative Poisson's ratio over a wide range of applied compressive strains. Our study shows that the origin of this behavior is linked to the added hexagonal features within the hierarchical structure which make the instabilities to occur at smaller compressive strains compared to the original non-hierarchical structure leading to auxeticity. In fact, these particular buckling modes have been previously observed in regular hexagonal honeycombs but they did not lead to auxeticity [61].

The hierarchical structure studied in this article which was first introduced by Ajdari et al. [76], exhibited higher stiffness and more phononic bandgaps compared to its regular non-hierarchical counterpart [54, 76, 118]. The structure exhibits a positive Poisson's ratio, ranging from ~0.37 to 1, at small deformations for first order of hierarchy [76]. The first level of hierarchy which was achieved by replacing the vertices of a regular hexagonal lattice with smaller hexagons and reducing the wall thickness to keep the overall density fixed, could be repeated to reach higher levels of hierarchy. **Figure 3.1** shows the evolution of a regular hexagonal honeycomb and its corresponding cell as the order of

hierarchy is increased. The geometrical organization of this structure at each order of hierarchy (γ_i) is defined by the ratio of the newly added hexagonal edge length (b for first order and c for second order of hierarchy, see **Figure 3.1**) to the original hexagon's edge length (a) (i.e., $\gamma_1 = b/a$, and $\gamma_2 = c/a$) [76] (See **Appendices** for more details). The density of the structure (i.e., area fraction) normalized by the parent material density can be given as [76]

$$\rho = 2/\sqrt{3}\,.(1 + 2\gamma_1 + 6\gamma_2)\,.t/a, \tag{3.1}$$

where t is the wall thickness which is assumed to be uniform throughout the structure.

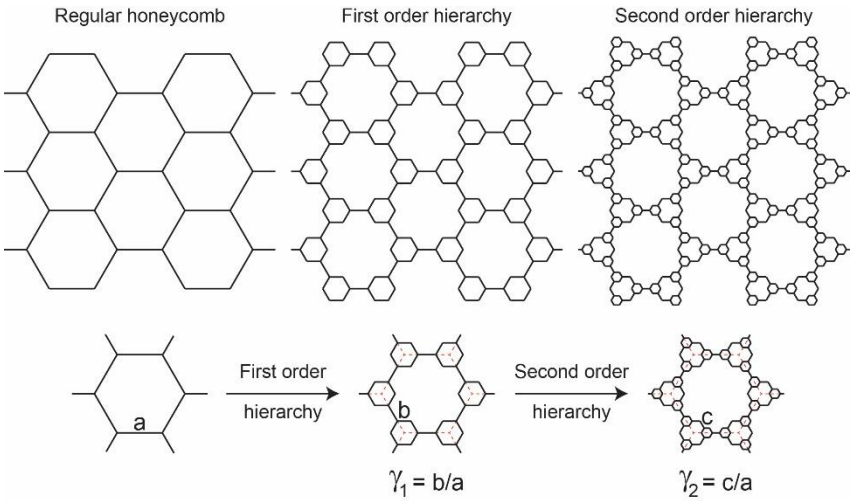

Figure 3.1 Schematic showing the evolution of a regular hexagonal honeycomb and its corresponding cell into first and second orders of hierarchy. The structural organization of the hierarchical structure at each order of hierarchy (γ_i) is defined as the ratio of the newly added hexagonal edge length (b for first order and c for second order of hierarchy) to the original hexagon's edge length (a) (i.e., $\gamma_1 = b/a$, and $\gamma_2 = c/a$) [76].

3.3 Results

We subjected a specimen with first order of hierarchy ($\gamma_1 = 0.25$) under uniaxial compression along the y and x directions (see **Section 3.5** and **Appendices** for more details), **Figure 3.2**. The response of the specimen was monitored by taking photographs at different levels of compression with local strains ε_{yy} and ε_{xx} in either direction measured within the inner-most unit of the specimen (i.e., Representative Volume Element

(RVE), highlighted in yellow in **Figure 3.2**) to avoid boundary effects [116, 119, 120]. Note that the classical definition of an RVE relies on a limit of relatively infinite size of the sample thereby making boundaries irrelevant. However, finite sample size is inevitable in experiments and in the current work we seek to minimize the boundary effects on the inner-most unit of the specimen by choosing sufficient numbers of unit cells in the test sample thereby making it equivalent to an RVE in an infinite periodic media. Thus, in this work, we compare the experimental response of only the inner-most unit cell, which has minimal boundary effects with our numerical simulations, which rely on the assumption of an infinite periodic sample (the details of numerical simulations will be explained shortly). **Figure 3.2** shows the undeformed and deformed configurations of the specimen and its RVE. As the deformation proceeds in either direction, the lateral sides of the specimen bulge inward, showing a perceptible 2D auxetic behavior which has not been observed in the non-hierarchical counterpart. Interestingly, two different types of deformation mode (i.e., buckling mode) are identified depending on the direction of the applied compression: X-shape and N-shape modes, respectively for the *y* and *x* direction loads. In the X-shape mode, the RVE's deformation is mostly governed by elastic buckling of the horizontal cell walls and rotation of the corresponding smaller hexagons in the central hexagonal cell, while the RVE's other horizontal cell walls and corresponding smaller hexagons remain almost intact. This is analogous to the buckling mode of a regular hexagonal honeycomb in biaxial compression [75, 99]. The N-shape deformation mode on the other hand, is characterized by a zigzag collapse of hexagonal cells due to compression along the *x* direction, similar to the uniaxial buckling mode of the regular hexagonal honeycomb [75, 99]. Interestingly, these buckling modes, which have been previously observed in the regular structure, did not lead to auxeticity.

In order to quantify this behavior, we plot the transverse strain and Poisson's ratio against the longitudinal strain for both loading directions, respectively in **Figures 3.3 (a)** and **3.3 (b)**, by post-processing photographs (See **Appendices** for details on strain calculations). Next, we computationally analyzed a single RVE under uniaxial compression along the y and x direction using finite element (FE) simulations, intrinsically assuming the structure to be infinitely extended in 2D space (i.e., periodic boundary conditions were imposed) [116]. We first investigated the instability of the structure

through a linear perturbation analysis [121]. Then, the non-linear post-buckling response of the system was simulated by introducing a small imperfection in the initial geometry (see **Section 3.5** for more details). In **Figures 3.3 (a)** and **3.3 (b)**, FE results of the transverse strain and Poisson's ratio (denoted by solid lines) are reported as functions of the longitudinal strain for both loading directions, which are in an excellent agreement with experimental results. Also, **Figure 3.3 (c)** compares the experimental and numerical images of deformed configurations of the RVE at different levels of applied compressive strain along the *y* (i.e., X-shape mode) and *x* (i.e., N-shape mode) directions, which are again in perfect agreement.

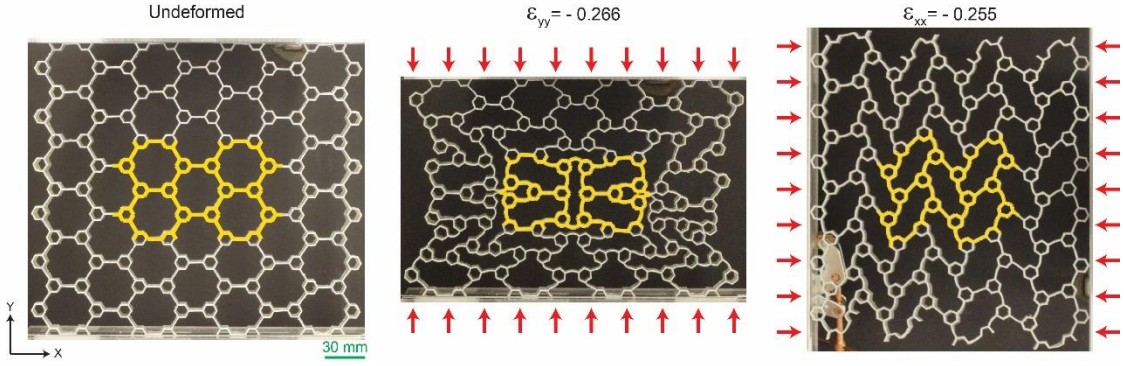

Figure 3.2 Hierarchical honeycomb auxetic metamaterials. (left) Undeformed configuration of the fabricated first order hierarchical structure with $\gamma_1 = 0.25$. The representative volume element (RVE) is highlighted as yellow. (middle and right) Deformed configurations of the specimen and the RVE under compression along the *y* ($\varepsilon_{yy} = -0.266$, X-shape deformation mode) and *x* ($\varepsilon_{xx} = -0.255$, N-shape deformation mode) directions, respectively.

Although these plots confirm the difference in deformation behavior of the structure in the two directions, several important similarities exist. For instance, in both these directions, upon increasing the compressive strain, the transverse strain rises from zero (i.e., undeformed configuration) up to a turning point, and then decreases until it becomes zero at ~10% compressive strain, **Figure 3.3 (a)**. After this point, the transverse strain becomes negative showing lateral contraction (i.e., negative Poisson's ratio). This similarity is further confirmed through Poisson's ratio variation with longitudinal strain in two directions ($\nu_{xy} = -\varepsilon_{yy}/\varepsilon_{xx}$ and $\nu_{yx} = -\varepsilon_{xx}/\varepsilon_{yy}$), **Figure 3.3 (b)**. Note that small deformation Poisson's ratios (~0.9) are in agreement with published literature [76]. The

Poisson's ratio decreases as the strain is increased: first, slowly as also seen for honeycombs with no hierarchy, and then follows by a sharp decrease due to instability. Negative Poisson's ratio is achieved at ~10% compressive strain. Thereafter, the rate of reduction becomes smaller indicating the formation of a plateau regime with $\nu \cong -0.5$ as the plateau Poisson's ratio.

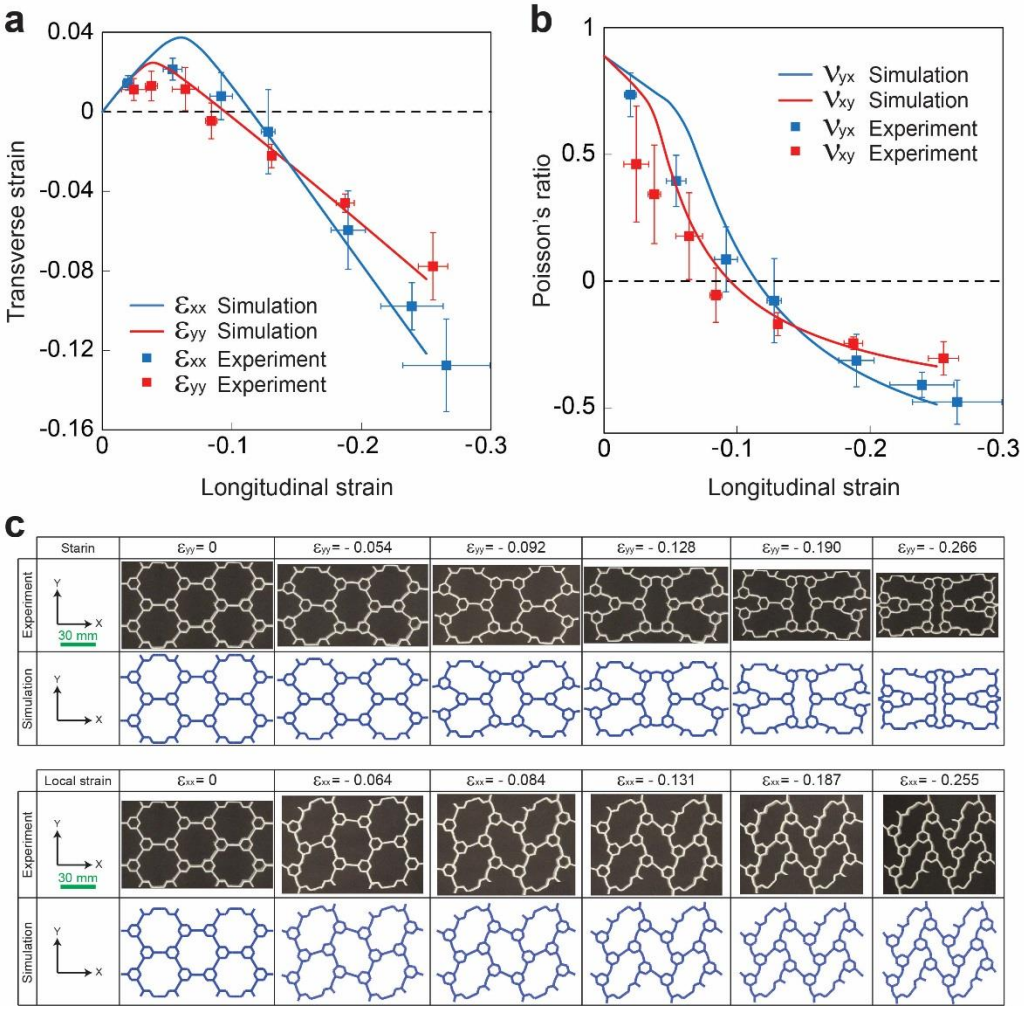

Figure 3.3 Validating the experiments using numerical simulations. **a)** Transverse strain, and **b)** Poisson's ratio, versus longitudinal strain for both loading directions. The solids lines denote the simulation results and markers represent the experimental data. The error bars on the experimental points show the standard deviation of the values of the strain (and Poisson's ratio) measured at different locations on the RVE. **c)** Experimental and numerical images of deformed configuration of the RVE at different levels of deformation.

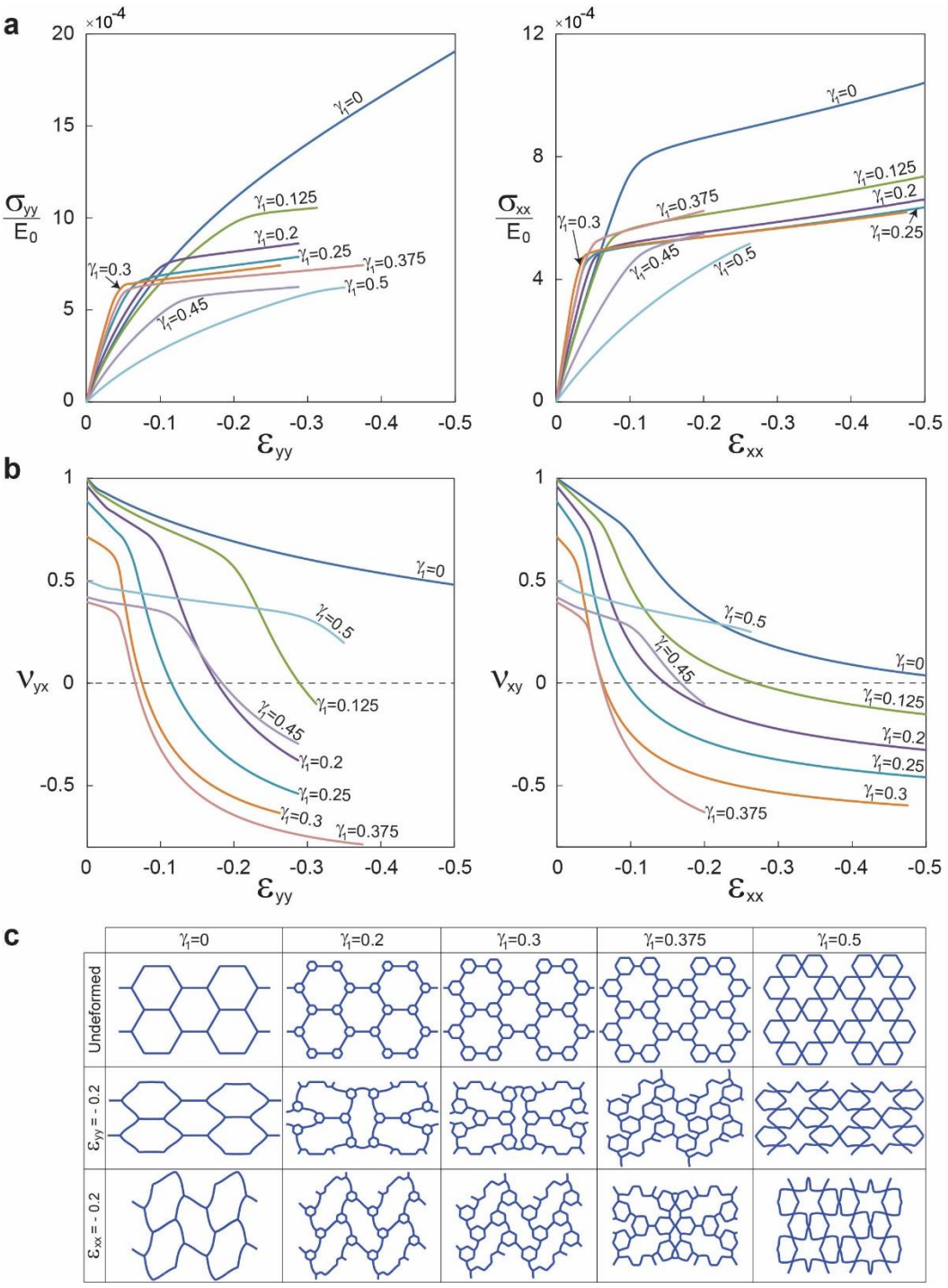

Figure 3.4 Strain-dependent response of first order hierarchical honeycombs. **a)** Stress-strain curves, and **b)** the evolution of Poisson's ratio versus longitudinal strain for uniaxial compression along the *y* and *x* directions. The stress is normalized with respect to the initial Young's modulus of the cell wall material (E_0). **c)** Undeformed and deformed configurations of the RVEs at 20% compression.

To further investigate the auxetic behavior of hierarchical honeycombs, we extend our validated simulations to study the effect of the parameter, γ_1, on uniaxial compressive response of the structures with first order of hierarchy. Although no dynamic calculations were performed in this study, in order to isolate the effect of hierarchy, the relative density was kept constant at 8% for these simulations performed on the RVE as earlier. The results are presented for eight different values of γ_1, varying from 0 (i.e., regular hexagonal honeycomb) to 0.5. **Figure 3.4 (a)** plots the evolution of the normalized nominal stress, σ/E_0 (where E_0 is the initial Young's modulus of the cell wall material), versus the applied longitudinal strain, ε. We find that no instability occurs in the structures with $\gamma_1 = 0$ and 0.5 for compression along the *y* direction. In fact, the structures' deformation is symmetrical and is formed by static deflection of the cell walls due to bending (see **Figures 3.4 (a)** (left) and **3.4 (c)** (middle row)). In contrast, for $0 < \gamma_1 < 0.5$, the response of the structure is characterized by a linear elastic regime followed by elastic buckling resulting in a stress plateau (i.e., a typical response for cellular solids). Similar phenomenon is observed for compression along the *x* direction (see **Figure 3.4 (a)** (right)) except for the structure with $\gamma_1 = 0$ in which the elastic buckling (in contrast to the other loading direction) is observed (i.e., uniaxial mode of buckling of a regular hexagonal honeycomb (see **Figure 3.4 (c)** (bottom row)) [75]).

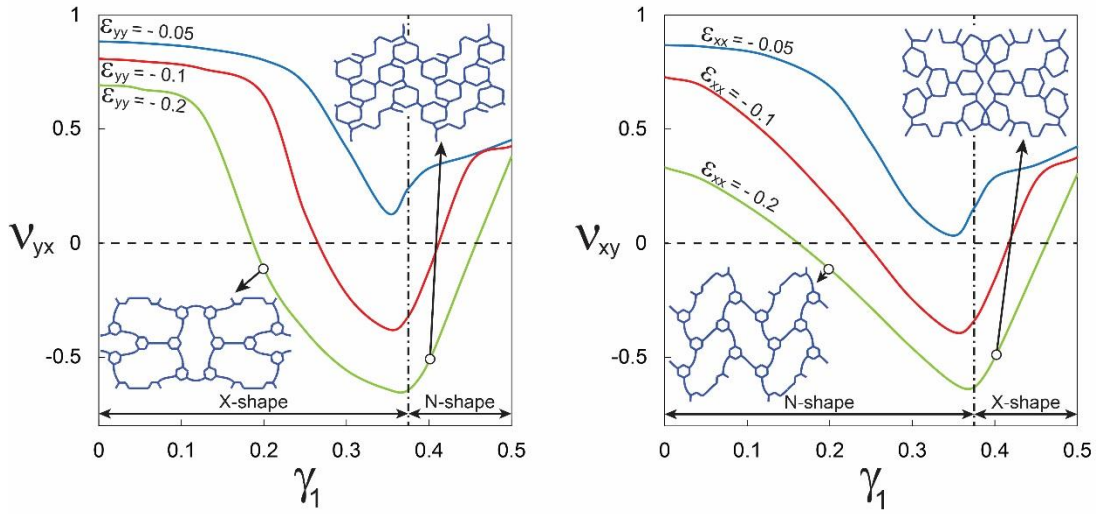

Figure 3.5 The evolution of Poisson's ratio as a function of γ_1 at 5, 10, and 20% compression along the *y* and *x* directions. The vertical dashed lines represent the point in which the Poisson's ratio is minimum and the deformation mode switches.

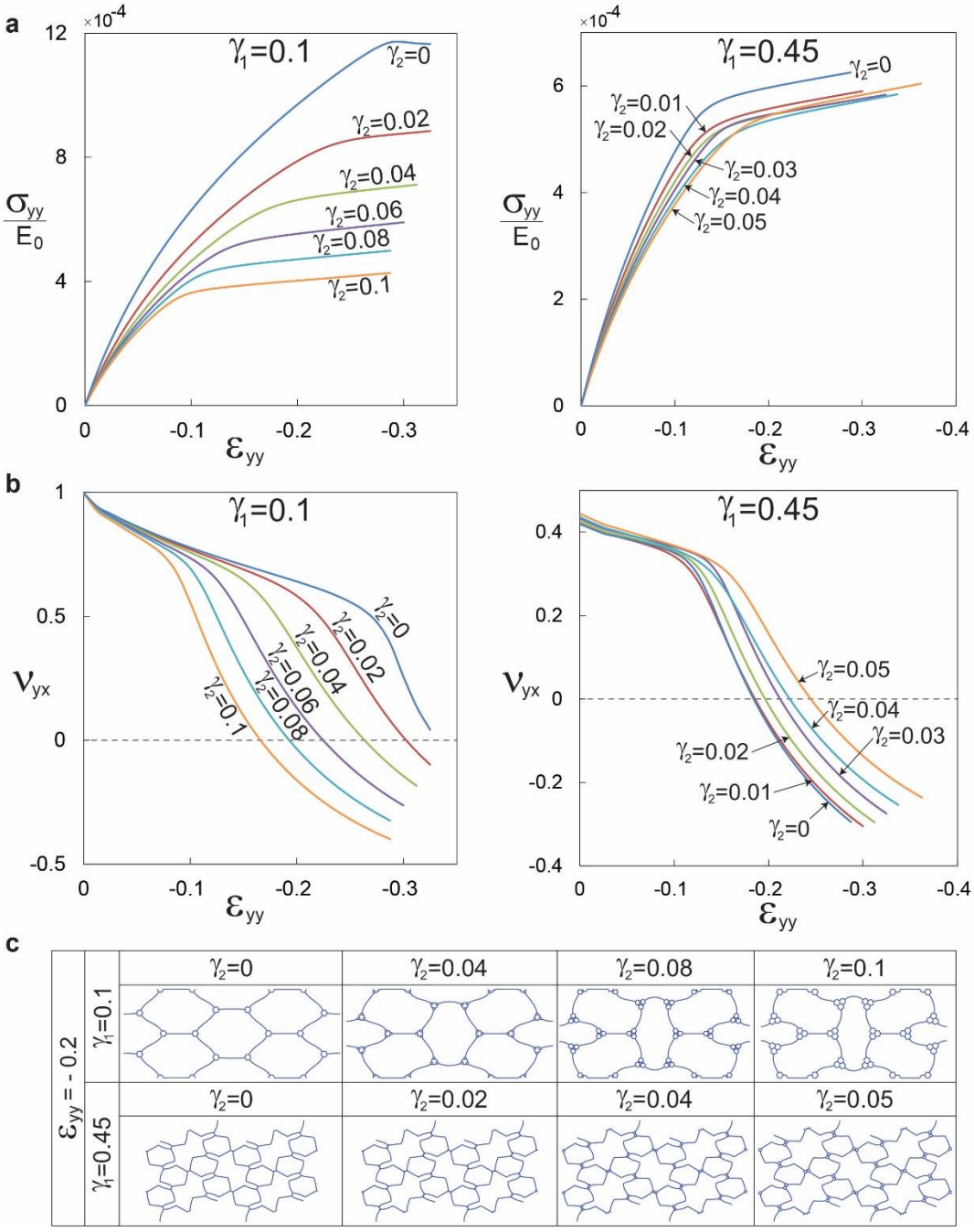

Figure 3.6 Honeycombs with second order of hierarchy. **a)** Stress-strain curves, and **b)** the evolution of Poisson's ratio versus longitudinal strain, for second order hierarchical structures with $\gamma_1 = 0.1$ and $\gamma_1 = 0.45$, under uniaxial compression along the *y* direction (see Supplementary Information for loading along the *x* direction). The stress is normalized with respect to the initial Young's modulus of the cell wall material (E_0). **c)** Deformed configuration of the RVEs at 20% compression.

Next, **Figure 3.4 (b)** which shows the evolution of Poisson's ratio with longitudinal strain in both directions, indicates that in either direction of loading, for structures with no instability, Poisson's ratio remains positive and smoothly decreases with deformation. On the other hand, Poisson's ratio for the structures with elastic instability exhibits an initial slow decrease from the small deformation positive value transitioning to a negative regime via a sharp drop. Our simulations showed that this sharp transition can be further advanced by increasing γ_1 which also lowers Poisson's ratio for a given deformation. Interestingly, we find that this trend is abruptly arrested at around $\gamma_1 \approx 0.375$, and then reversed for higher γ_1 making it an important design parameter. Shedding greater light on this critical point, **Figure 3.4 (c)**, which shows the deformed configuration of the RVEs at 20% compressive strain for different geometries, reveals that the fundamental origin of this critical point is a switch in deformation mode at $\gamma_1 \approx 0.375$ from X-shape to N-shape and vice versa for compression along the *y* and *x* directions, respectively. It is interesting to note that the γ_1 corresponding to this critical point also results in the lowest possible Poisson's ratio. **Figure 3.5** displays the evolution of Poisson's ratio against γ_1 at 5, 10, and 20% longitudinal strain for both loading directions, showing that Poisson's ratio reaches a minimum at $\gamma_1 \approx 0.375$, corresponding to the switching of the buckling modes.

Investigating the role of hierarchy further, we computationally study honeycombs with two orders of hierarchy with $\gamma_1 = 0.1$ and 0.45 under uniaxial compression along the *y* direction (see **Appendices** for loading along the *x* direction, exhibiting similar behavior). Carrying out FE simulations on RVEs with relative density held constant at 8%, we plot the normalized nominal stress against the applied strain, **Figure 3.6 (a)**. The effect of second order of hierarchy depends on γ_1 values. For instance, the plateau stress decreases dramatically upon introducing second order of hierarchy into a structure with $\gamma_1 = 0.1$ (see **Figure 3.6 (a)** (left)) in contrast to the structure with $\gamma_1 = 0.45$ (see **Figure 3.6 (a)** (right)). More dramatically, second order of hierarchy can significantly advance auxeticity by significantly reducing the Poisson's ratio with deformation for the $\gamma_1 = 0.1$ case (**Figure 3.6 (b)** (left)) whereas having an opposite effect for the $\gamma_1 = 0.45$ case. The contrasting behavior stems from the overall size of the smaller hexagons in the hierarchical structure, rather than from any fundamental change of buckling modes of the underlying structure due to introduction of the second order of hierarchy as confirmed in **Figure 3.6 (c)**.

Essentially, introducing a higher order of hierarchy increases the overall size of the smaller hexagons, and this acts like increasing γ_1 without increasing the order of hierarchy. Recalling our discussion from first order hierarchical structures, this makes the structures with γ_1 less than the turning point value (≈ 0.375) achieve a smaller Poisson's ratio (moving left to right in **Figure 3.5**) while the opposite being true for γ_1 greater than this turning point value (also moving left to right in **Figure 3.5**).

3.4 Discussion and Conclusions

In summary, our experimental and computational study provides new insights on the behavior of auxetic metamaterials with structural hierarchy. We found that hierarchy-dependent elastic buckling introduced at relatively early stages of deformation decreases the value of Poisson's ratio as the structure is compressed uniaxially leading to auxeticity in subsequent stages of deformation. This extraordinary behavior, which originates from structural hierarchy, has not been observed in the non-hierarchical regular structure, in spite of topical similarities in deformation modes. Our proposed hierarchical architecture is unique in exhibiting two different deformation modes for structures with different geometrical parameters when compressed along the same direction. An optimal design in terms of the lowest Poisson's ratio is achieved among the structures with first order of hierarchy, which interestingly corresponds to a point in which the buckling modes switch. The auxetic response can further be pronounced (i.e., lower Poisson's ratio) by introducing higher orders of hierarchy. Our results provide new insights into designing energy absorbing materials and tunable membrane filters [100, 122].

However, the main limitation of our proposed hierarchical architecture is the range of the strain at which the Poisson's ratio becomes negative (i.e., critical strain ~10%). It is desirable to achieve auxetic behavior at much smaller strains for many practical applications. To reduce the critical strain, we tailor the geometry of the hierarchical structure for lowest critical strain. For instance, a hierarchical structure with first order of hierarchy has the lowest critical strain (~6%) for the geometry at which the switching of the buckling modes occurs and Poisson's ratio attains the lowest value among all first order

hierarchical structures. Interestingly, the critical strain can further be reduced by introducing higher orders of hierarchy as we demonstrated for second order of hierarchy.

3.5 Methods

Materials. A rubber-like flexible material (commercial name TangoGray, with material properties presented in **Appendices**) was used to 3D print the experimental specimen. The material properties were measured through tensile testing on dog-bone specimens up to the strain of $\varepsilon \sim 0.3$. G_0=1.7 MPa and K_0=84.43 MPa are the initial shear and bulk moduli in the undeformed configuration and they are obtained by fitting the response under uniaxial tension of the bulk material (see **Appendices** for more details).

Fabrication using 3D printing. The specimen was fabricated using PolyJet 3D printing technique (Objet Eden260V 3D printer, Stratasys Inc., Eden Prairie, MN) out of TangoGray material. The specimen has overall size of Width × Hight × Depth = 254 × 229 × 20 mm with wall thickness of 1 mm, maintaining a relative density of 8% for $\gamma_1 = 0.25$. Prior to testing in either direction, two aluminum plates were attached to the top and bottom of the specimen to prevent the edge nodes from excessive bending.

Mechanical testing. We applied uniaxial compression along the *y* and *x* directions using an Instron 5582 testing machine with a 1 KN load cell. In order to calculate the Poisson's ratio at each level of applied compression, the photographs of deformed configurations of the specimen were recorded using a digital camera (See **Appendices** for more details).

Numerical simulations. The commercial FE package ABAQUS (SIMULIA, Providence, RI) was employed to carry out all the simulations in this study. Both microscopic and macroscopic instability analyses as well as post-buckling analysis were performed using the ABAQUS/Standard solver. The 2D FE models of periodic unit cells for the first and second order of hierarchical honeycomb were constructed using beam elements (ABAQUS hybrid element type B22H) and the accuracy of the mesh is insured by a mesh refinement study. The models were subjected to uniaxial static compression

along the *y* and *x* directions while the lateral contractions were monitored. The first four eigenvalues from the instability analysis were employed to model imperfections in non-linear post-buckling analysis.

3.6 Appendices

3.A Hierarchical honeycombs

The first order of hierarchy is obtained by replacing all three-edge nodes of a regular hexagonal honeycomb with smaller, parallel hexagons. This procedure can be repeated at smaller scales to achieve higher orders of hierarchy, yet the thickness of the cell walls must be reduced simultaneously to keep the overall density fixed. **Figure 3.1** shows the evolution of a regular hexagonal honeycomb and its corresponding cell as the order of hierarchy is increased.

The structural organization of the structure at each order of hierarchy (γ_i) is defined by the ratio of the newly added hexagonal edge length (b for first order and c for second order of hierarchy) (see **Figure 3.1**) to the original hexagon's edge length (a) (i.e., $\gamma_1 = b/a$ and $\gamma_2 = c/a$) [76]. For first order of hierarchy, $0 \leq b \leq a/2$ and thus, $0 \leq \gamma_1 \leq 0.5$, where $\gamma_1 = 0$ represents the regular hexagonal honeycomb. For a structure with second order of hierarchy, $0 \leq c \leq b$ and $c \leq a/2 - b$ and thus, $0 \leq \gamma_2 \leq \gamma_1$ if $\gamma_1 \leq 0.25$, and $0 \leq \gamma_2 \leq (0.5 - \gamma_1)$ if $0.25 \leq \gamma_1 \leq 0.5$. These geometrical constraints must be imposed on the structures to avoid overlapping edges. The dimensionless relative density (i.e., area fraction), compared to the material density, is given as:

$$\rho = 2/\sqrt{3}\ .(1 + 2\gamma_1 + 6\gamma_2)\ .t/a \tag{3.A.1}$$

where t is the wall thickness which is assumed to be uniform throughout the structure.

3.B Experimental specimen - material properties

We used a rubber-like flexible material (commercial name TangoGray) as the bulk material to fabricate the specimen. To measure the material properties, five dog-bone specimens were 3D printed and tested under uniaxial tensile loading, and the stress-strain response of the material (i.e., engineering stress vs. engineering strain) is monitored up to the strain of $\varepsilon = 0.3$ (see **Figure 3.B.1**). Since the test was performed quasi-statically, we neglected viscoelastic effect and captured the constitutive behavior using a nearly-incompressible Neo-Hookean hyperelastic model (Poisson's ratio: $\nu_0 = 0.49$), whose strain energy is given by $U = G_0(\bar{I}_1 - 3)/2 + K_0(J-1)^2/2$, where $\bar{I}_1 = J^{-2/3}\,\mathrm{tr}[\mathrm{dev}(\mathbf{F}^{\mathrm{T}}\mathbf{F})]$, $\mathrm{J} = \det(\mathbf{F})$, and **F** is the deformation gradient. We obtained the initial shear modulus (G_0=1.7 MPa) and bulk modulus (K_0=84.43 MPa) in the undeformed configuration by fitting the material model to the experimental data (see **Figure 3.B.1**). The mechanical tests were performed based on ASTM-D638-10, which is the standard test method for measuring tensile properties of plastics.

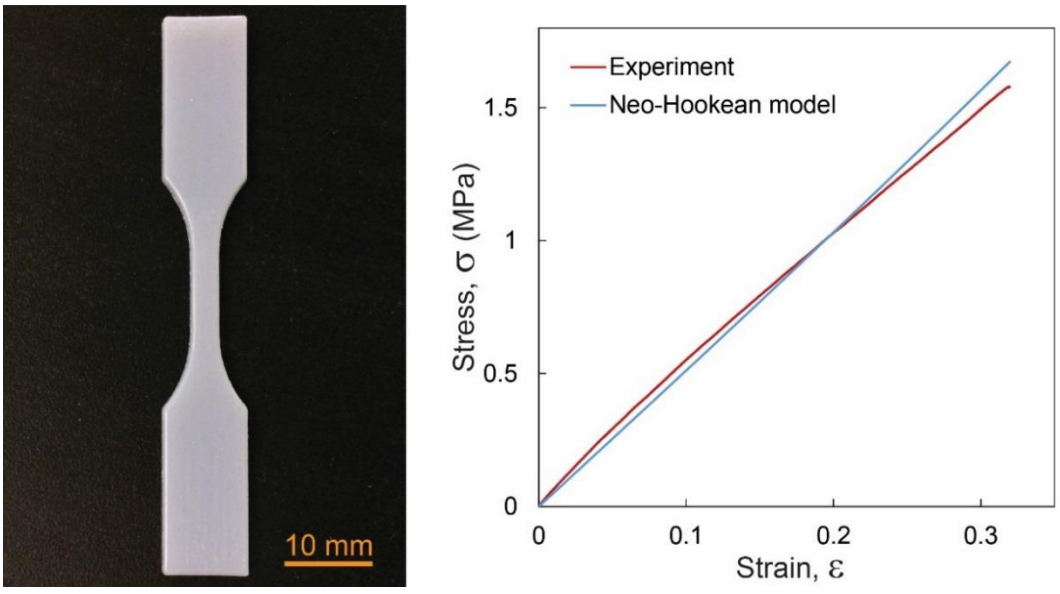

Figure 3.B.1 (Left) 3D printed dog-bone specimen for uniaxial tension test. (Right) Engineering stress vs. engineering strain for the tested material.

3.C Experiments

The specimen was fabricated using PolyJet 3D printing technique out of TangoGray material which has an overall size of Width × Hight × Depth = 254 × 229 × 20 mm with wall thickness of 1 mm, maintaining a relative density of 8% for $\gamma_1 = 0.25$. Next, we applied uniaxial compression along the *y* and *x* directions using an Instron 5582 testing machine with a 1 KN load cell. In order to calculate the Poisson's ratio at each level of applied compression, the photographs of deformed configurations of the specimen was recorded using a digital camera. Then, we tracked RVEs' boundary points (i.e., the points in touch with adjacent RVEs) to obtain their locations at different levels of deformation and used them to measure the horizontal and vertical distances (i.e., Δx and Δy, see **Figure 3.C.1**) needed to evaluate the local strains (i.e., $\varepsilon_{xx} = \Delta x/\Delta x(0)$ and $\varepsilon_{yy} = \Delta y/\Delta y(0)$). The measurement was repeated at least at five different locations on the RVE at each level of compression. The Poisson's ratio is then calculated as $\nu_{xy} = -\varepsilon_{yy}/\varepsilon_{xx}$ and $\nu_{yx} = -\varepsilon_{xx}/\varepsilon_{yy}$.

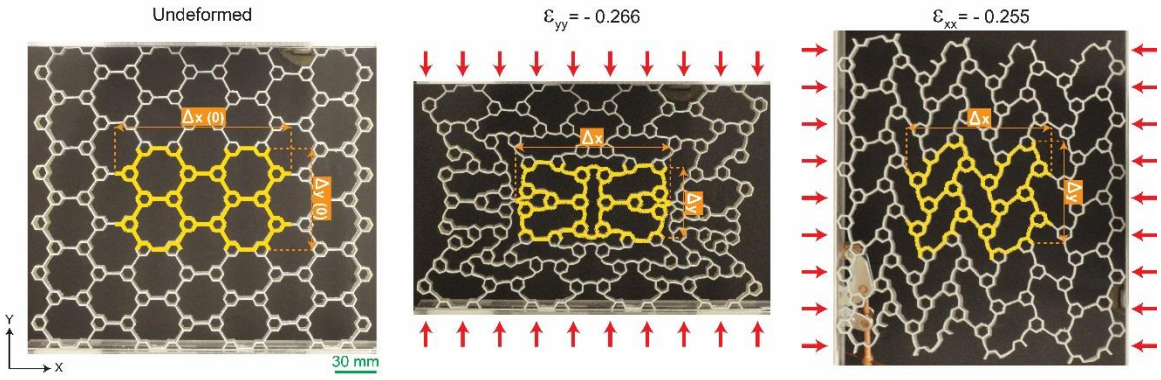

Figure 3.C.1 Hierarchical honeycomb auxetic metamaterials: experimental setup. (left) Undeformed configuration of the fabricated first order hierarchical structure with $\gamma_1 = 0.25$. The representative volume element (RVE) is highlighted as yellow. (middle and right) Deformed configurations of the specimen and the RVE under compression along the *y* ($\varepsilon_{yy} = -0.266$, X-shape deformation mode) and *x* ($\varepsilon_{xx} = -0.255$, N-shape deformation mode) directions, respectively.

3.D Second order of hierarchy – additional results

We performed FE simulations on second order hierarchical structures with $\gamma_1 = 0.1$ and 0.45 under uniaxial compression along the *x* direction. The relative density was kept constant at 8%. The results are presented in **Figure 3.D.1** in the form of the normalized nominal stress (**Figure 3.D.1.a**) and Poisson's ratio (**Figure 3.D.1.b**) versus the applied compressive strain. Deformed configuration of the RVEs at 20% compressive strain is also presented in **Figure 3.D.1.c**. The results presented in **Figure 3.D.1**, which show the effect of the second order of hierarchy on auxetic response of hierarchical honeycombs, are similar to the results presented in **Figure 3.6** for compression in y direction.

Next, **Figure 3.D.2** plots the evolution of Poisson's ratio against γ_2 at 20% compressive strain for second order hierarchical structures with $\gamma_1 = 0.1$ and 0.45. The figure clearly shows that second order of hierarchy reduces the value of Poisson's ratio for the structure with $\gamma_1 = 0.1$, whereas the opposite is true for the structure with $\gamma_1 = 0.45$. The reason for this behavior relies on the overall size of the smaller hexagons in the hierarchical structure. Introducing a higher order of hierarchy increases the overall size of the smaller hexagons, and this acts like increasing the value of γ_1 without increasing the order of hierarchy. This makes the structures with $\gamma_1 < 0.375$ to achieve a smaller Poisson's ratio (moving from left to right in **Figure 3.5**) with the opposite being true for $\gamma_1 > 0.375$ (moving from left to right in **Figure 3.5**).

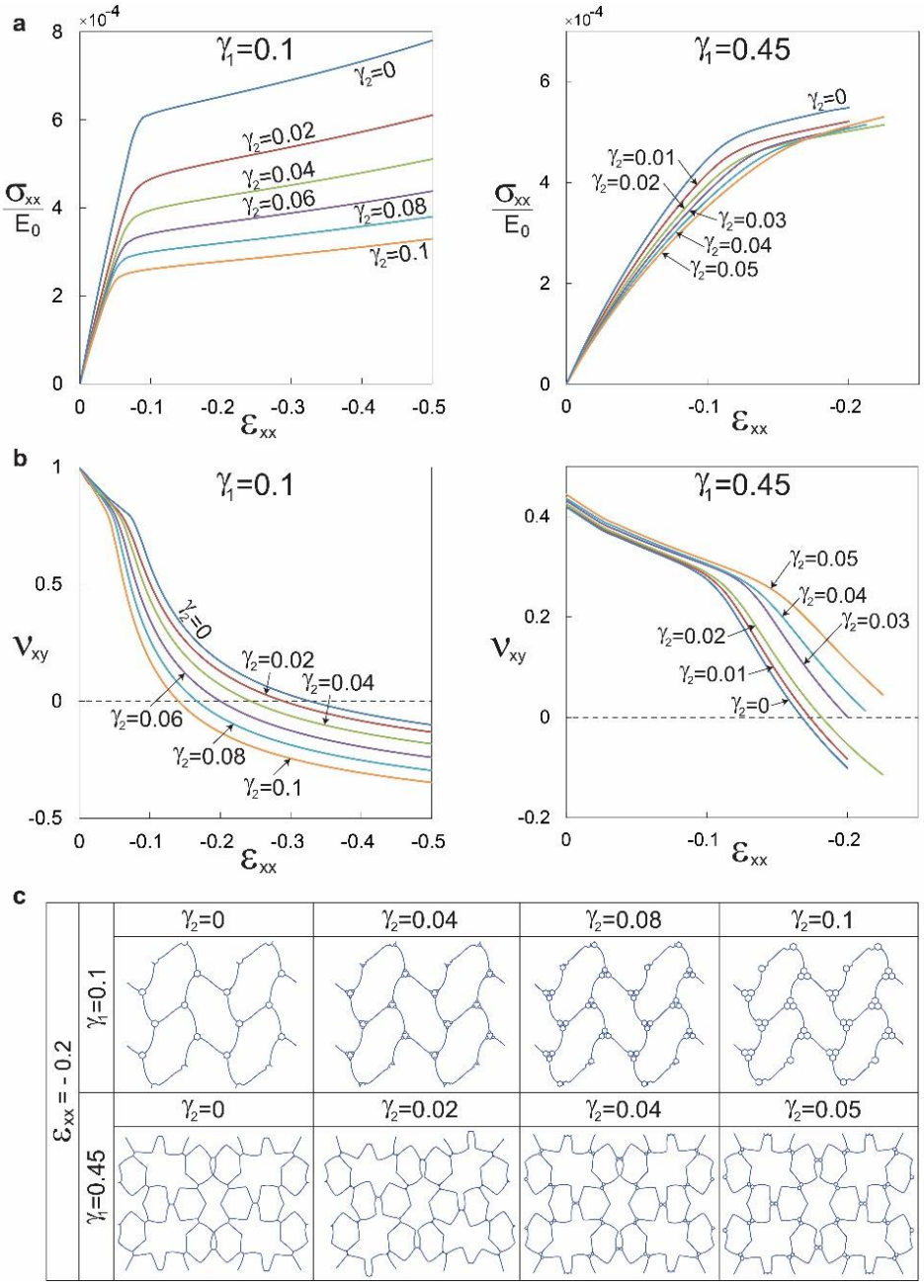

Figure 3.D.1 Honeycombs with second order of hierarchy. **a)** Stress-strain curves, and **b)** the evolution of Poisson's ratio versus longitudinal strain, for second order hierarchical structure with $\gamma_1 = 0.1$ and $\gamma_1 = 0.45$, under uniaxial compression along the *x* direction. The stress is normalized with respect to the initial Young's modulus of the cell wall material (E_0). **c)** Deformed configuration of the RVEs at 20%.

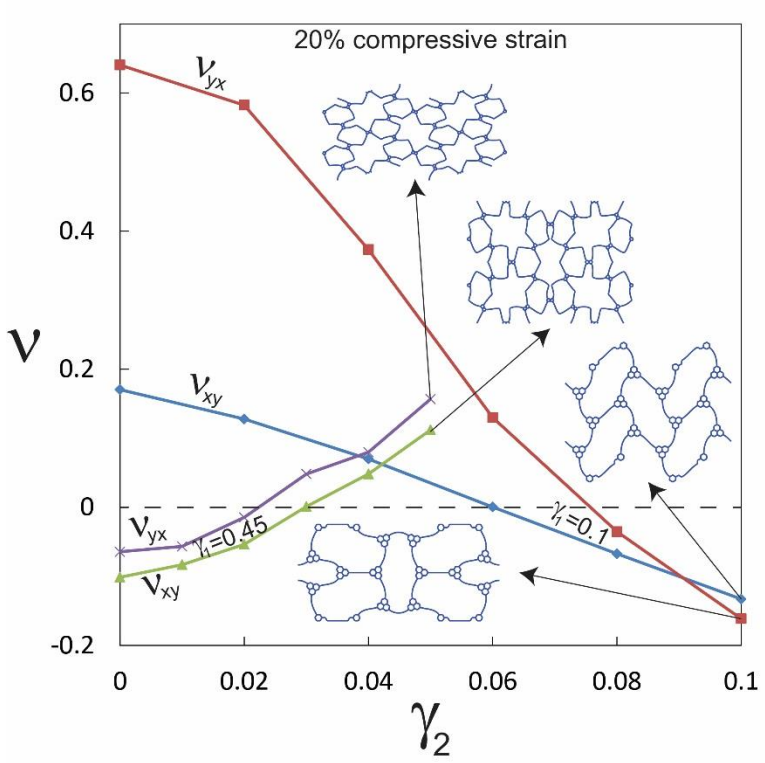

Figure 3.D.2 Poisson's ratio vs. γ_2 for second order hierarchical structures with γ_1=0.1 and 0.45.

Chapter 4

Honeycomb Phononic Crystals with Self-similar Hierarchy

4.1 Abstract

We highlight the effect of structural hierarchy and deformation on band structure and wave-propagation behavior of two-dimensional phononic crystals. Our results show that the topological hierarchical architecture and instability-induced pattern transformations of the structure under compression can be effectively used to tune the band gaps and directionality of phononic crystals. The work provides insights into the role of structural organization and hierarchy in regulating the dynamic behavior of phononic crystals, and opportunities for developing tunable phononic devices.

4.2 Introduction

Hierarchical organization is ubiquitous in biological systems, from the nanometer to the macroscopic length scales. Examples include collagen [7], bone [9, 123], tooth [123], tendon [9], wood [9, 13], nacre [12], gecko foot pads [124], Asteriscus plant [125], Euplectella sponge [6], and water-repellant biological systems [126]. The purely structural role of hierarchy in boosting mechanical performance is now well known [11, 54, 61, 115, 127]. In addition to hierarchy, periodic organizations aimed at influencing the wave-propagation behavior, for instance in structural colorations, can also be found in nature [128-130]. More interestingly, the reversible modulation of these so-called phononic crystals through deformation provides an incredibly rich optical behavior enhancing their survival [131, 132].

Pursuing these synergetic motifs for materials development [133-136], we investigate a different class of hierarchical organization based on 2D honeycomb-like structures primarily geared towards phononic applications (i.e., phononic crystals) and the effect of deformation on controlling their band gaps (defined as frequency ranges of strong wave attenuation). To this end, 2D lattices with different nonhierarchical topologies have been well investigated (no deformation included) [137-139]. However, recently, Xu et al. [140] investigated wave propagation in 2D hexagonal lattice structures with sandwich plate cell walls possessing only first-order non-self-similar hierarchy. This early study, although lacking a systematic analysis of the role of hierarchy in fostering phononic properties, provided an early evidence of expansion of band gaps with hierarchy.

In this dissertation, we study the effect of structural hierarchy on the band structure and directionality of these crystals, as well as investigate the additional effect of compressive loads on the tunability of band gaps of first-order hierarchical phononic crystals. Interestingly, our results reveal that hierarchy and pattern transformations through compression can significantly affect the dynamic response, and they can be effectively used to tune the propagation of elastic waves in phononic crystals.

The evolution of a regular honeycomb into the fractal-like hierarchical phononic crystal studied in this dissertation is illustrated schematically in **Figure 4.1**. The structural organization of the honeycomb at each order of hierarchy (γ_i) is defined by the ratio of the

newly introduced hexagonal edge length (l_i) to the previous hexagon's edge length (l_{i-1}), i.e., $\gamma_i = l_i/l_{i-1}$. For convenience, γ_1 is defined as $\gamma_1 = 2l_1/l_0$ (see **Figure 4.1 (a)**) [54]. The following geometrical constraints must be imposed on the structure to avoid overlapping edges:

$$\begin{cases} 0 \le \gamma_n \le 1 \\ \sum_{i=1}^{n} \prod_{j=1}^{i} \gamma_j \le 1 \end{cases} \tag{4.1}$$

where n is the order of hierarchy ($n \ge 1$). The dimensionless relative density (equal to area fraction) of the structure [compared to the material density (ρ_s)], i.e., $\rho_c = \rho/\rho_s$, is given as the following:

$$\rho_c = \frac{2}{\sqrt{3}}\left(1 + \sum_{i=1}^{n} 3^{i-1} \prod_{j=1}^{i} \gamma_j\right)\frac{t_n}{l_0} \tag{4.2}$$

where t_n is the wall thickness which for simplicity is assumed to be uniform throughout the structure. Thus, thickness (t_n) must decrease to maintain a fixed relative density (ρ_c) as the order of hierarchy (n) and the values of γ_i are increased.

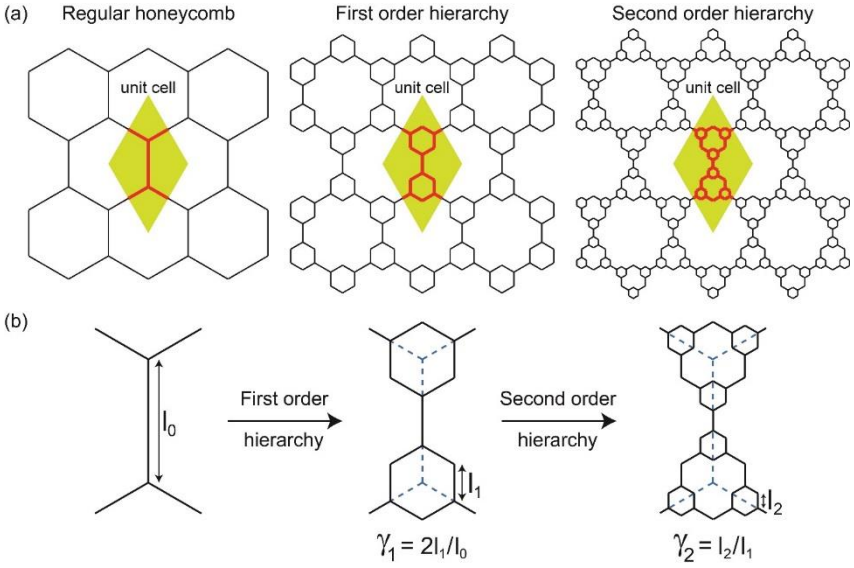

Figure 4.1 Hierarchical honeycombs. **(a)** The evolution of a regular hexagonal honeycomb (left) to first-order (middle) and second-order (right) hierarchical honeycombs. **(b)** Corresponding primitive unit cells of the structures.

4.3 Results and discussions

We consider the structure to be infinitely extended in 2D space and the advancing wavefront to induce no finite strains to model waves of low intensity with wavelengths of the order of lattice characteristic size. Numerical simulations of the propagation of these small-amplitude elastic waves in the crystal (in undeformed configuration) were performed using Finite Element (FE) method and Bloch wave analysis [141] (see **Appendices** for more details). In the FE models, honeycomb walls were modeled as Timoshenko beams with a rectangular cross section of unit length normal to the plane of wave motion, and the material was assumed to be aluminum with Young's modulus $E_s = 71GPa$, Poisson's ratio $\nu_s = 0.33$, and density $\rho_s = 2700\,\mathrm{kg/m^3}$. The relative density of the structure was kept constant at 8%. The frequency of the propagating wave (ω) was normalized with respect to the first flexural frequency of a simply supported beam with length l_0 and thickness t_0, that is $\Omega = \omega/\omega_0$, where $\omega_0 = \pi^2\sqrt{E_s {t_0}^2/\left(12\rho_s {l_0}^4\right)}$ [138].

We compare in **Figure 4.2**, the band structures and directionality diagrams of a regular honeycomb (left column) and a first order hierarchical structure with $\gamma_1 = 0.5$ (right column). In **Figure 4.2 (a)**, we report the normalized frequency as a function of the reduced wave vector (see **Appendices** for more details). For the considered frequency range, the regular structure features a band gap at $\Omega = 4.56 - 5.46$. On introducing hierarchy, the lowest frequency band gap is now much lower ($\Omega = 2.01 - 2.85$) and several other new band gaps appear in the considered frequency range ($\Omega = 5.77 - 10.22, 11.67 - 12.38$). Another pre-existing band gap is also shifted to the lower frequency at $\Omega = 13.16 - 13.55$. This considerable change in the band structure is due to the newly added hexagons (brought about by hierarchy), which also reduce the cell wall thickness to conserve mass. This geometrical change results in an increase in multiple scattering of the propagating waves at the cell walls and consequently opening up the Bragg-type band gaps [142]. The alterations of the band structure indicate a hierarchy dependent transition, which parallels the effect of hierarchy on mechanical behavior in other contexts [11, 54, 61, 115, 127].

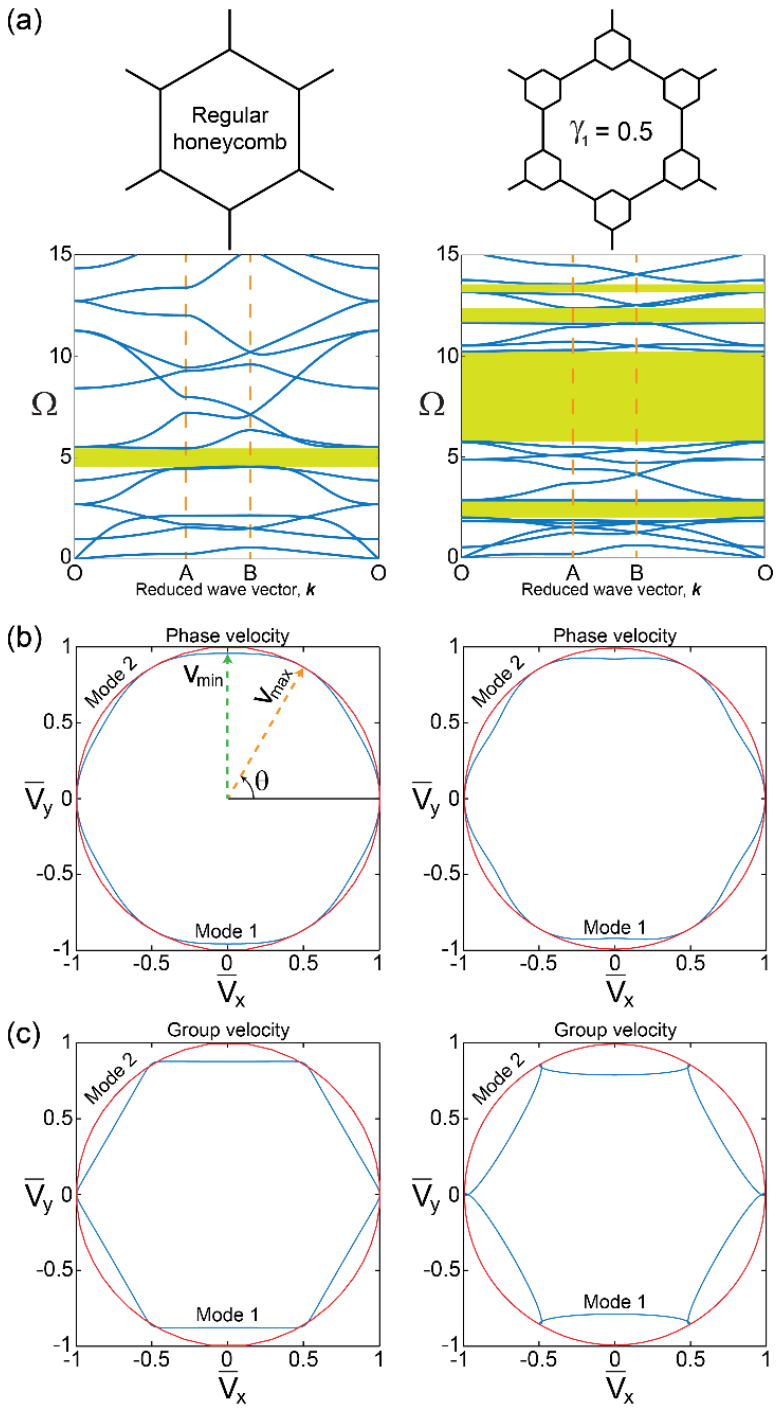

Figure 4.2 Regular hexagonal honeycomb vs. a first order hierarchical honeycomb with $\gamma_1 = 0.5$. **(a)** Effect of hierarchy on band gaps. **(b,c)** Effects of hierarchy on the directionality of phase and group velocities.

Since band diagrams such as **Figure 4.2 (a)** cannot always fully provide the directional behavior of a lattice structure, they are often investigated using dispersion surfaces (in compact form: phase and group velocities) [143]. In rapidly expanding broadband applications, it is crucial to focus on the low frequency regime in addition to more well investigated high frequency behavior [137, 144, 145]. **Figures 4.2 (b)** and **4.2 (c)** respectively present the phase and group velocity profiles for the lowest two modes of propagating waves at relatively low frequency of $\Omega = 0.1$. Each velocity profile is normalized with respect to the maximum velocity of the profile (V_{max}) (see **Figure 4.2 (b)**). For the regular structure (left column), the phase velocity profile exhibits a slight preference in the direction of propagation at $\theta = 0^{\circ}$, $\theta = 60^{\circ}$, and due to symmetry, at $\theta = 120^{\circ}$ for mode 1 (shear or S-mode), whereas it does not show any preferential direction for mode 2 (longitudinal or L-mode). Hierarchy seems to have no effect on the relative isotropy of mode 2. However, anisotropy of mode 1 is further accentuated due to hierarchy. The origin of this effect can be traced to decreased thickness of the original cell walls due to additional hexagons resulting in an increase in the relative anisotropy ratio V_{max}/V_{min}. Group velocity, which typically indicates the velocity at which energy is transported along the wave vector, also reflects this anisotropy concentration of mode 1 in **Figure 4.2 (c)** for both the regular and hierarchical structures.

Next, we investigate the effects of the hierarchical order (n) and geometrical ratios ($\gamma_i's$) on band gaps and wave directionality. For convenience, we limited the analysis to self-similar hierarchical honeycombs up to third order of hierarchy with self-similarity ratio, η, defined as $\eta = \gamma_n = \gamma_{n-1} = \cdots = \gamma_1$ for n^{th} order of hierarchy with n =1, 2, and 3, respectively for first, second, and third orders of hierarchy. The geometrical constraints given in **Equation (4.1)** limit the maximum value of η at each order of hierarchy to η_{max} = 1, 0.62, and 0.54, respectively for first, second, and third orders of hierarchy.

Figures 4.3 (a), **4.3 (b)**, and **4.3 (c)** show the evolution of band gaps as the value of η increases, respectively for first, second, and third orders of hierarchy for the range of frequencies, $0 \leq \Omega \leq 10$. Note that the upper bound of the horizontal axis is limited to η_{max}. For $n = 1$ (**Figure 4.3 (a)**), introducing hierarchy is found to at first, lower the midgap position of the original non-hierarchical band gap, although the width of the band

gap remains fairly the same. Thereafter, a slender band gap appears on either side of this central band gap. Increasing η, opens up another band gap at higher frequencies which continues to expand as the original dominant band narrows. After $\eta \approx 0.35$ this original band gap disappears giving way to two separate band gap flanges which first expand and then disappear giving further band gap flanges. This waxing and waning pattern of band gaps continues as newer band gaps emerge and disappear. Similar phenomena are observed for higher orders of hierarchy (see **Figure 4.3 (b)** and **4.3 (c)**). The results presented in **Figures 4.3 (a)**, **4.3 (b)**, and **4.3 (c)** confirm that the order of hierarchy and self-similarity ratio are two important geometric parameters affecting the band structure. This has important implications on the critical gap/midgap ratio for phononic applications [146].

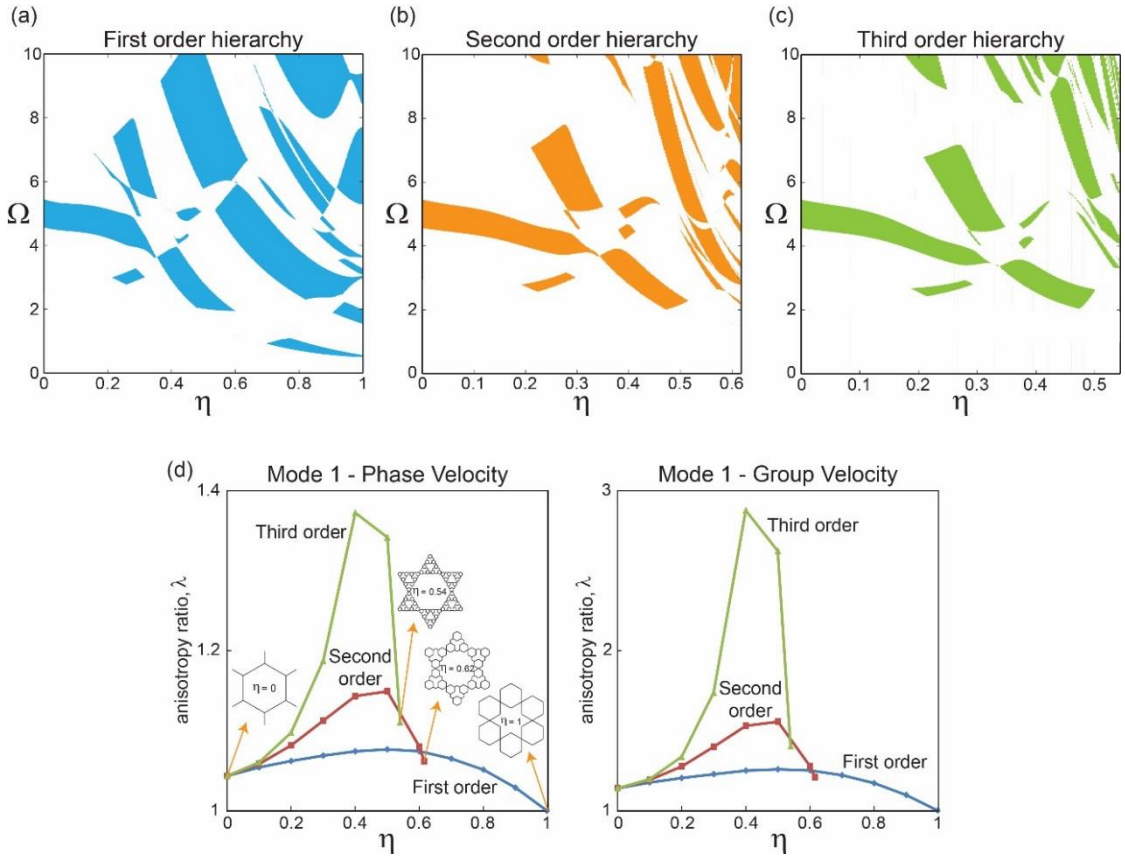

Figure 4.3 (a, b, c) The evolution of band gaps as a function of self-similarity ratio (η) for hierarchical honeycombs with first, second, and third, orders of hierarchy. **(d)** The evolution of anisotropy ratio (λ) as a function of self-similarity ratio (η) for phase, and group velocity profiles for mode 1 of propagating waves.

To study the directionality of propagating waves at low frequency of $\Omega = 0.1$, we define the following scalar anisotropy ratio [142]:

$$\lambda = V_{max}/V_{min} \tag{4.3}$$

where V_{max} and V_{min} are the maximum and minimum wave velocities, respectively (**Figure 4.2 (b)**). Note that $\lambda \geq 1$, with $\lambda = 1$ showing an isotropic media where elastic waves propagate with the same speed in every spatial direction with no preference (i.e., the polar plot of wave velocity is circular). We report in **Figure 4.3 (d)** the evolution of anisotropy ratio as η increases for phase and group velocity profiles for mode 1 of propagating waves. Note that the phase and group velocity profiles of the structures for mode 2 do not show any preferential direction of propagation indicating isotropic response (i.e., $\lambda = 1$). **Figure 4.3 (d)** shows that for mode 1, λ of both the phase and group velocity profiles rise from the initial values ($\eta = 0$, regular structure) up to a turning point (critical point), then decrease as a function of η restoring isotropy. This behavior is entirely due to the redistribution of matter within the crystal resulting in an initial increase of scattering in the smaller hexagons whose expanding size eventually restores crystal symmetry. The figures also reveal that the higher order of hierarchy accentuates the rate of anisotropy ratio. This is due to higher number of smaller hexagons in the structure which introduces greater incremental anisotropy in the crystal structure.

Next, we investigate the propagation of small-amplitude elastic waves in a first order hierarchical honeycomb with $\gamma_1 = 0.5$ under different levels of applied compressive loads using FE simulations. The numerical analyses include: (i) the stability analysis of the structure [121]; (ii) the non-linear post-buckling analysis of the system [121]; and (iii) the propagation of small-amplitude elastic waves at a given deformation [134, 147]. The 2D FE models were constructed using beam elements (hybrid element type B22H in ABAQUS). We assumed that the 2D phononic crystal is made of a silicon-based rubber (Elite Double 32:Zhermack) represented by an incompressible Neo-Hookean model [148], with $G_s = 0.27\ MPa$, $K_s = 13.4\ MPa$, and $\rho_s = 965$ kg/m^3 [116]. We chose this material to guarantee reversibility under large deformations.

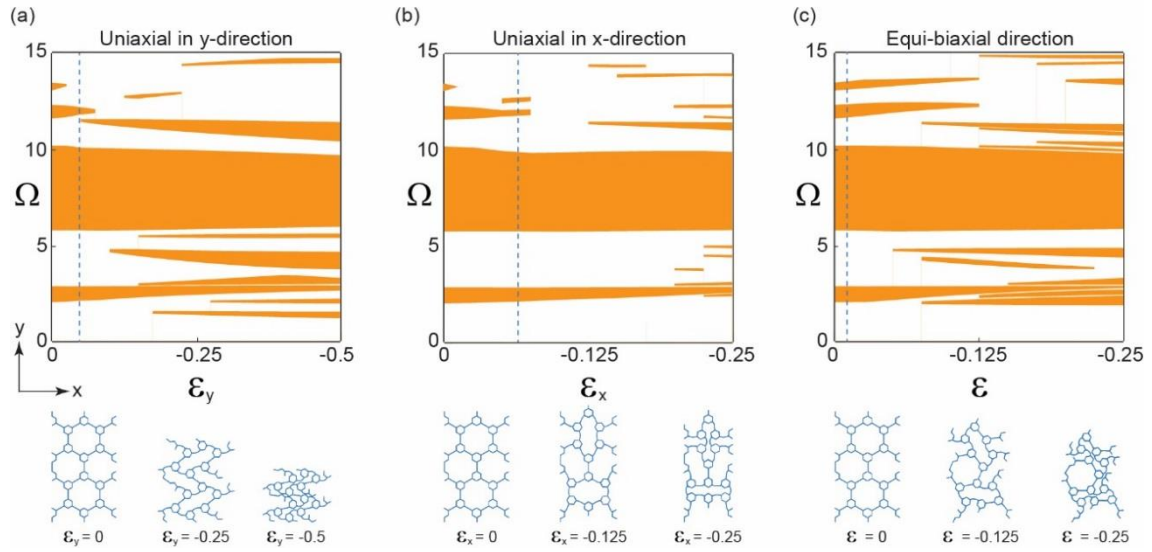

Figure 4.4 The evolution of band gaps as a function of the applied engineering strain for the first order hierarchical honeycomb with $\gamma_1 = 0.5$ subjected to **(a)** uniaxial compression in y-direction, **(b)** uniaxial compression in x-direction, and **(c)** equi-biaxial compression. The dashed vertical lines represent the strain that buckling occurs. The undeformed and deformed configurations of the RVEs at different levels of applied strain are shown at the bottom.

Using this model, we calculate the dispersion relations for both undeformed and deformed configurations [137, 147] (see **Appendices** for more details). We report the normalized frequency (Ω) as a function of applied engineering strain (ε) in **Figure 4.4 (a)** for uniaxial compression in *y*-direction, **Figure 4.4 (b)** for uniaxial compression in *x*-direction, and **Figure 4.4 (c)** for equi-biaxial compression. Note that the structure was compressed in all the directions up to the limit where the beams begin to contact one another. The dynamic response of the structure is characterized with four band gaps at the undeformed configuration in the given range of frequency ($0 \leq \Omega \leq 15$). While the widest band gap at $\Omega = 5.77 - 10.22$ remains almost unchanged during the entire range of applied strain, the other three band gaps are significantly altered upon compression in all the directions. The lowest frequency band gap narrows and shifts to higher frequencies whereas the other two high frequency band gaps completely close around the buckling point and at $\varepsilon = -0.125$, respectively for uniaxial and equi-biaxial compressive loads. Furthermore, once buckling occurs (highlighted with dashed vertical lines), by increasing the level of deformation, several new band gaps open up at different levels of compression,

which most of them remain open, up to the highest level of applied deformation. The results reported in **Figure 4.4 (c)** clearly indicate that equi-biaxial compression opens more band gaps, a signature of higher band gap tunability (compared to other loading directions).

Moreover, the corresponding deformation mode shapes of the representative volume element (RVE) at different levels of applied strains were shown in **Figure 4.4**. The results clearly show the emergence of distinct pattern transformations upon loading in different directions, induced by buckling of the individual beams. Since the pattern transformation is reversible, repeatable, and scale-independent, our results provide new insights into designing tunable materials and devices over a wide range of length scales.

4.4 Conclusions

In summary, our computational study, which investigates the influence of structural hierarchy and imposed deformations on band structure of self-similar hierarchical honeycombs provides new insights on the critical role of hierarchy on dynamic response of phononic crystals. We found that hierarchy tends to shift the existing band gaps to lower frequencies while opening up new band gaps. Deformation was also demonstrated as another mechanism for opening more number of band gaps in hierarchical structures. This study, therefore, provides useful guidelines for the design of phononic devices with tunable properties [149-151].

4.5 Appendices

4.A Bloch wave theory

In our study, we consider the structure to be infinitely extended in two-dimensional (2D) space. **Figure 4.A.1 (a)** shows the schematic of the primitive unit cell and the lattice vectors $\mathbf{a}_1$ and $\mathbf{a}_2$ for a second order hierarchical honeycomb. Note that the lattice vectors are the same for all orders of hierarchy and can be expressed as the following:

$$\mathbf{a}_1 = \sqrt{3}\mathrm{l}_0\left(0.5\mathbf{i} + 0.5\sqrt{3}\mathbf{j}\right)$$

$$\mathbf{a}_2 = \sqrt{3}\mathrm{l}_0\left(-0.5\mathbf{i} + 0.5\sqrt{3}\mathbf{j}\right) \qquad (4.A.1)$$

where **i** and **j** are the Cartesian unit vectors in the x − y plane. Note that all the vector and matrix quantities in this section are denoted by bold letters. The reciprocal lattice vectors (see **Figure 4.A.1 (b)**) are determined as the following:

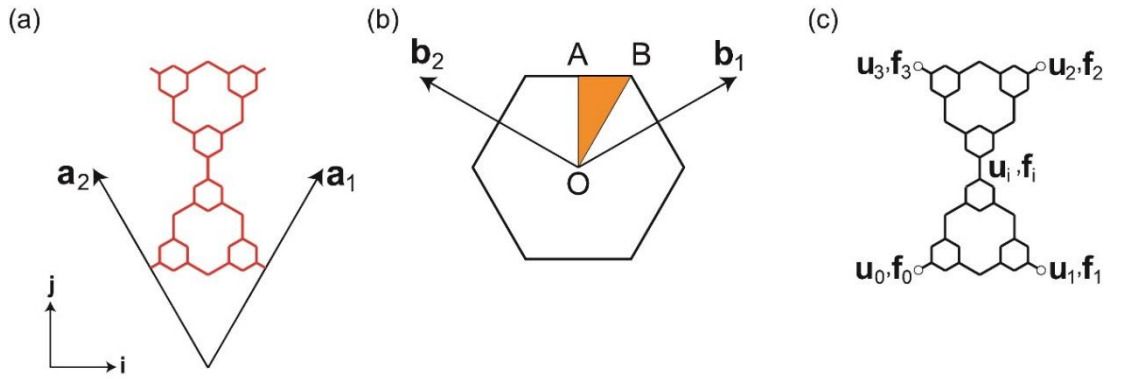

Figure 4.A.1 (a) Schematic of the primitive unit cell and the lattice vectors ($\mathbf{a_1}$ and $\mathbf{a_2}$) of a second order hierarchical honeycomb. **(b)** The reciprocal lattice vectors ($\mathbf{b_1}$ and $\mathbf{b_2}$), first Brillouin zone (hexagonal area), and the irreducible Brillouin zone (shaded triangular area) of the structure. **(c)** Finite element model of the unit cell.

$$\mathbf{b}_1 = \frac{2\pi}{3\mathrm{l}_0}\left(\sqrt{3}\mathbf{i} + \mathbf{j}\right)$$

$$\mathbf{b}_2 = \frac{2\pi}{3\mathrm{l}_0}\left(-\sqrt{3}\mathbf{i} + \mathbf{j}\right) \qquad (4.A.2)$$

Figure 4.A.1 (b) shows the first Brillouin zone (hexagonal region) corresponding to the hierarchical structure. It has been shown that the reflectional and rotational symmetries of the structure can further reduce the region to what referred as the irreducible Brillouin zone (IBZ) which for the hierarchical honeycomb is shown in **Figure 4.A.1 (b)** as a shaded triangular region (OAB). Furthermore, we can restrict the analysis to the wave vectors whose origins are located at the center of the first Brillouin zone (O) with their tips located on the perimeter of the IBZ (O-A-B-O).

4.B Finite element formulations

Numerical simulations of the propagation of small-amplitude elastic waves in the structures were performed using Finite Element (FE) method. **Figure 4.A.1 (c)** shows the unit cell of a second order hierarchical honeycomb structure used in FE analysis. We model the unit cell as a finite number of rigidly connected beam elements with axial, transverse, and rotational degrees of freedom (DOFs) whose mechanics is governed by Timoshenko beam theory [152]. A mesh sensitivity analysis was performed to ensure that the results are not dependent on the mesh size.

The FE form of unit cell's equation of motion can be expressed as:

$$(\mathbf{K} - \omega^2\mathbf{M})\mathbf{u} = \mathbf{f} \tag{4.B.1}$$

where ω is the wave frequency, **K** and **M** are the global stiffness and mass matrices of the unit cell, and, **u** and **f** are the vectors containing generalized nodal displacements and forces defined as the following:

$$\mathbf{u} = \{\mathbf{u}_0 \ \mathbf{u}_1 \ \mathbf{u}_2 \ \mathbf{u}_3 \ \mathbf{u}_i\}^T$$
$$\mathbf{f} = \{\mathbf{f}_0 \ \mathbf{f}_1 \ \mathbf{f}_2 \ \mathbf{f}_3 \ \mathbf{f}_i\}^T \tag{4.B.2}$$

where the subscripts 0, 1, 2, and 3 denote the boundary nodes of the unit cell in contact with the adjacent cells, while the subscript i denote the internal nodes (see **Figure 4.A.1 (c)**). By virtue of Bloch theorem, the following periodic boundary conditions are obtained for the boundary nodes:

$$\mathbf{u}_2 = e^{ik_1}\mathbf{u}_0$$
$$\mathbf{u}_3 = e^{ik_2}\mathbf{u}_1 \tag{4.B.3}$$

and

$$\mathbf{f}_2 = -e^{ik_1}\mathbf{f}_0$$
$$\mathbf{f}_3 = -e^{ik_2}\mathbf{f}_1 \tag{4.B.4}$$

Using **Equation (4.B.3)**, one can define the following transformation:

$$\mathbf{u} = \mathbf{T}\mathbf{u}_r \tag{4.B.5}$$

where $\mathbf{u}_r = \{\mathbf{u}_0 \ \ \mathbf{u}_1 \ \ \mathbf{u}_i\}^T$ is the nodal displacements in the Bloch reduced coordinates, and $\mathbf{T}$ is a transformation matrix obtained as the following:

$$\mathbf{T} = \begin{bmatrix} \mathbf{I} & \mathbf{0} & \mathbf{0} \\ \mathbf{0} & \mathbf{I} & \mathbf{0} \\ \mathbf{I}e^{ik_1} & \mathbf{0} & \mathbf{0} \\ \mathbf{0} & \mathbf{I}e^{ik_2} & \mathbf{0} \\ \mathbf{0} & \mathbf{0} & \mathbf{I} \end{bmatrix} \tag{4.B.6}$$

Now, substituting **Equation (4.B.5)** into **Equation (4.B.1)** and pre-multiplying the resulting equation by $\mathbf{T}^H$, with $()^H$ denoting the Hermitian transpose, yields:

$$[\mathbf{K}_r(k_1, k_2) - \omega^2\mathbf{M}_r(k_1, k_2)]\mathbf{u}_r = \mathbf{0} \tag{4.B.7}$$

where $\mathbf{K}_r(k_1, k_2)$ and $\mathbf{M}_r(k_1, k_2)$ denote the reduced stiffness and mass matrices. **Equation (4.B.7)** is the equation of motion for free wave propagation which constitutes an eigenvalue problem whose solution expresses the dispersion characteristics of the periodic lattice. Wavenumbers k_1 and k_2, which for the wave propagation without attenuation are taken to be real quantities, vary within the first Brillouin zone. The solutions obtained for all possible values of k_1 and k_2 within the first Brillouin zone define the dispersion surfaces of the lattice. The number of dispersion surfaces corresponds to the number of reduced DOFs in the eigenvalue problem.

4.C Numerical implementations

Matlab® (Mathworks Inc., Natick, MA) was employed to develop a FE code to investigate the propagation of small-amplitude elastic waves in the proposed hierarchical honeycomb structure. Beams were assumed to have a rectangular cross section with unit length normal to the plane of wave motion and the thickness was adjusted to be consistent with the value of the relative density of the structure. Mesh convergence study was also performed in order to remove any mesh dependence on final results. Linear elastic properties of

aluminum were assumed for the cell wall material with $E_s = 71\text{GPa}$, $\nu_s = 0.33$, and $\rho_s = 2700\,\text{kg/m}^3$. In all the simulations in this study, the relative density is kept constant at 8%.

We basically solved the eigenvalue problem given in **Equation (4.B.7)** to obtain the dispersion relations $\omega = \omega(\mathbf{k})$ for $\mathbf{k}$ vectors varying on the perimeter of the IBZ. Then the band gaps were identified by the frequency ranges in which no solution exists for $\omega(\mathbf{k})$. At least fifty uniformly spaced points on each edge of the IBZ were used for band gap calculations. For convenience, the wave propagation frequency is normalized with respect to the first flexural frequency of a simply supported beam with length l_0 and thickness t_0, that is $\Omega = \omega/\omega_0$, where $\omega_0 = \pi^2\sqrt{E_s {t_0}^2/\left(12\rho_s {l_0}^4\right)}$ [138].

4.D Additional results for low frequency directionality

Note that the first and second modes of the propagating waves respectively represent shear- and pressure-dominated modes of propagation. The phase velocity $\mathbf{V}_p$ and group velocity $\mathbf{V}_g$ of the propagating waves can be calculated using the following relations:

$$\mathbf{V}_p = \frac{\omega\mathbf{k}}{\|\mathbf{k}\|^2}$$

$$\mathbf{V}_g = \frac{\partial\omega}{\partial\mathbf{k}} \tag{4.D.1}$$

At least four hundred uniformly spaced points inside the IBZ were used to interpolate the dispersion surface in $\mathbf{k}$ space.

Here, we first report phase and group velocity profiles for all directions of wave motion at $\Omega = 0.1$ for the lowest two modes of propagating waves. **Figures 4.D.1**, **4.D.2**, **4.D.3**, and **4.D.4** respectively present the phase and group velocity profiles for the first and second modes of propagating waves. The results are presented for six different values of η (i.e., self-similarity ratio, defined in the manuscript) for self-similar hierarchical honeycombs up to third order of hierarchy. We employed the data extracted from these

profiles to plot the evolution of anisotropy ratio against self-similarity ratio depicted in **Figure 4.3 (d)** in the manuscript. The results clearly indicate that the directionality of propagating waves at low frequency regimes is extremely dependent to the topology of the structure (i.e., the hierarchical order and self-similarity ratio). Then, the topology of the structure can be used as a design parameter to tune the directionality characteristics of the structure at low frequency regimes.

Next, we report in **Figures 4.D.5 - 4.D.10** the contour plots of dispersion surfaces for the first (S-mode) and second (L-mode) modes of propagation. The results are presented for six different values of self-similarity ratio for self-similar hierarchical honeycombs up to third order of hierarchy. Note that ξ_1 and ξ_2 are the components of the wave vector along the Cartesian unit vectors in the $x-y$ plane, that is $\mathbf{k} = k_1\mathbf{b}_1 + k_2\mathbf{b}_2 = \xi_1\mathbf{i} + \xi_2\mathbf{j}$. The results again confirm the dependency of directionality of propagating waves at low frequency regimes to the topology of the structure.

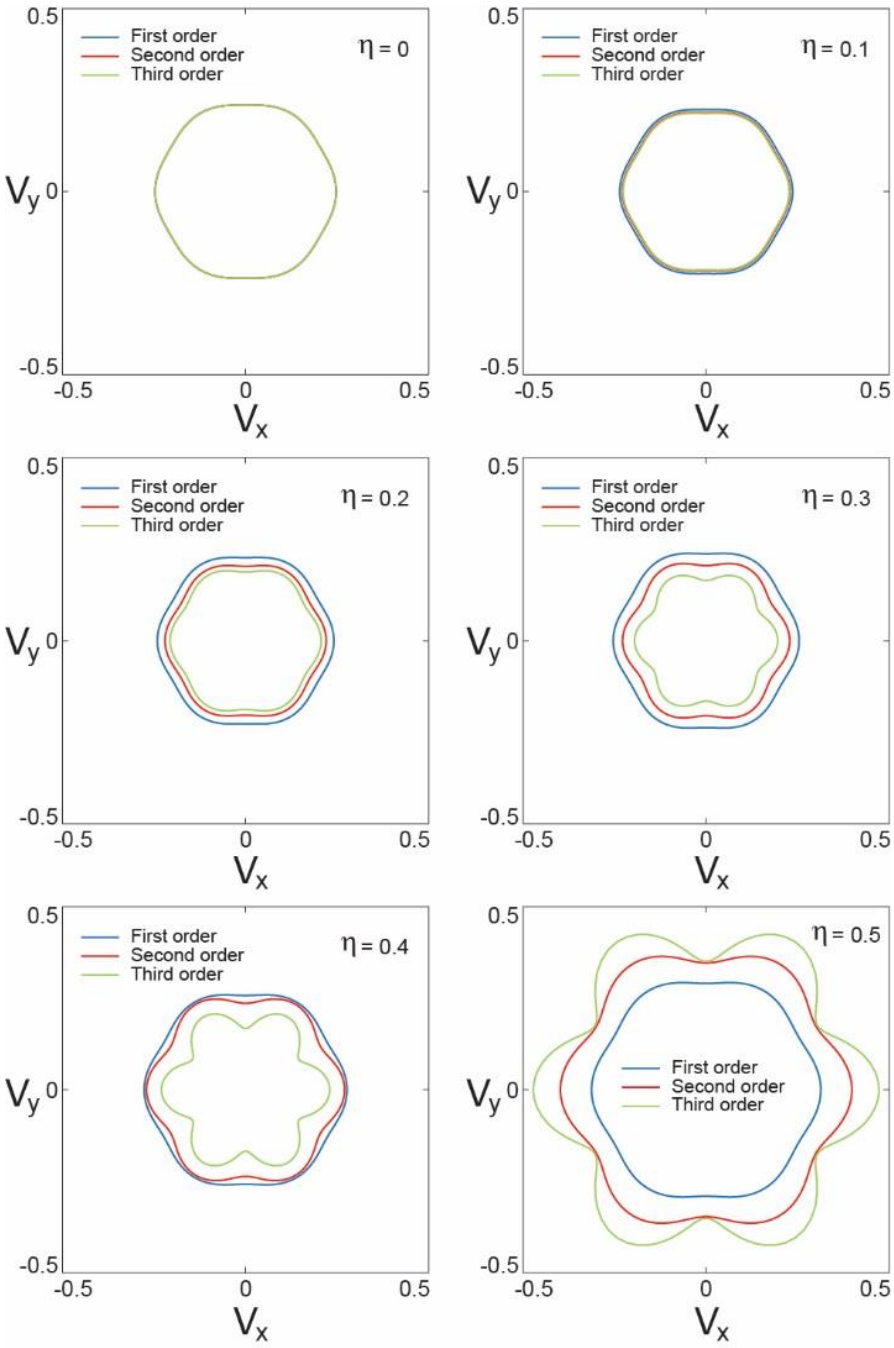

Figure 4.D.1 Phase velocity profiles for the first mode of wave propagation. The results are presented for six different values of self-similarity ratio for self-similar hierarchical honeycombs up to third order of hierarchy.

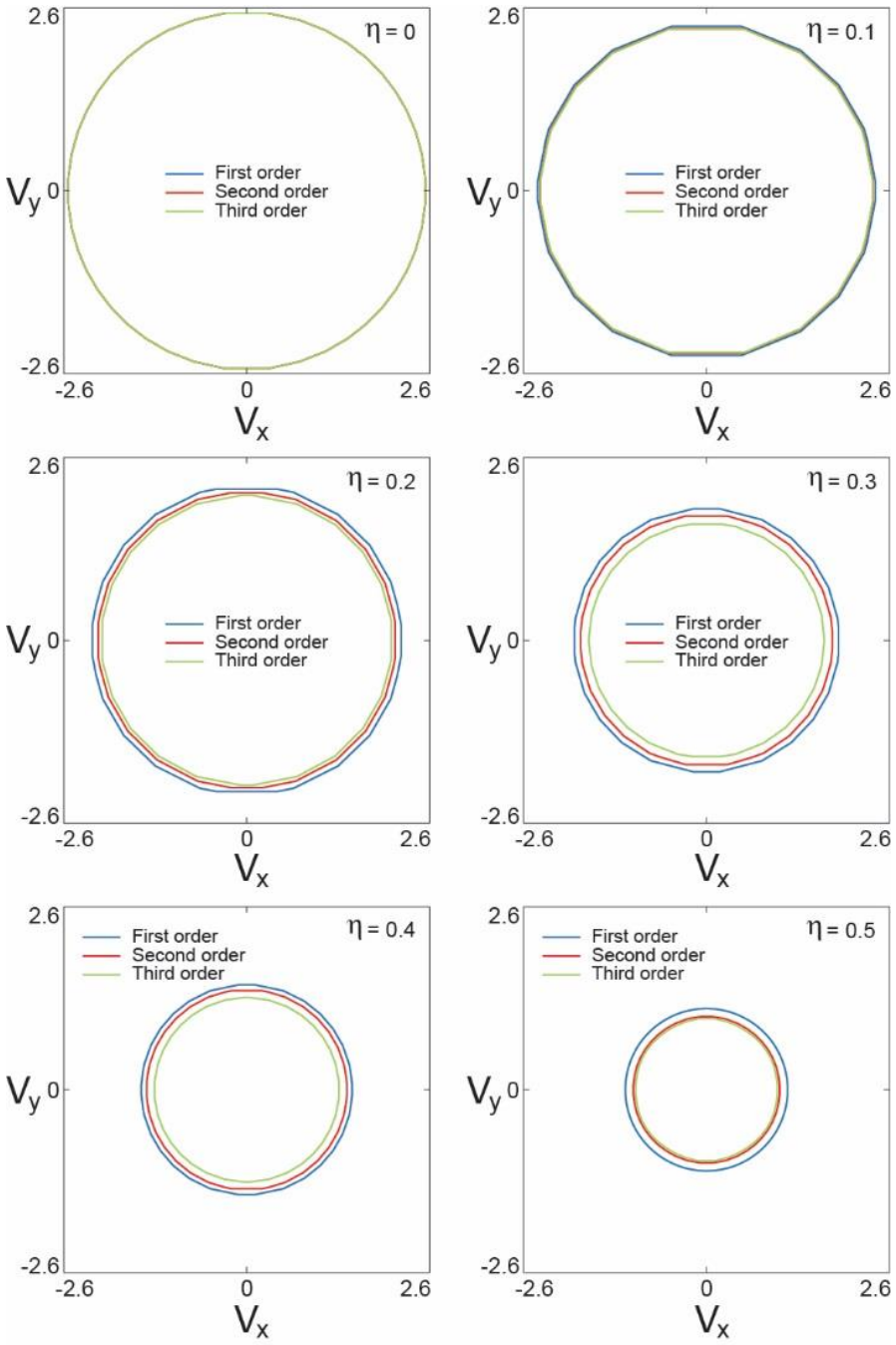

Figure 4.D.2 Phase velocity profiles for the second mode of wave propagation. The results are presented for six different values of self-similarity ratio for self-similar hierarchical honeycombs up to third order of hierarchy.

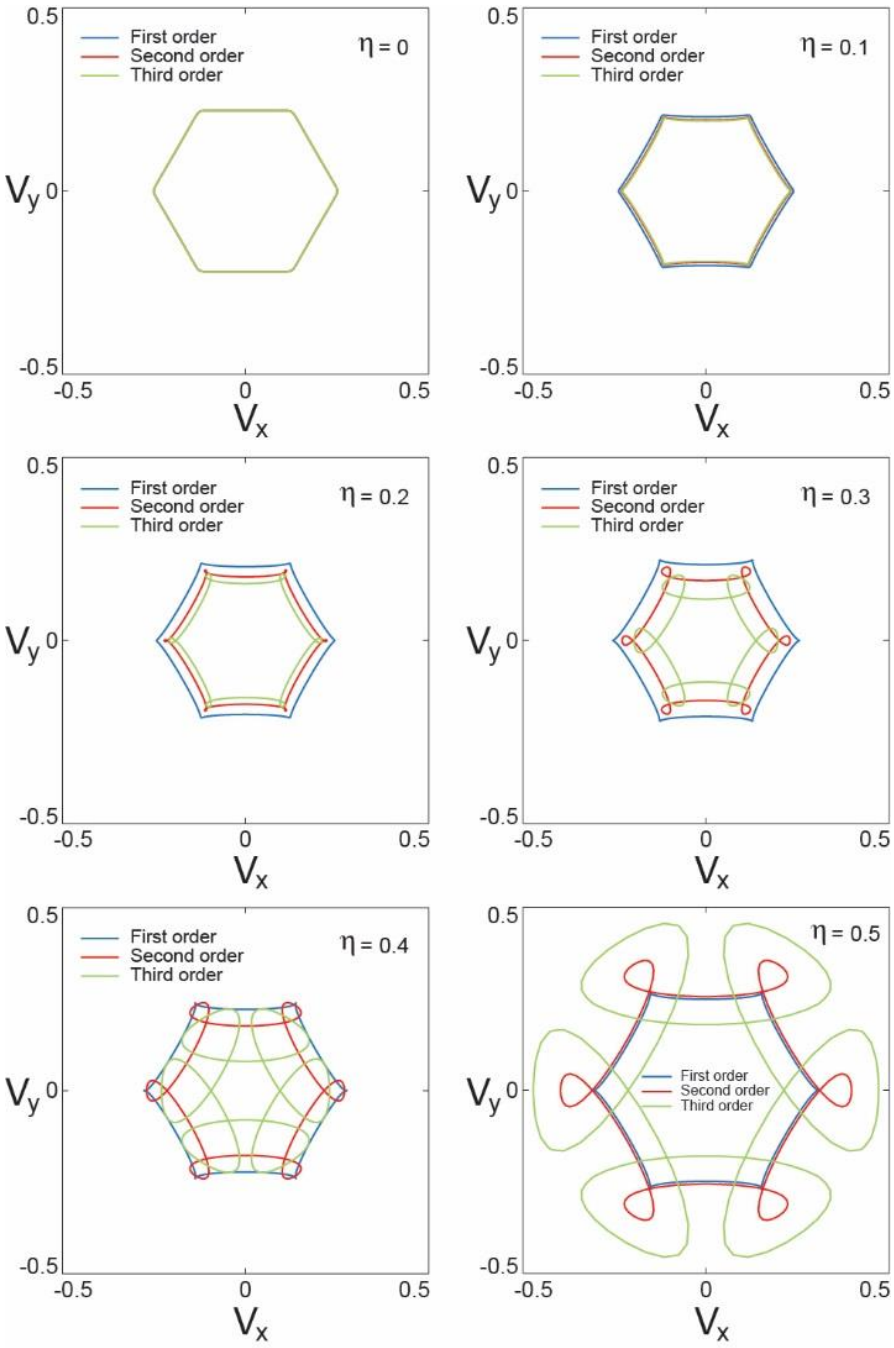

Figure 4.D.3 Group velocity profiles for the first mode of wave propagation. The results are presented for six different values of self-similarity ratio for self-similar hierarchical honeycombs up to third order of hierarchy.

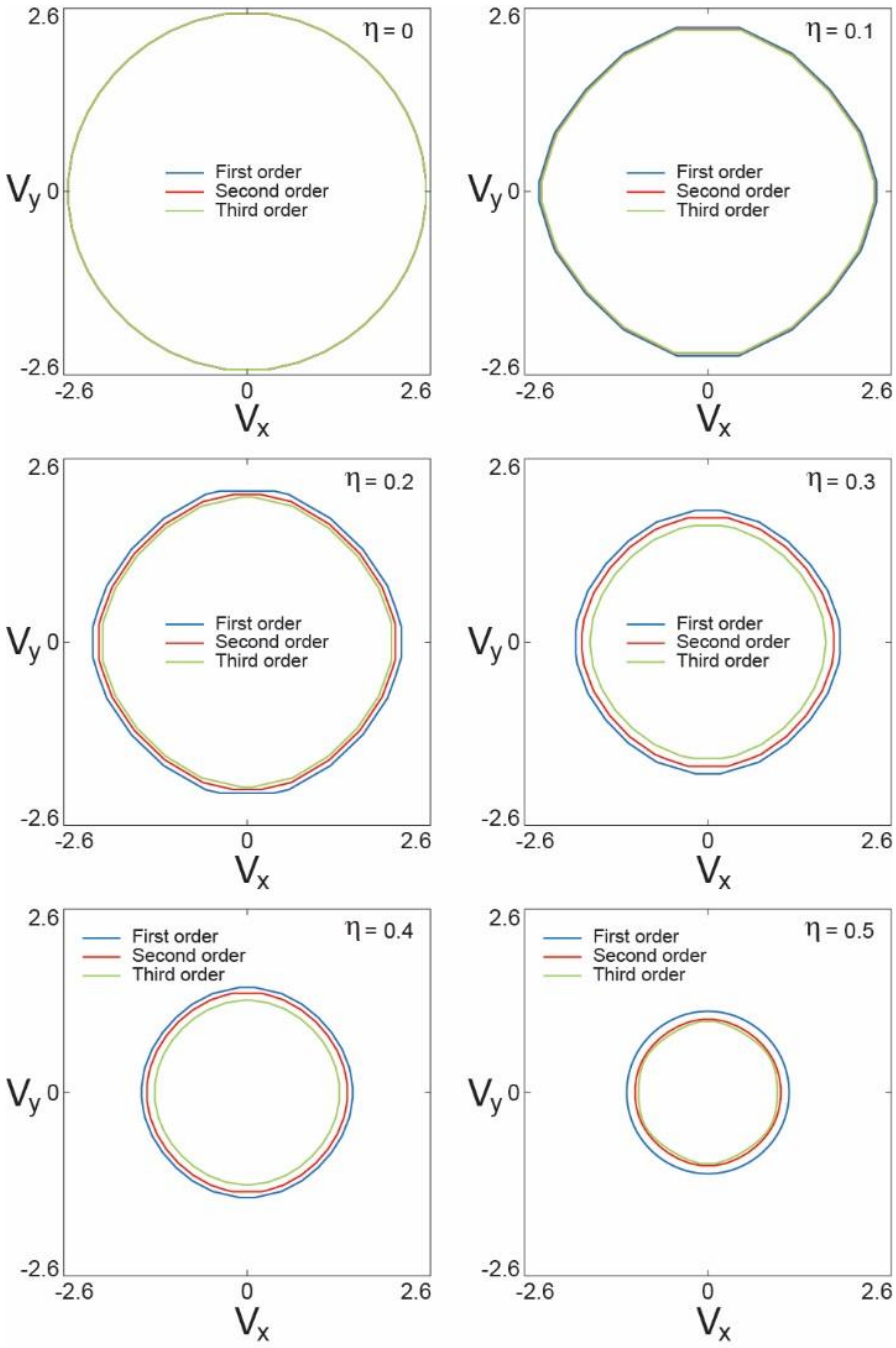

Figure 4.D.4 Group velocity profiles for the second mode of wave propagation. The results are presented for six different values of self-similarity ratio for self-similar hierarchical honeycombs up to third order of hierarchy.

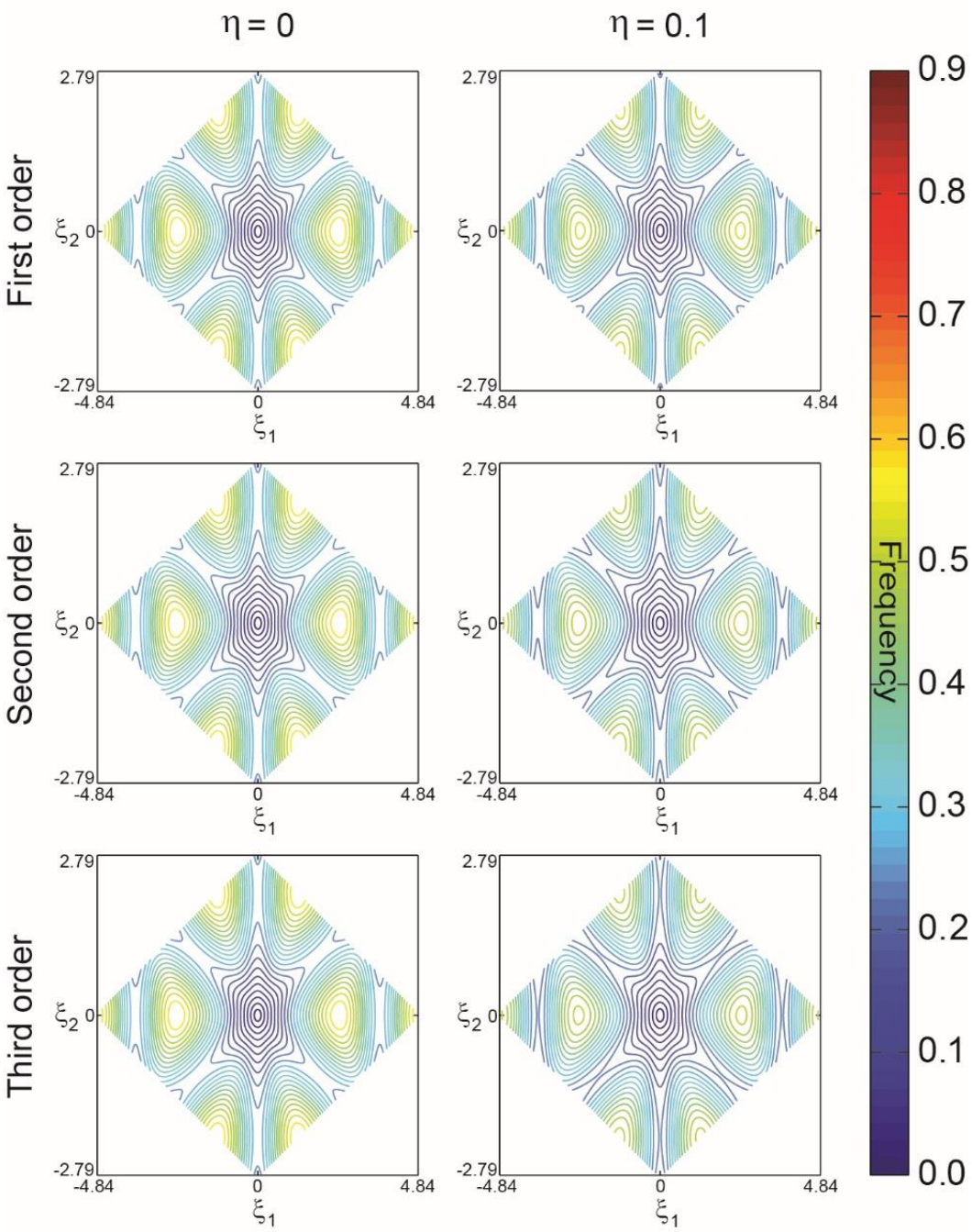

Figure 4.D.5 Iso-frequency plots of the first mode of wave propagation. The results are presented for six different values of self-similarity ratio for self-similar hierarchical honeycombs up to third order of hierarchy.

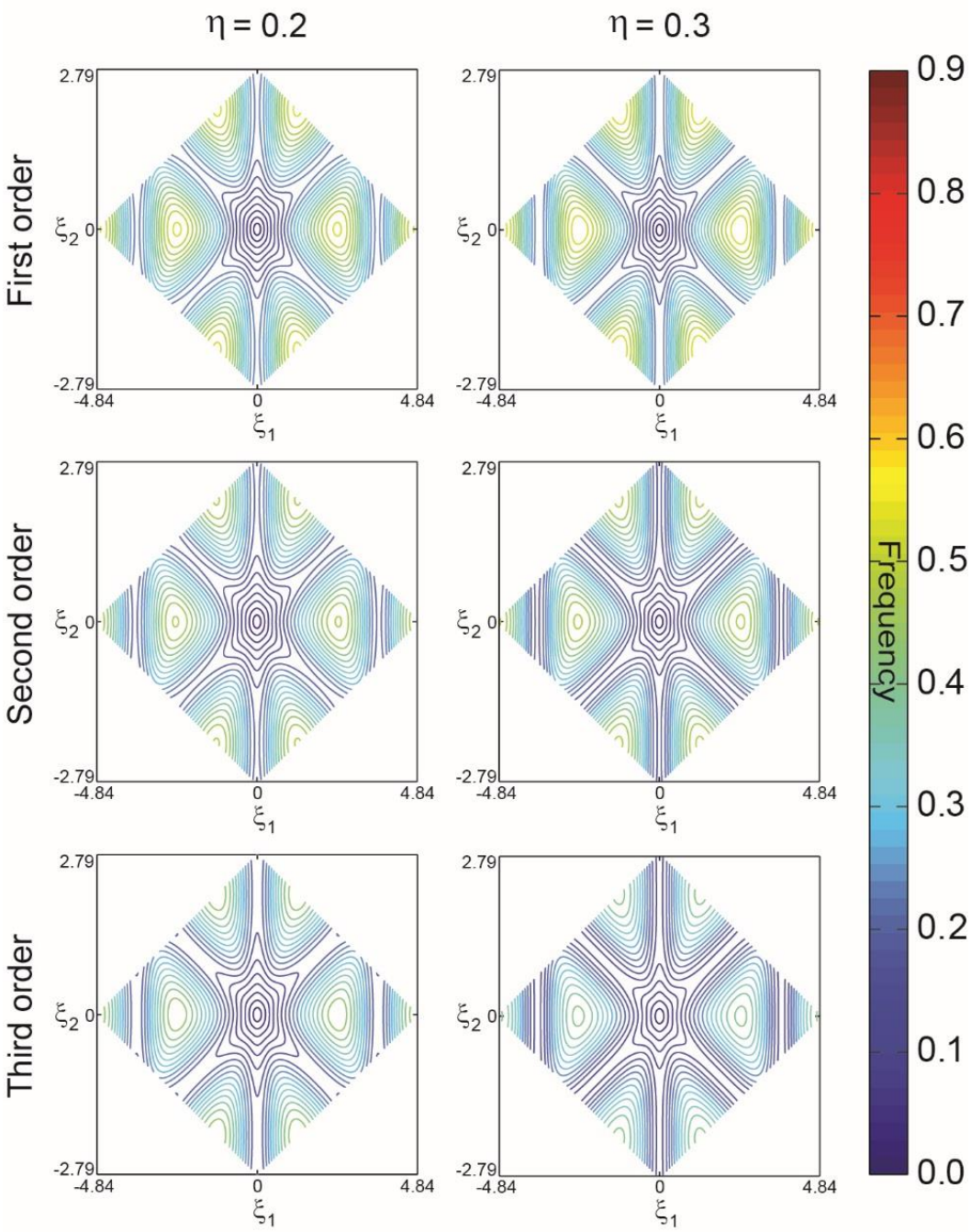

Figure 4.D.6 Iso-frequency plots of the first mode of wave propagation. The results are presented for six different values of self-similarity ratio for self-similar hierarchical honeycombs up to third order of hierarchy.

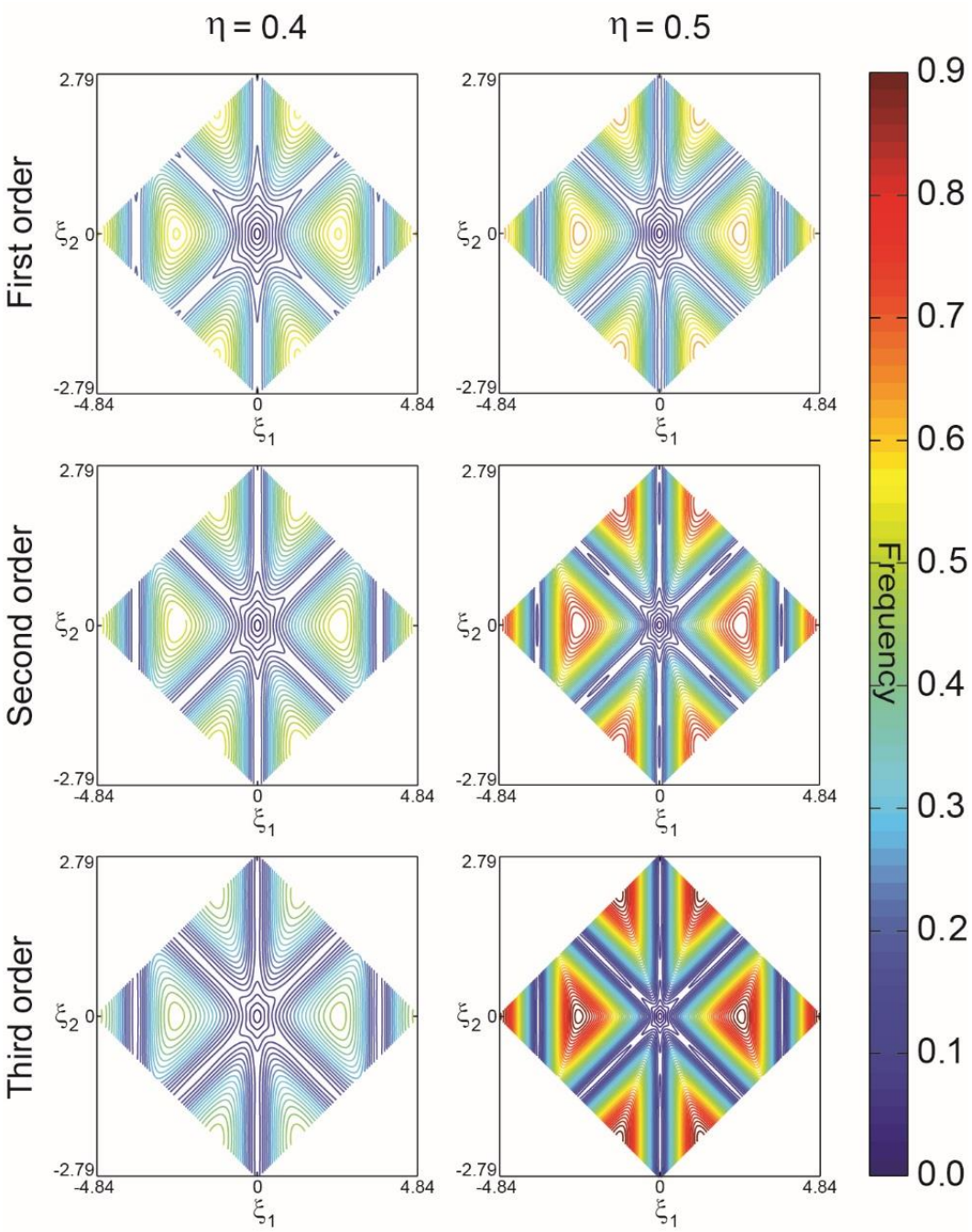

Figure 4.D.7 Iso-frequency plots of the first mode of wave propagation. The results are presented for six different values of self-similarity ratio for self-similar hierarchical honeycombs up to third order of hierarchy.

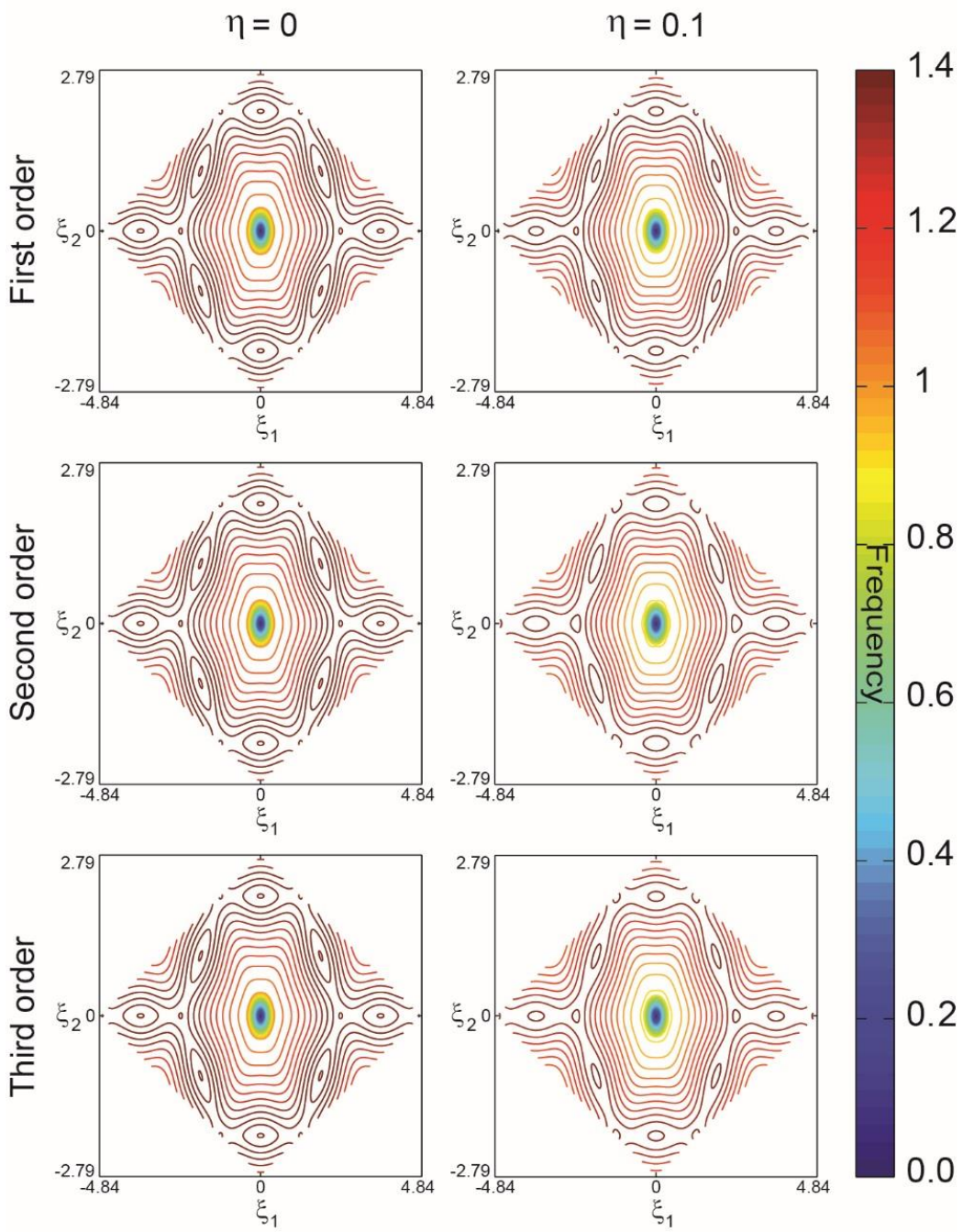

Figure 4.D.8 Iso-frequency plots of the second mode of wave propagation. The results are presented for six different values of self-similarity ratio for self-similar hierarchical honeycombs up to third order of hierarchy.

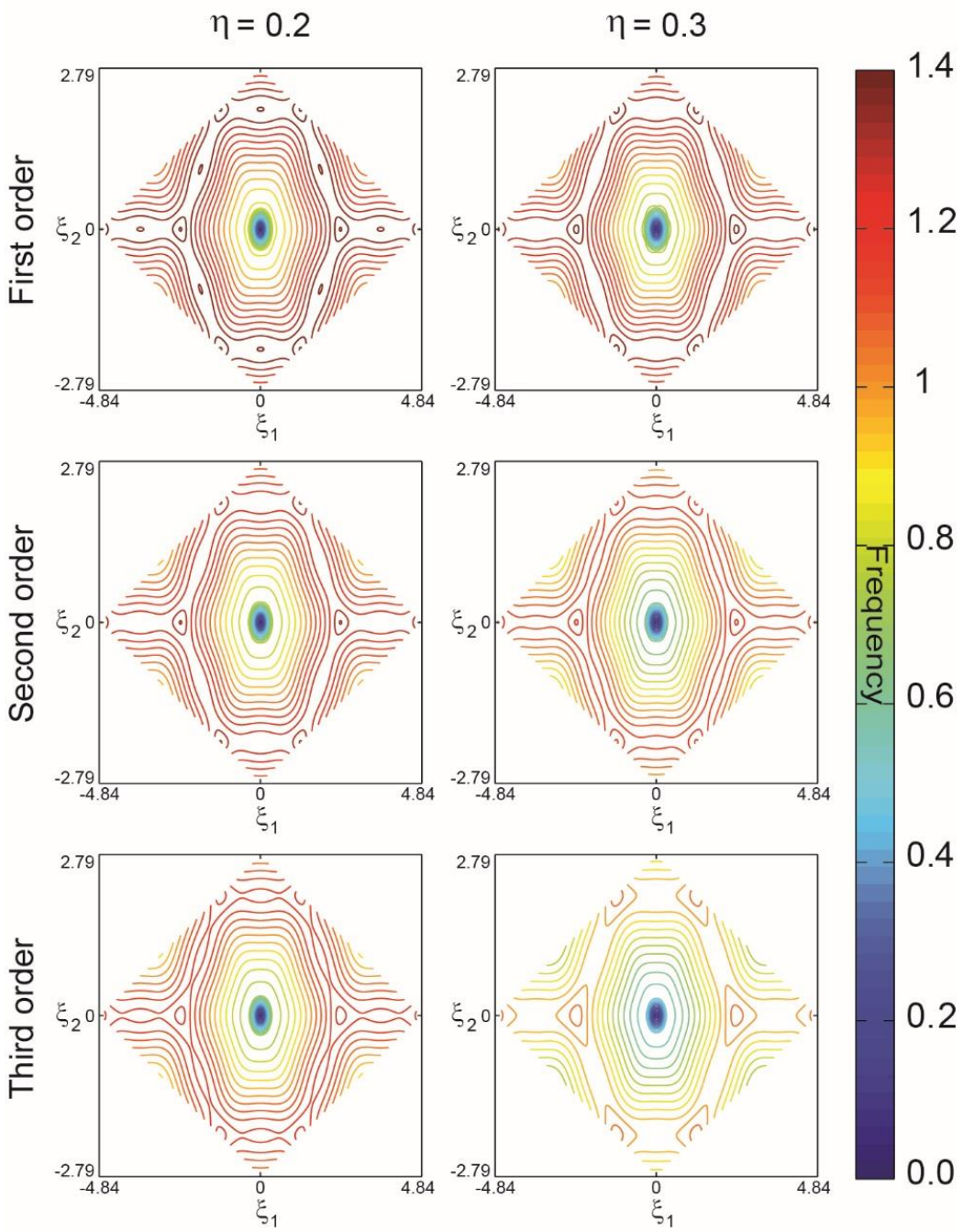

Figure 4.D.9 Iso-frequency plots of the second mode of wave propagation. The results are presented for six different values of self-similarity ratio for self-similar hierarchical honeycombs up to third order of hierarchy.

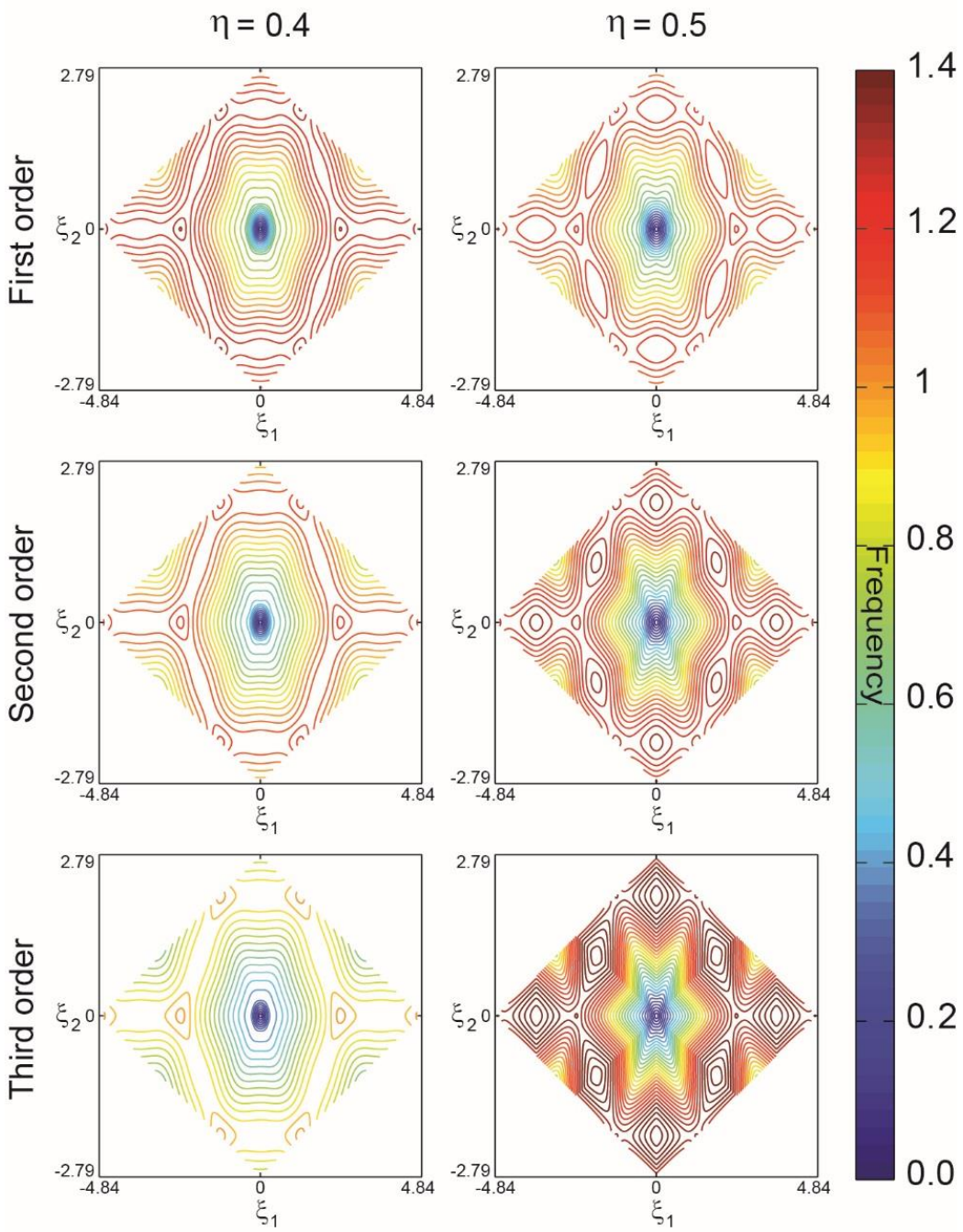

Figure 4.D.10 Iso-frequency plots of the second mode of wave propagation. The results are presented for six different values of self-similarity ratio for self-similar hierarchical honeycombs up to third order of hierarchy.

4.E Effect of deformation - wave propagation analysis

We investigated the propagation of small-amplitude elastic waves in an elastomeric deformable hierarchical honeycomb with $\gamma_1 = 0.5$ under different levels of applied compression in *x*-, *y*-, and biaxial directions. In order to obtain the dispersion relation, $\omega = \omega(k)$, frequency domain wave propagation analysis was conducted on both the undeformed and deformed configurations generated by the post-buckling analysis using commercial FE package ABAQUS/Standard [153, 154].

In this section, for the sake of simplicity in numerical calculations, we considered a rectangular unit cell, and we performed the simulations on the enlarged unit cell assuming Bloch type boundary conditions which is implemented using a user defined multiple point constraint (MPC) subroutine [134, 153, 154]. In the band diagrams presented in **Figures 4.E.2**, **4.E.3**, and **4.E.4**, the normalized frequency (Ω) was calculated for all k vectors along the perimeter and the diagonal of the IBZ in reciprocal lattice space (see path G − X − M − G − Y – M in **Figure 4.E.1**). We used 20 uniformly spaced k points on each line segment (e.g. G − X), that they were updated at every levels of deformation [155].

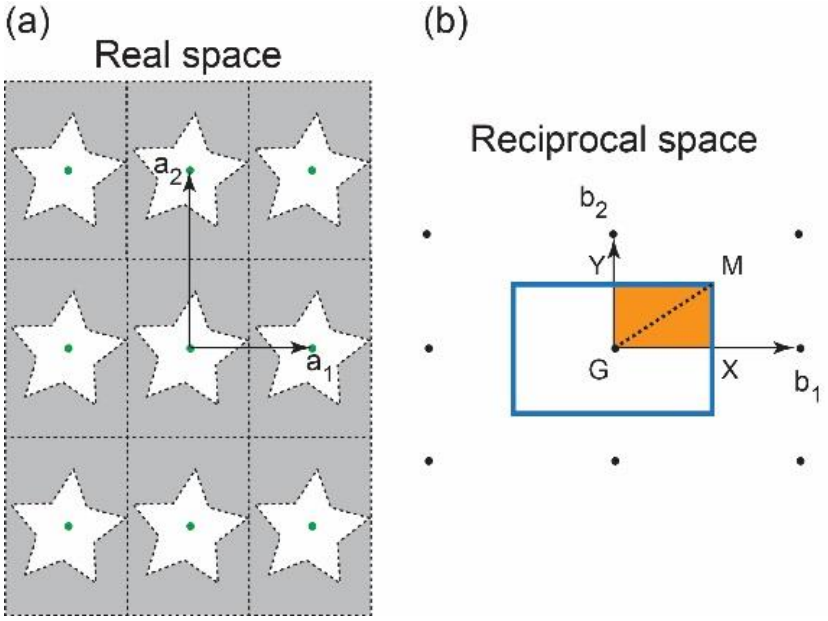

Figure 4.E.1 Schematic of a 2D point lattice in **(a)** real space (green dots), and **(b)** reciprocal space (black dots). The unit cell spanned by lattice vectors a_1 and a_2 is shown in grey. The first Brillioun zone (blue rectangle area) and the irreducible Brillioun zone (orange area GXMYM) are shown in (b).

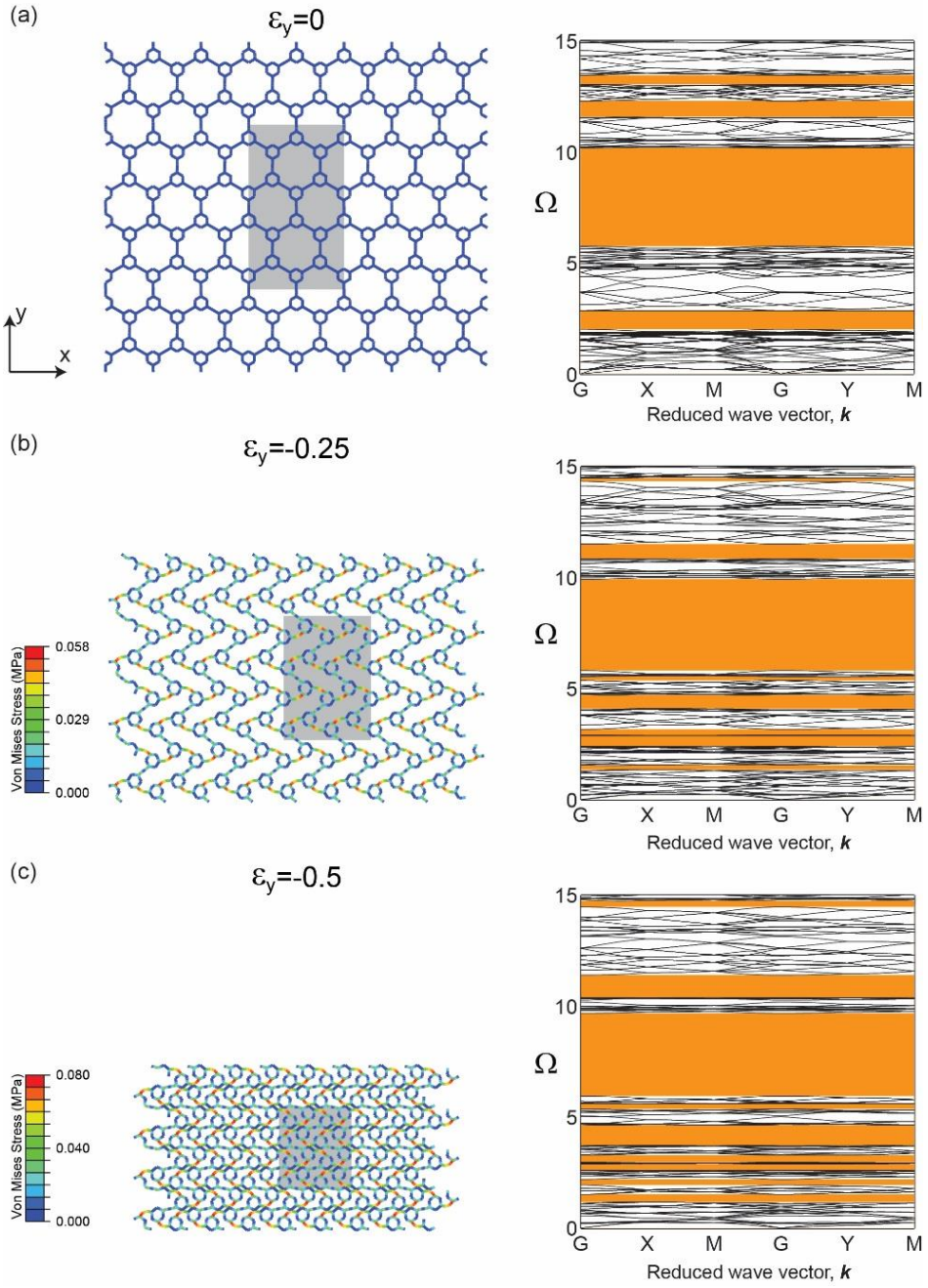

Figure 4.E.2 Effect of the applied compression in y-direction on propagation of elastic waves. The band diagrams and corresponding deformed structures are presented at three different levels of applied deformation. The contour plot on the deformed structures represents the von Mises stress distribution (unit:MPa), and the dark grey area shows the RVE during the pattern transformation.

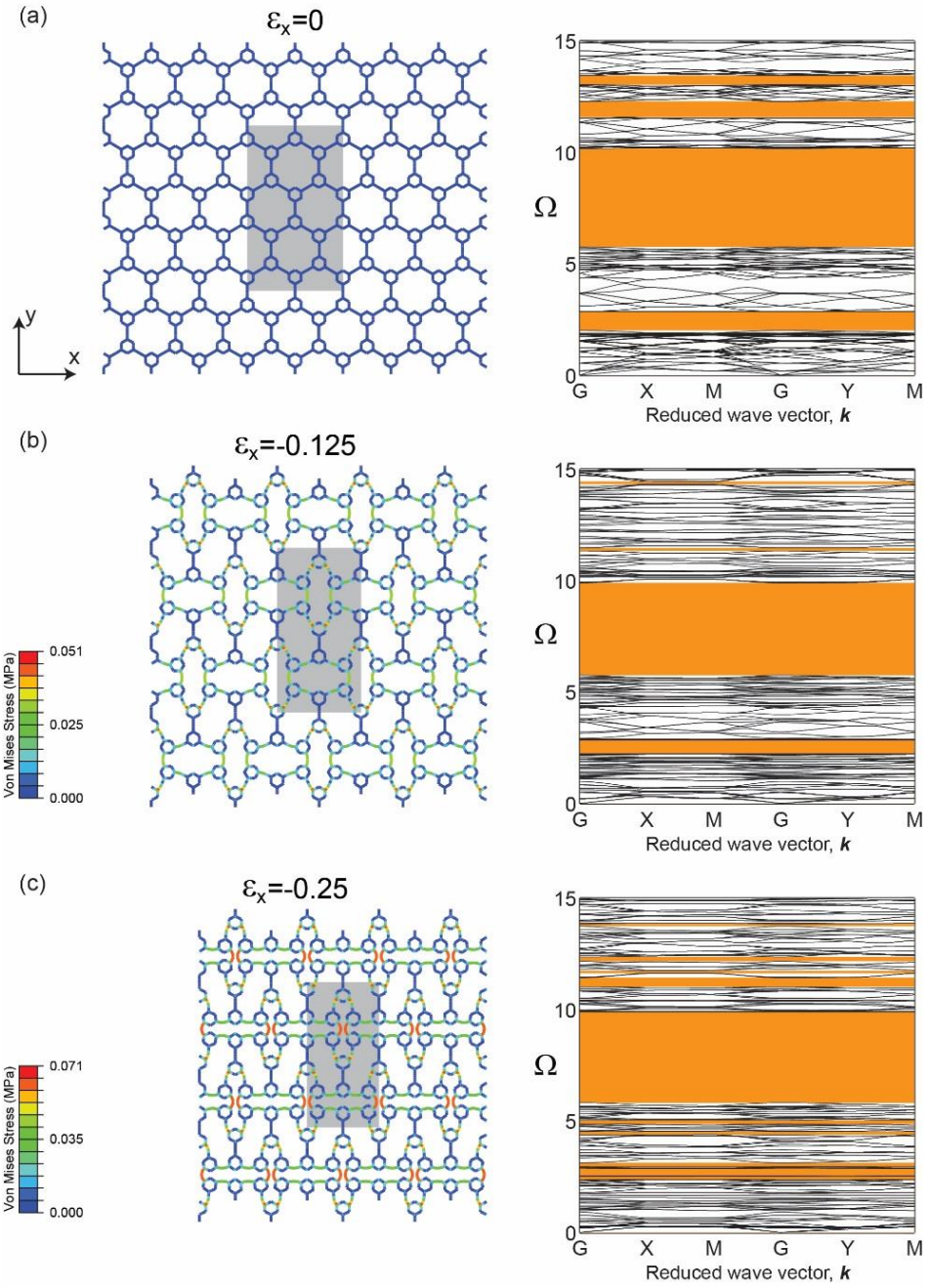

Figure 4.E.3 Effect of the applied compression in x-direction on propagation of elastic waves. The band diagrams and corresponding deformed structures are presented at three different levels of applied deformation. The contour plot on the deformed structures represents the von Mises stress distribution (unit:MPa), and the dark grey area shows the RVE during the pattern transformation.

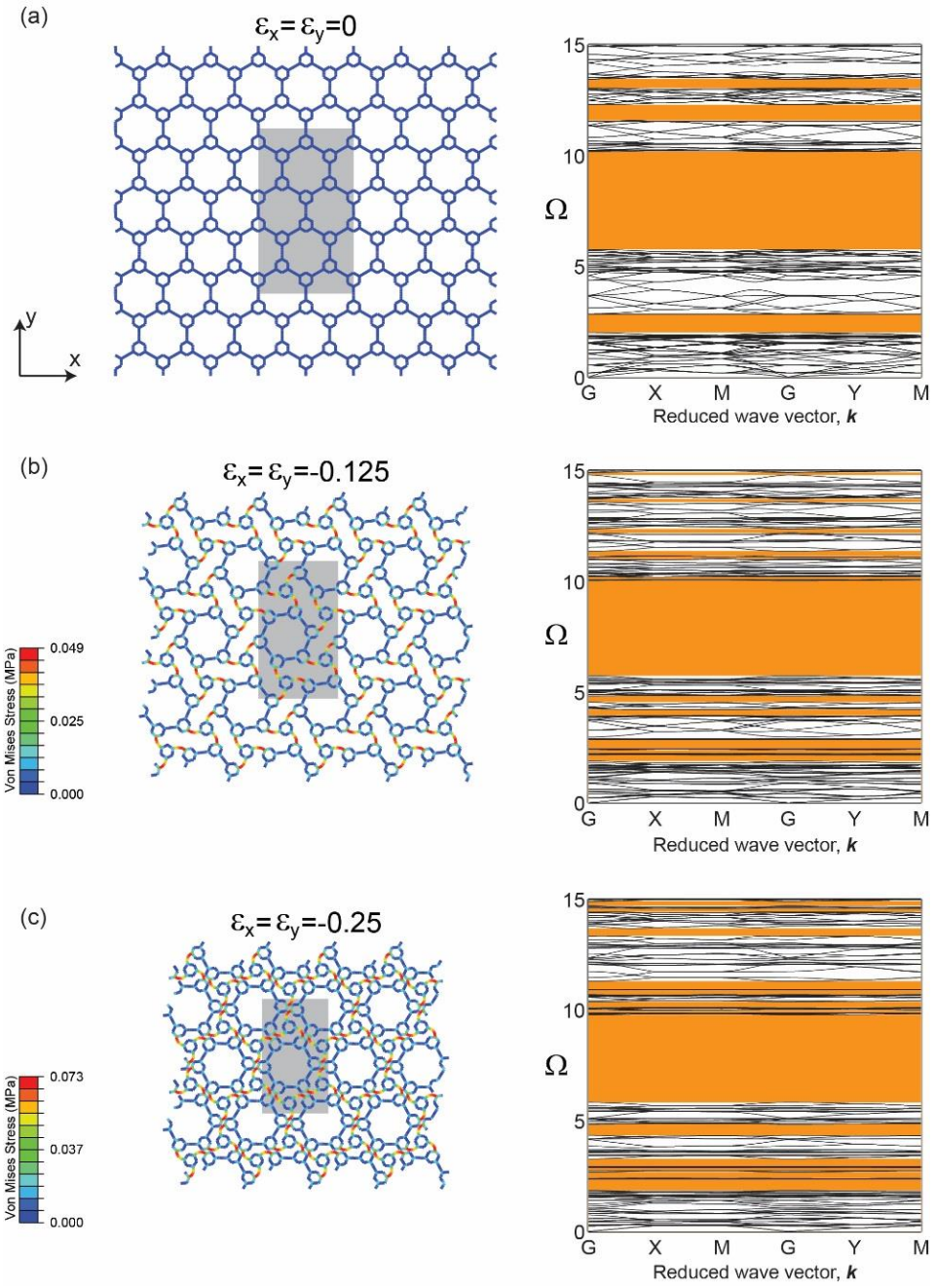

Figure 4.E.4 Effect of the applied eqi-biaxial compression on propagation of elastic waves. The band diagrams and corresponding deformed structures are presented at three different levels of applied deformation. The contour plot on the deformed structures represents the von Mises stress distribution (unit:MPa), and the dark grey area shows the RVE during the pattern transformation.

References

[1] S. Lubkin, Unidirectional waves on rings: Models for chiral preference of circumnutating plants, Bulletin of Mathematical Biology, 56 (1994) 795-810.

[2] M. Oliverio, M.C. Digilio, P. Versacci, B. Dallapiccola, B. Marino, Shells and heart: Are human laterality and chirality of snails controlled by the same maternal genes?, American Journal of Medical Genetics Part A, 152A (2010) 2419-2425.

[3] M. Schilthuizen, A. Davison, The convoluted evolution of snail chirality, Naturwissenschaften, 92 (2005) 504-515.

[4] R.R. Sinden, DNA Structure and Function, Gulf Professional Publishing, 1994.

[5] Z.-L. Zhao, B. Li, X.-Q. Feng, Handedness-dependent hyperelasticity of biological soft fibers with multilayered helical structures, International Journal of Non-Linear Mechanics, 81 (2016) 19-29.

[6] J. Aizenberg, J.C. Weaver, M.S. Thanawala, V.C. Sundar, D.E. Morse, P. Fratzl, Skeleton of Euplectella sp.: Structural Hierarchy from the Nanoscale to the Macroscale, Science, 309 (2005) 275-278.

[7] M.J. Buehler, Nature designs tough collagen: Explaining the nanostructure of collagen fibrils, Proceedings of the National Academy of Sciences, 103 (2006) 12285-12290.

[8] H.D. Espinosa, A.L. Juster, F.J. Latourte, O.Y. Loh, D. Gregoire, P.D. Zavattieri, Tablet-level origin of toughening in abalone shells and translation to synthetic composite materials, Nat Commun, 2 (2011) 173.

[9] P. Fratzl, R. Weinkamer, Nature's hierarchical materials, Progress in Materials Science, 52 (2007) 1263-1334.

[10] L.J. Gibson, M.F. Ashby, B.A. Harley, Cellular materials in nature and medicine, Cambridge University Press, 2010.

[11] R. Lakes, Materials with structural hierarchy, Nature, 361 (1993) 511-515.

[12] C. Ortiz, M.C. Boyce, Bioinspired Structural Materials, Science, 319 (2008) 1053-1054.

[13] H. Qing, L. Mishnaevsky Jr, 3D hierarchical computational model of wood as a cellular material with fibril reinforced, heterogeneous multiple layers, Mechanics of Materials, 41 (2009) 1034-1049.

[14] J.-S. Wang, G. Wang, X.-Q. Feng, T. Kitamura, Y.-L. Kang, S.-W. Yu, Q.-H. Qin, Hierarchical chirality transfer in the growth of Towel Gourd tendrils, Scientific reports, 3 (2013).

[15] Z.-L. Zhao, H.-P. Zhao, J.-S. Wang, Z. Zhang, X.-Q. Feng, Mechanical properties of carbon nanotube ropes with hierarchical helical structures, Journal of the Mechanics and Physics of Solids, 71 (2014) 64-83.

[16] N. Fang, D. Xi, J. Xu, M. Ambati, W. Srituravanich, C. Sun, X. Zhang, Ultrasonic metamaterials with negative modulus, Nature materials, 5 (2006) 452-456.

[17] Z. Liu, X. Zhang, Y. Mao, Y. Zhu, Z. Yang, C. Chan, P. Sheng, Locally resonant sonic materials, Science, 289 (2000) 1734-1736.

[18] R. Lakes, T. Lee, A. Bersie, Y. Wang, Extreme damping in composite materials with negative-stiffness inclusions, Nature, 410 (2001) 565-567.

[19] U.D. Larsen, O. Sigmund, S. Bouwstra, Design and fabrication of compliant micromechanisms and structures with negative Poisson's ratio, in: Micro Electro Mechanical Systems, 1996, MEMS'96, Proceedings.'An Investigation of Micro Structures, Sensors, Actuators, Machines and Systems'. IEEE, The Ninth Annual International Workshop on, IEEE, 1996, pp. 365-371.

[20] R. Lakes, Foam structures with a negative Poisson's ratio, Science, 235 (1987) 1038-1040.

[21] E. Friis, R. Lakes, J. Park, Negative Poisson's ratio polymeric and metallic foams, Journal of materials science, 23 (1988) 4406-4414.

[22] C. Körner, Y. Liebold-Ribeiro, A systematic approach to identify cellular auxetic materials, Smart Materials and Structures, 24 (2015) 025013.

[23] O. Sigmund, S. Torquato, Design of materials with extreme thermal expansion using a three-phase topology optimization method, Journal of the Mechanics and Physics of Solids, 45 (1997) 1037-1067.

[24] C.A. Steeves, S.L. Dos Santos E Lucato, M. He, E. Antinucci, J.W. Hutchinson, A.G. Evans, Concepts for structurally robust materials that combine low thermal expansion with high stiffness, Journal of the Mechanics and Physics of Solids, 55 (2007) 1803-1822.

[25] O. Sigmund, S. Torquato, Composites with extremal thermal expansion coefficients, Applied Physics Letters, 69 (1996) 3203-3205.

[26] F. Scarpa, Auxetic materials for bioprostheses [In the Spotlight], Signal Processing Magazine, IEEE, 25 (2008) 128-126.

[27] J. Choi, R. Lakes, Design of a fastener based on negative Poisson's ratio foam, Cellular Polymers, 10 (1991) 205-212.

[28] O. Sigmund, S. Torquato, I.A. Aksay, On the design of 1-3 piezocomposites using topology optimization, Journal of Materials Research, 13 (1998) 1038-1048.

[29] K. Evans, K. Alderson, Auxetic materials: the positive side of being negative, Engineering Science and Education Journal, 9 (2000) 148-154.

[30] F. Scarpa, G. Burriesci, F. Smith, B. Chambers, Mechanical and electromagnetic behaviour of auxetic honeycomb structures, Aeronautical Journal, 107 (2003) 175.

[31] F. Scarpa, L. Ciffo, J. Yates, Dynamic properties of high structural integrity auxetic open cell foam, Smart Materials and Structures, 13 (2004) 49.

[32] A. Spadoni, M. Ruzzene, Elasto-static micropolar behavior of a chiral auxetic lattice, Journal of the Mechanics and Physics of Solids, 60 (2012) 156-171.

[33] Y. Chen, F. Scarpa, Y. Liu, J. Leng, Elasticity of anti-tetrachiral anisotropic lattices, International Journal of Solids and Structures, (2012).

[34] O. Levy, S. Krylov, I. Goldfarb, Design considerations for negative Poisson ratio structures under large deflection for MEMS applications, Smart Materials and Structures, 15 (2006) 1459.

[35] R.J. Jackman, S.T. Brittain, A. Adams, M.G. Prentiss, G.M. Whitesides, Design and fabrication of topologically complex, three-dimensional microstructures, Science, 280 (1998) 2089-2091.

[36] G. Lesieutre, J.A. Browne, M. Frecker, Scaling of Performance, Weight, and Actuation of a 2-D Compliant Cellular Frame Structure for a Morphing Wing, Journal of Intelligent Material Systems and Structures, 22 (2011) 979-986.

[37] K.R. Olympio, F. Gandhi, Flexible skins for morphing aircraft using cellular honeycomb cores, Journal of Intelligent Material Systems and Structures, 21 (2010) 1719-1735.

[38] E.A. Bubert, B.K. Woods, K. Lee, C.S. Kothera, N.M. Wereley, Design and fabrication of a passive 1D morphing aircraft skin, Journal of Intelligent Material Systems and Structures, 21 (2010) 1699-1717.

[39] A. Spadoni, M. Ruzzene, Static aeroelastic response of chiral-core airfoils, Journal of Intelligent Material Systems and Structures, 18 (2007) 1067-1075.

[40] H. Heo, J. Ju, D.-M. Kim, C.-S. Jeon, Passive Morphing Airfoil with Honeycombs, in: Proceedings of the ASME International Mechanical Engineering Congress and Exposition, IMECE2011-64350, Denver, CO, 2011.

[41] T. Johnson, M. Frecker, M. Abdalla, Z. Gurdal, D. Lindner, Nonlinear Analysis and Optimization of Diamond Cell Morphing Wings, Journal of Intelligent Material Systems and Structures, 20 (2009) 815-824.

[42] D. Bornengo, F. Scarpa, C. Remillat, Evaluation of hexagonal chiral structure for morphing airfoil concept, Proceedings of the Institution of Mechanical Engineers, Part G: Journal of Aerospace Engineering, 219 (2005) 185-192.

[43] J.L. Reed Jr, C.D. Hemmelgarn, B.M. Pelley, E. Havens, Adaptive wing structures, in: Proc. of SPIE Vol, 2005, pp. 133.

[44] J. Ju, D.-M. Kim, K. Kim, Flexible cellular solid spokes of a non-pneumatic tire, Composite Structures, (2012).

[45] J. Ju, B. Ananthasayanam, J.D. Summers, P. Joseph, Design of Cellular Shear Bands of a Non-Pneumatic Tire-Investigation of Contact Pressure, SAE International Journal of Passenger Cars-Mechanical Systems, 3 (2010) 598-606.

[46] A. Alderson, K. Alderson, D. Attard, K. Evans, R. Gatt, J. Grima, W. Miller, N. Ravirala, C. Smith, K. Zied, Elastic constants of 3-, 4-and 6-connected chiral and anti-chiral honeycombs subject to uniaxial in-plane loading, Composites Science and Technology, 70 (2010) 1042-1048.

[47] A. Alderson, K.L. Alderson, G. Chirima, N. Ravirala, K.M. Zied, The in-plane linear elastic constants and out-of-plane bending of 3-coordinated ligament and cylinder-ligament honeycombs, Composites Science and Technology, 70 (2010) 1034-1041.

[48] D. Prall, R. Lakes, Properties of a chiral honeycomb with a poisson's ratio of—1, International Journal of Mechanical Sciences, 39 (1997) 305-314.

[49] Y. Chen, X. Liu, G. Hu, Q. Sun, Q. Zheng, Micropolar continuum modelling of bi-dimensional tetrachiral lattices, Proceedings of the Royal Society A: Mathematical, Physical and Engineering Science, 470 (2014) 20130734.

[50] Y. Chen, X. Liu, G. Hu, Micropolar modeling of planar orthotropic rectangular chiral lattices, Comptes Rendus Mécanique, 342 (2014) 273-283.

[51] A. Bacigalupo, L. Gambarotta, Homogenization of periodic hexa-and tetrachiral cellular solids, Composite Structures, (2014).

[52] A. Ajdari, B.H. Jahromi, J. Papadopoulos, H. Nayeb-Hashemi, A. Vaziri, Hierarchical honeycombs with tailorable properties, International Journal of Solids and Structures, 49 (2012) 1413–1419.

[53] R. Oftadeh, B. Haghpanah, J. Papadopoulos, A. Hamouda, H. Nayeb-Hashemi, A. Vaziri, Mechanics of anisotropic hierarchical honeycombs, International Journal of Mechanical Sciences, 81 (2014) 126-136.

[54] R. Oftadeh, B. Haghpanah, D. Vella, A. Boudaoud, A. Vaziri, Optimal Fractal-Like Hierarchical Honeycombs, Physical review letters, 113 (2014) 104301.

[55] F. Barthelat, H. Espinosa, An experimental investigation of deformation and fracture of nacre–mother of pearl, Experimental mechanics, 47 (2007) 311-324.

[56] N.M. Pugno, Mimicking nacre with super-nanotubes for producing optimized super-composites, Nanotechnology, 17 (2006) 5480.

[57] Z. Zhang, Y.-W. Zhang, H. Gao, On optimal hierarchy of load-bearing biological materials, Proceedings of the Royal Society B: Biological Sciences, 278 (2011) 519-525.

[58] D. Mousanezhad, H. Ebrahimi, B. Haghpanah, R. Ghosh, A. Ajdari, A. Hamouda, A. Vaziri, Spiderweb honeycombs, International Journal of Solids and Structures, 66 (2015) 218-227.

[59] D. Rayneau-Kirkhope, Y. Mao, R. Farr, Ultralight Fractal Structures from Hollow Tubes, Phys. Rev. Letts, 109 (2012) 204301.

[60] B. Haghpanah, J. Papadopoulos, A. Vaziri, Plastic collapse of lattice structures under a general stress state, Mechanics of Materials, 68 (2014) 267-274.

[61] B. Haghpanah, J. Papadopoulos, D. Mousanezhad, H. Nayeb-Hashemi, A. Vaziri, Buckling of regular, chiral and hierarchical honeycombs under a general macroscopic stress state, Proceedings of the Royal Society A: Mathematical, Physical and Engineering Science, 470 (2014) 20130856.

[62] Y. Sun, N. Pugno, Hierarchical Fibers with a Negative Poisson's Ratio for Tougher Composites, Materials, 6 (2013) 699-712.

[63] F. Song, J. Zhou, X. Xu, Y. Xu, Y. Bai, Effect of a negative Poisson ratio in the tension of ceramics, Physical review letters, 100 (2008) 245502.

[64] R. Lakes, High damping composite materials: effect of structural hierarchy, Journal of composite materials, 36 (2002) 287-297.

[65] D. Mousanezhad, S. Babaee, H. Ebrahimi, R. Ghosh, A.S. Hamouda, K. Bertoldi, A. Vaziri, Hierarchical honeycomb auxetic metamaterials, Scientific reports, 5 (2015).

[66] D. Mousanezhad, S. Babaee, R. Ghosh, E. Mahdi, K. Bertoldi, A. Vaziri, Honeycomb phononic crystals with self-similar hierarchy, Physical Review B, 92 (2015) 104304.

[67] R.S. Farr, Fractal design for an efficient shell strut under gentle compressive loading, Physical Review E, 76 (2007) 056608.

[68] R.S. Farr, Fractal design for efficient brittle plates under gentle pressure loading, Physical Review E, 76 (2007) 046601.

[69] D. Rayneau-Kirkhope, R. Farr, Y. Mao, Fractal-like dependence in the designs of efficient pressure-bearing structures, EPL (Europhysics Letters), 93 (2011) 34002.

[70] D. Rayneau-Kirkhope, Y. Mao, R. Farr, J. Segal, Hierarchical space frames for high mechanical efficiency: Fabrication and mechanical testing, Mechanics Research Communications, (2012).

[71] B. Haghpanah, R. Oftadeh, J. Papadopoulos, A. Vaziri, Self-similar hierarchical honeycombs, Proceedings of the Royal Society A: Mathematical, Physical and Engineering Science, 469 (2013).

[72] A.P. Boresi, R.J. Schmidt, Advanced mechanics of materials, Wiley, 2002.

[73] R. Christensen, Sufficient symmetry conditions for isotropy of the elastic moduli tensor, Journal of applied mechanics, 54 (1987) 772.

[74] C.T. Herakovich, Mechanics of Fibrous Composites, 1 ed., Wiley, 1997.

[75] L.J. Gibson, M.F. Ashby, Cellular solids: structure and properties, Cambridge Univ Pr, 1999.

[76] A. Ajdari, B.H. Jahromi, J. Papadopoulos, H. Nayeb-Hashemi, A. Vaziri, Hierarchical honeycombs with tailorable properties, International Journal of Solids and Structures, 49 (2012) 1413-1419.

[77] H. Harders, K. Hupfer, J. Rösler, Influence of cell wall shape and density on the mechanical behaviour of 2D foam structures, Acta Materialia, 53 (2005) 1335-1345.

[78] A. Ajdari, B. Haghpanah Jahromi, J. Papadopoulos, A. Vaziri, Honeycombs with hierarchical organization, Bulletin of the American Physical Society, 57 (2012).

[79] T.A. Blackledge, R.A. Cardullo, C.Y. Hayashi, Polarized light microscopy, variability in spider silk diameters, and the mechanical characterization of spider silk, Invertebrate Biology, 124 (2005) 165-173.

[80] T.A. Blackledge, J.E. Swindeman, C.Y. Hayashi, Quasistatic and continuous dynamic characterization of the mechanical properties of silk from the cobweb of the black widow spider Latrodectus hesperus, Journal of Experimental Biology, 208 (2005) 1937-1949.

[81] S.W. Cranford, A. Tarakanova, N.M. Pugno, M.J. Buehler, Nonlinear material behaviour of spider silk yields robust webs, Nature, 482 (2012) 72-76.

[82] L. Eisoldt, A. Smith, T. Scheibel, Decoding the secrets of spider silk, Materials Today, 14 (2011) 80-86.

[83] K.J. Koski, P. Akhenblit, K. McKiernan, J.L. Yarger, Non-invasive determination of the complete elastic moduli of spider silks, Nat Mater, 12 (2013) 262-267.

[84] Z. Qin, M.J. Buehler, Spider silk: Webs measure up, Nat Mater, 12 (2013) 185-187.

[85] Y. Termonia, Molecular Modeling of Spider Silk Elasticity, Macromolecules, 27 (1994) 7378-7381.

[86] F. Vollrath, Silk evolution untangled, Nature, 466 (2010) 319-319.

[87] N.M. Pugno, S.W. Cranford, M.J. Buehler, Synergetic Material and Structure Optimization Yields Robust Spider Web Anchorages, Small, 9 (2013) 2747-2756.

[88] V.M. Ortega-Jimenez, R. Dudley, Spiderweb deformation induced by electrostatically charged insects, Sci. Rep., 3 (2013).

[89] F.K. Ko, J. Jovicic, Modeling of Mechanical Properties and Structural Design of Spider Web, Biomacromolecules, 5 (2004) 780-785.

[90] A. Ajdari, B.H. Jahromi, J. Papadopoulos, H. Nayeb-Hashemi, A. Vaziri, Hierarchical honeycombs with tailorable properties, Int J Solids Struct, 49 (2012) 1413-1419.

[91] Y. Sun, N.M. Pugno, In plane stiffness of multifunctional hierarchical honeycombs with negative Poisson's ratio sub-structures, Composite Structures, 106 (2013) 681-689.

[92] Y. Sun, Q. Chen, N. Pugno, Elastic and transport properties of the tailorable multifunctional hierarchical honeycombs, Composite Structures, 107 (2014) 698-710.

[93] S. Banerjee, On the mechanical properties of hierarchical lattices, Mechanics of Materials, 72 (2014) 19-32.

[94] A. Vigliotti, D. Pasini, Mechanical properties of hierarchical lattices, Mechanics of Materials, 62 (2013) 32-43.

[95] H. Fan, F. Jin, D. Fang, Mechanical properties of hierarchical cellular materials. Part I: Analysis, Composites Science and Technology, 68 (2008) 3380-3387.

[96] C.M. Taylor, C.W. Smith, W. Miller, K.E. Evans, The effects of hierarchy on the in-plane elastic properties of honeycombs, International Journal of Solids and Structures, 48 (2011) 1330-1339.

[97] U.G. Wegst, H. Bai, E. Saiz, A.P. Tomsia, R.O. Ritchie, Bioinspired structural materials, Nature materials, (2014).

[98] L.J. Gibson, M.F. Ashby, Cellular Solids: Structure and Properties, 2 ed., Cambridge University Press, Cambridge, MA, 1997.

[99] B. Haghpanah, J. Papadopoulos, D. Mousanezhad, H. Nayeb-Hashemi, A. Vaziri, Buckling of regular, chiral, and hierarchical honeycombs under a general macroscopic

stress state, Proceedings of the Royal Society A: Mathematical, Physical and Engineering Science, 470 (2014).

[100] X. Hou, V.V. Silberschmidt, Metamaterials with negative poisson's ratio: A review of mechanical properties and deformation mechanisms, in: Mechanics of Advanced Materials, Springer, 2015, pp. 155-179.

[101] T.-C. Lim, Auxetic Materials and Structures, Springer, 2015.

[102] H. Mitschke, J. Schwerdtfeger, F. Schury, M. Stingl, C. Körner, R.F. Singer, V. Robins, K. Mecke, G.E. Schröder-Turk, Finding auxetic frameworks in periodic tessellations, Advanced Materials, 23 (2011) 2669-2674.

[103] M. Taylor, L. Francesconi, M. Gerendás, A. Shanian, C. Carson, K. Bertoldi, Low Porosity Metallic Periodic Structures with Negative Poisson's Ratio, Advanced Materials, 26 (2014) 2365-2370.

[104] J. Schwerdtfeger, F. Wein, G. Leugering, R. Singer, C. Körner, M. Stingl, F. Schury, Design of auxetic structures via mathematical optimization, Advanced materials, 23 (2011) 2650-2654.

[105] G. Wu, Y. Cho, I.S. Choi, D. Ge, J. Li, H.N. Han, T. Lubensky, S. Yang, Directing the Deformation Paths of Soft Metamaterials with Prescribed Asymmetric Units, Advanced Materials, 27 (2015) 2747-2752.

[106] R. Lakes, Advances in negative Poisson's ratio materials, Advanced Materials, 5 (1993) 293-296.

[107] K. Evans, M. Nkansah, I. Hutchinson, S. Rogers, Molecular network design, (1991).

[108] R. Lakes, R. Witt, Making and characterizing negative Poisson's ratio materials, International Journal of Mechanical Engineering Education, 30 (2002) 50-58.

[109] L. Gibson, M. Ashby, G. Schajer, C. Robertson, The mechanics of two-dimensional cellular materials, Proceedings of the Royal Society of London. A. Mathematical and Physical Sciences, 382 (1982) 25-42.

[110] R. Lakes, Foam structures with a negative Poisson's ratio, Science, 235 (1987) 1038-1040.

[111] Y. Chen, F. Scarpa, Y. Liu, J. Leng, Elasticity of anti-tetrachiral anisotropic lattices, International Journal of Solids and Structures, 50 (2013) 996-1004.

[112] R. Gatt, L. Mizzi, J.I. Azzopardi, K.M. Azzopardi, D. Attard, A. Casha, J. Briffa, J.N. Grima, Hierarchical Auxetic Mechanical Metamaterials, Scientific reports, 5 (2015).

[113] D. Attard, J.N. Grima, A three-dimensional rotating rigid units network exhibiting negative Poisson's ratios, physica status solidi (b), 249 (2012) 1330-1338.

[114] J.N. Grima, R. Gatt, B. Ellul, E. Chetcuti, Auxetic behaviour in non-crystalline materials having star or triangular shaped perforations, Journal of Non-Crystalline Solids, 356 (2010) 1980-1987.

[115] D. Mousanezhad, H. Ebrahimi, B. Haghpanah, R. Ghosh, A. Ajdari, A.M.S. Hamouda, A. Vaziri, Spiderweb honeycombs, International Journal of Solids and Structures, 66 (2015) 218-227.

[116] S. Babaee, J. Shim, J.C. Weaver, E.R. Chen, N. Patel, K. Bertoldi, 3D Soft metamaterials with negative Poisson's ratio, Advanced Materials, 25 (2013) 5044-5049.

[117] K. Bertoldi, P.M. Reis, S. Willshaw, T. Mullin, Negative Poisson's ratio behavior induced by an elastic instability, Advanced Materials, 22 (2010) 361-366.

[118] D. Mousanezhad, S. Babaee, R. Ghosh, E. Mahdi, K. Bertoldi, A. Vaziri, Honeycomb phononic crystals with self-similar hierarchy, Submitted to Physical Review B, (2015).

[119] S. Shan, S.H. Kang, Z. Zhao, L. Fang, K. Bertoldi, Design of planar isotropic negative Poisson's ratio structures, Extreme Mechanics Letters, 4 (2015) 96-102.

[120] J. Shim, S. Shan, A. Košmrlj, S.H. Kang, E.R. Chen, J.C. Weaver, K. Bertoldi, Harnessing instabilities for design of soft reconfigurable auxetic/chiral materials, Soft Matter, 9 (2013) 8198-8202.

[121] K. Bertoldi, M. Boyce, S. Deschanel, S. Prange, T. Mullin, Mechanics of deformation-triggered pattern transformations and superelastic behavior in periodic elastomeric structures, Journal of the Mechanics and Physics of Solids, 56 (2008) 2642-2668.

[122] A. Alderson, J. Rasburn, K. Evans, J. Grima, Auxetic polymeric filters display enhanced de-fouling and pressure compensation properties, Membrane Technology, 2001 (2001) 6-8.

[123] J.L. Katz, A. Misra, P. Spencer, Y. Wang, S. Bumrerraj, T. Nomura, S.J. Eppell, M. Tabib-Azar, Multiscale mechanics of hierarchical structure/property relationships in calcified tissues and tissue/material interfaces, Materials Science and Engineering: C, 27 (2007) 450-468.

[124] H. Yao, H. Gao, Mechanics of robust and releasable adhesion in biology: Bottom–up designed hierarchical structures of gecko, Journal of the Mechanics and Physics of Solids, 54 (2006) 1120-1146.

[125] D. Ren, Y. Ma, Z. Li, Y. Gao, Q. Feng, Hierarchical structure of asteriscus and in vitro mineralization on asteriscus substrate, Journal of Crystal Growth, 325 (2011) 46-51.

[126] Y. Su, B. Ji, K. Zhang, H. Gao, Y. Huang, K. Hwang, Nano to Micro Structural Hierarchy Is Crucial for Stable Superhydrophobic and Water-Repellent Surfaces, Langmuir, 26 (2010) 4984-4989.

[127] D. Rayneau-Kirkhope, Y. Mao, R. Farr, Ultralight fractal structures from hollow tubes, Physical review letters, 109 (2012) 204301.

[128] S. Kinoshita, Structural colors in the realm of nature, World Scientific, 2008.

[129] L.P. Biro, J.-P. Vigneron, Photonic nanoarchitectures in butterflies and beetles: valuable sources for bioinspiration, Laser & Photonics Reviews, 5 (2011) 27-51.

[130] A.D. Pris, Y. Utturkar, C. Surman, W.G. Morris, A. Vert, S. Zalyubovskiy, T. Deng, H.T. Ghiradella, R.A. Potyrailo, Towards high-speed imaging of infrared photons with bio-inspired nanoarchitectures, Nature Photonics, 6 (2012) 195-200.

[131] J. Teyssier, S.V. Saenko, D. Van Der Marel, M.C. Milinkovitch, Photonic crystals cause active colour change in chameleons, Nature communications, 6 (2015).

[132] L.F. Deravi, A.P. Magyar, S.P. Sheehy, G.R. Bell, L.M. Mäthger, S.L. Senft, T.J. Wardill, W.S. Lane, A.M. Kuzirian, R.T. Hanlon, The structure–function relationships of a natural nanoscale photonic device in cuttlefish chromatophores, Journal of The Royal Society Interface, 11 (2014) 20130942.

[133] K. Bertoldi, M. Boyce, Wave propagation and instabilities in monolithic and periodically structured elastomeric materials undergoing large deformations, Physical Review B, 78 (2008) 184107.

[134] P. Wang, J. Shim, K. Bertoldi, Effects of geometric and material nonlinearities on tunable band gaps and low-frequency directionality of phononic crystals, Physical Review B, 88 (2013) 014304.

[135] J. Shim, P. Wang, K. Bertoldi, Harnessing instability-induced pattern transformation to design tunable phononic crystals, International Journal of Solids and Structures, 58 (2015) 52-61.

[136] K. Jim, C. Leung, S. Lau, S. Choy, H. Chan, Thermal tuning of phononic bandstructure in ferroelectric ceramic/epoxy phononic crystal, Applied Physics Letters, 94 (2009) 193501.

[137] S. Gonella, M. Ruzzene, Analysis of in-plane wave propagation in hexagonal and re-entrant lattices, Journal of Sound and Vibration, 312 (2008) 125-139.

[138] A.S. Phani, J. Woodhouse, N. Fleck, Wave propagation in two-dimensional periodic lattices, The Journal of the Acoustical Society of America, 119 (2006) 1995-2005.

[139] X. Liu, G. Hu, C. Sun, G. Huang, Wave propagation characterization and design of two-dimensional elastic chiral metacomposite, Journal of Sound and Vibration, 330 (2011) 2536-2553.

[140] Y. Xu, C. Chen, X. Tian, Wave Characteristics of Two-Dimensional Hierarchical Hexagonal Lattice Structures, Journal of Vibration and Acoustics, 136 (2014) 011011.

[141] L. Brillouin, Wave propagation in periodic structures: electric filters and crystal lattices, Courier Dover Publications, 2003.

[142] M. Maldovan, E.L. Thomas, Periodic Materials and Interference Lithography: For Photonics, Phononics and Mechanics, John Wiley & Sons, 2009.

[143] F. Casadei, J. Rimoli, Anisotropy-induced broadband stress wave steering in periodic lattices, International Journal of Solids and Structures, 50 (2013) 1402-1414.

[144] E. Nolde, R. Craster, J. Kaplunov, High frequency homogenization for structural mechanics, Journal of the Mechanics and Physics of Solids, 59 (2011) 651-671.

[145] S. Gonella, M. Ruzzene, Homogenization and equivalent in-plane properties of two-dimensional periodic lattices, International Journal of Solids and Structures, 45 (2008) 2897-2915.

[146] M. Maldovan, E. Thomas, Simultaneous complete elastic and electromagnetic band gaps in periodic structures, Applied Physics B, 83 (2006) 595-600.

[147] S. Babaee, P. Wang, K. Bertoldi, Three-dimensional adaptive soft phononic crystals, Journal of Applied Physics, 117 (2015) 244903.

[148] L. Treloar, Stress-strain data for vulcanised rubber under various types of deformation, Trans. Faraday Soc., 40 (1944) 59-70.

[149] W. Cheng, J. Wang, U. Jonas, G. Fytas, N. Stefanou, Observation and tuning of hypersonic bandgaps in colloidal crystals, Nature Materials, 5 (2006) 830-836.

[150] J. Vasseur, A.-C. Hladky-Hennion, B. Djafari-Rouhani, F. Duval, B. Dubus, Y. Pennec, P. Deymier, Waveguiding in two-dimensional piezoelectric phononic crystal plates, Journal of Applied Physics, 101 (2007) 114904.

[151] M. Maldovan, Sound and heat revolutions in phononics, Nature, 503 (2013) 209-217.

[152] D. Logan, A first course in the finite element method, Cengage Learning, 2011.

[153] S. Babaee, P. Wang, K. Bertoldi, Three-dimensional adaptive soft phononic crystals, Physical review B, (2015).

[154] K. Bertoldi, M. Boyce, Mechanically triggered transformations of phononic band gaps in periodic elastomeric structures, Physical Review B, 77 (2008) 052105.

[155] J. Shim, P. Wang, K. Bertoldi, Harnessing instability-induced pattern transformation to design tunable phononic crystals, International Journal of Solids and Structures, (2014).